Universitat
Autònoma
de Barcelona

Generation of ferromagnetism on non-magnetic materials

Doctoral Thesis by

Enric Menéndez Dalmau

Bellaterra, September 2008

Departament de Física

Facultat de Ciències

Directors: Dr. Jordi Sort and Dr. Josep Nogués

Els Doctors **Josep Nogués Sanmiquel** i **Jordi Sort Viñas**, directors de la Tesi Doctoral "Generation of ferromagnetism on non-magnetic materials" realitzada per l'**Enric Menéndez Dalmau**,

fan constar

que l'aportació de l'Enric Menéndez Dalmau al treball que es presenta ha estat fonamental tant pel que fa al disseny experimental, com per a l'obtenció de les mostres, la realització dels experiments, l'anàlisi de les dades i la discussió i elaboració dels resultats.

I per a què així consti, a petició de l'interessat i als efectes oportuns, signem la tesi doctoral a Bellaterra, el 25 de Setembre de 2008.

Dr. J. Nogués Dr. J. Sort

Acknowledgements

En primer lloc, voldria agrair la permanent dedicació, suport i orientació científica que he rebut per part dels meus directors, el Dr. Jordi Sort i el Prof. Josep Nogués. Agraeixo la seva crítica i els consells que m'han donat en tot moment, el temps que han invertit en la meva formació científica i, en particular, el fet que han aconseguit fer-me sentir un investigador més al seu costat.

Agraeixo a la Professora Maria Dolors Baró i al Prof. Santiago Suriñach la possibilitat que em van donar de pertànyer al *Grup de Física de Materials II*, la seva ajuda constant i els seus consells.

Voldria agrair al Servei de Microscòpia de la UAB i al Dr. Ángel Álvarez la seva col·laboració i consell en la realització i anàlisi de les experiències de microscòpia electrònica i difracció de raigs X, respectivament. A més, també voldria destacar la total disposició del Jordi, el Manel, el Rafa i el Ramón pel suport tècnic que donen al nostre grup.

Un record especial per a la resta de membres, amb els que he compartit moments molt bons i he après un munt de coses, que pertanyen o han format part del *Grup de Física de Materials II*.

En relació a les meves estades al *Forschungszentrum Dresden-Rossendorf* d'Alemanya, voldria destacar la bona acollida, el tracte i l'ajut que he rebut del Dr. Maciej Oskar Liedke i del Dr. Jürgen Fassbender. També voldria donar les gràcies a la resta de persones amb les que he treballat al llarg d'aquests anys i la seva col·laboració s'ha vist directament reflectida en aquesta Tesi: Dr. A. Concustell, A. Martinavicius, Dr. G. Abrasonis, T. Strache, Prof. W. Möller, Dr. T. Gemming, Dra. A. Weber, Dra. L. J. Heyderman, Prof. K. V. Rao, Dr. S. C. Deevi, J. Sommerlatte i Prof. K. Nielsch.

Vull agrair al Ministerio de Educación y Ciencia per la beca de *Formación de Personal Investigador*, cofinançada pel Fons Social Europeu, que em van concedir.

També vull donar les gràcies als meus amics per les bones estones que passo al seu costat i els ànims que sempre m'han donat. Finalment i de manera molt especial, m'agradaria agrair el constant suport i ajuda que sempre he rebut i rebo dels meus pares, de la meva germana Mireia i dels meus cosins, un pilar fonamental per a mi.

Resum

En els darrers anys, el desenvolupament de nous mètodes per a la fabricació de xarxes ordenades de nanoestructures magnètiques (litografia magnètica) ha esdevingut un camp de recerca de gran interès. Això es deu tant per l'ampli ventall d'aplicacions tecnològiques que se'n deriven de les estructures magnètiques de grandària submicromètrica (biomedicina, gravació magnètica, ...), com per raons de caire més fonamental, ja que sovint el comportament magnètic d'aquests materials a escala nanomètrica és diferent del corresponent als materials massissos.

Els aliatges de $Fe_{60}Al_{40}$ (percentatge atòmic) i els acers inoxidables austenítics posseeixen una combinació de propietats estructurals i magnètiques que els converteix en materials amb cert potencial per a ser litografiats magnèticament. Des d'un punt de vista magnètic, mentre que els aliatges de $Fe_{60}Al_{40}$ ordenats atòmicament són paramagnètics a temperatura ambient, els aliatges de $Fe_{60}Al_{40}$ desordenats a nivell atòmic presenten un comportament ferromagnètic. Pel que fa als acers inoxidables austenítics, a partir de deformació mecànica, es pot induir la transformació en estat sòlid de la fase austenita (paramagnètica) a la fase martensita (ferromagnètica) en aquests aliatges ferris. A més, els processos de nitruració a temperatura moderada en acers inoxidables austenítics permeten transformar parcialment la fase austenita en la fase "austenita expandida", que és una solució sòlida sobresaturada de nitrogen que presenta un comportament ferromagnètic.

Aquesta Tesi està basada en la generació de xarxes ordenades d'entitats ferromagnètiques a escala micro/nanomètrica, dins d'una matriu paramagnètica, en la superfície d'aliatges de $Fe_{60}Al_{40}$ i acers inoxidables austenítics. Aquest propòsit s'assoleix aprofitant les transicions magnètiques que tenen lloc en aquests materials després de sotmetre'ls a processos de deformació plàstica local (nanoindentació) i irradiació controlada amb ions (ús de feixos d'ions focalitzats i irradiació amb ions de gasos nobles a través de màscares en el cas del $Fe_{60}Al_{40}$ i processos de nitruració a través de màscares d'irradiació en els acers inoxidables austenítics). Cal esmentar que també s'ha dut a terme un estudi detallat de les modificacions a nivell estructural, mecànic i magnètic que ocorren en aquests materials una vegada s'han deformat mecànicament o irradiat amb ions.

Summary

In recent years, intense research is being pursued in the development of novel methods for the fabrication of arrays of ordered magnetic nanostructures. This is motivated, in part, by the technological applications of sub-micron magnetic structures, ranging from biomedicine to recording media, but it is also due to fundamental scientific reasons, since the behavior of magnetic materials at this length scale is often significantly different from that in the bulk.

$Fe_{60}Al_{40}$ (at. %) alloys and austenitic stainless steels show an interesting combination of magnetic and structural properties, which makes them turn into potential candidates to be magnetically patterned. Namely, from the magnetic point of view, whereas atomically ordered $Fe_{60}Al_{40}$ (at. %) is paramagnetic at room temperature, disordered $Fe_{60}Al_{40}$ becomes ferromagnetic. Concerning austenitic stainless steels, due to mechanical deformation, a phase transformation from the paramagnetic austenite phase to the ferromagnetic martensite phase can occur in these ferrous alloys. In addition, nitriding of austenitic stainless steels at moderate temperatures is able to partially transform the austenite phase into the supersaturated nitrogen solid solution, often called in the literature “expanded austenite” phase, which shows ferromagnetic behavior.

This Thesis is mainly focused on the generation of ordered arrays of micro/nanoscaled ferromagnetic entities (i.e., magnetic patterning), embedded in a paramagnetic matrix, at the surface of either $Fe_{60}Al_{40}$ (at. %) alloys or austenitic stainless steels. This is accomplished by taking advantage of the magnetic transitions which occur in these alloys upon local plastic deformation (nanoindentation) and controlled ion irradiation (focused ion beam and broad beam noble gas ion irradiation through shadow masks in FeAl alloys and ion beam nitriding through shadow masks in austenitic stainless steels). Furthermore, a detailed study of the structural, mechanical and magnetic changes which take place in these materials upon either mechanical deformation or ion irradiation is presented.

Index

Preface

In recent years, intense research is being pursued in the development of novel methods for the fabrication of arrays of ordered magnetic nanostructures [1,2]. This is motivated, in part, by the technological applications of sub-micron magnetic structures, ranging from biomedicine to recording media [3,4], but it is also due to fundamental scientific reasons, since the behavior of magnetic materials at this length scale is often significantly different from that in the bulk [5]. Nevertheless, the production of magnetic nanostructures, arranged in regular configurations (i.e., patterned), over areas in the macroscopic range still remains rather challenging [2].

$Fe_{60}Al_{40}$ (at. %) alloys and austenitic stainless steels (ASSs) show an interesting combination of magnetic and structural properties, which make them turn into potential candidates to be magnetically patterned. Namely, from the magnetic point of view, whereas atomically ordered $Fe_{60}Al_{40}$ (at. %) is paramagnetic at room temperature, disordered $Fe_{60}Al_{40}$ becomes ferromagnetic [6,7]. Concerning ASSs, it is known that, due to mechanical deformation, a phase transformation from the paramagnetic austenite (γ) phase to the ferromagnetic martensite (α') phase can occur in these ferrous alloys [8]. In addition, nitriding of ASSs at moderate temperatures is able to partially transform the austenite phase into the supersaturated nitrogen solid solution, often called in the literature "expanded austenite" or γ_N phase [9], which shows ferromagnetic behavior [10].

This Thesis is mainly focused on the generation of ordered arrays of micro/nanoscaled ferromagnetic entities (i.e., magnetic patterning) at the surface of either $Fe_{60}Al_{40}$ (at. %) alloys or ASSs (AISI 304L, AISI 316 and AISI 316L, see appendix for further details). This is accomplished by taking advantage of the magnetic transitions which occur in these alloys upon local plastic deformation and controlled ion irradiation.

The main objectives of this doctoral thesis are:

- To investigate the deformation-induced ferromagnetism in atomically ordered $Fe_{60}Al_{40}$ (at. %) alloys subjected to compression tests and correlate structural (i.e., lattice cell parameter, crystallite size, microstrain and atomic intermixing), mechanical (i.e., microhardness) and magnetic (i.e., saturation magnetization) properties.

- To study the generation of ferromagnetism in ordered $Fe_{60}Al_{40}$ (at. %) alloys by ion irradiation, analyzing the effect of different ion species on the induced magnetism.

- To show the feasibility to produce periodic arrays of isolated ferromagnetic structures in the micro/nanoscaled range, embedded in a paramagnetic matrix, by means of either local mechanical deformation (i.e., nanoindentation) or selective ion irradiation (i.e., using either ion irradiation through shadow masks or focused ion beam) on $Fe_{60}Al_{40}$ alloys.

- To study the mechanically induced martensitic transformation obtained by means of either ball milling processes in AISI 316L ASS powders (dynamic approach, i.e. high strain rate processing) or compressive deformation in AISI 316L ASS bulk specimens (quasi-static approach, i.e. low strain rate processing), aimed at tailoring and correlating the induced structural, mechanical, and magnetic properties.

- To demonstrate the feasibility to produce periodic arrays of isolated ferromagnetic structures in the micro/nanoscaled range, embedded in a paramagnetic matrix, by either local mechanical deformation (i.e., nanoindentation) or selective ion irradiation (i.e., ion beam nitriding through shadow masks) on austenitic stainless steels.

This work has been organized in different chapters as follows:

- Chapter 1 introduces some of the current techniques to prepare arrays of ordered magnetic structures. Moreover, the fundamental aspects regarding the origin of ferromagnetism in both $Fe_{60}Al_{40}$ (at. %) alloys and ASSs are presented.

- Chapter 2 deals with the experimental procedures that have been used to induce ferromagnetism in $Fe_{60}Al_{40}$ (at. %) alloys and austenitic stainless steels by means of either plastic deformation (mechanical milling and compression testing) or ion irradiation (broad beam ion irradiation and focused ion beam). Next, the techniques for structural, morphological, mechanical and magnetic characterization are described.

- Chapter 3 presents the obtained results and their discussion. The studied materials (i.e., $Fe_{60}Al_{40}$ and ASSs) lead to the two major sections of this chapter. Both sections start reporting on the generation of ferromagnetism by mechanical deformation (part A) in a macroscopic approach. Then, the results concerning the creation of micro/nanoscaled ferromagnetic structures by means of local mechanical deformation are presented. Finally, the irradiation-induced ferromagnetism investigation (part B) is reported starting from the macroscopic approach, followed by the magnetic patterning using ion irradiation.

- Chapter 4 points out the main conclusions of this doctoral thesis.

Finally, an appendix about some compositional aspects of the studied ASSs is presented.

This Thesis has been partially based on the following articles:

- J. Sort, A. Concustell, E. Menéndez, S. Suriñach, M. D. Baró, J. Farran and J. Nogués: Selective generation of local ferromagnetism in austenitic stainless steel using nanoindentation *Appl. Phys. Lett.* **89** 032509 (2006)

- J. Sort, A. Concustell, E. Menéndez, S. Suriñach, K. V. Rao, S. C. Deevi, M. D. Baró and J. Nogués: Periodic arrays of micrometer and sub-micrometer magnetic structures prepared by nanoindentation of a nonmagnetic intermetallic compound *Adv. Mater.* **18** 1717 (2006)

- J. Fassbender, M. O. Liedke, T. Strache, W. Möller, E. Menéndez , J. Sort, K. V. Rao, S. C. Deevi and J. Nogués: Ion mass dependence of the irradiation-induced local creation of ferromagnetism in $Fe_{60}Al_{40}$ alloys *Phys. Rev. B* **77** 174430 (2008)

- E. Menéndez, A. Martinavicius, M. O. Liedke, G. Abrasonis, J. Fassbender, J. Sommerlatte, K. Nielsch, S. Suriñach, M. D. Baró, J. Nogués and J. Sort: Patterning of magnetic structures on austenitic stainless steel by local ion beam nitriding *Acta Mater.* **56** 4570 (2008)

- E. Menéndez, J. Sort, M. O. Liedke, J. Fassbender, S. Suriñach, M. D. Baró and J. Nogués: Two-fold origin of the deformation-induced ferromagnetism in bulk $Fe_{60}Al_{40}$ (at.%) alloys *New J. Phys.* **10** 103030 (2008)

- J. Sort, E. Menéndez, A. Concustell, S. Suriñach, M. D. Baró, G. Salazar-Alvarez and J. Nogués: Nous materials per a l'emmagatzematge magnètic d'alta densitat *Revista de l'Institut d'Estudis Catalans* In press

- E. Menéndez, J. Sort, M. O. Liedke, J. Fassbender, T. Gemming, A. Weber, L. J. Heyderman, S. Suriñach, K. V. Rao, S. C. Deevi, M. D. Baró and J. Nogués: Direct magnetic patterning due to the generation of ferromagnetism by selective ion irradiation of paramagnetic FeAl alloys *Small* doi: 10.1002/smll.200800783 In press

- E. Menéndez, J. Sort, M. O. Liedke, J. Fassbender, S. Suriñach, M. D. Baró and J. Nogués: Controlled generation of ferromagnetic martensite from paramagnetic austenite in AISI 316L austenitic stainless steel submitted

and the patent P200600426:

- Inventors (in order of authorship): J. Sort, J. Nogués, A. Concustell, E. Menéndez, S. Suriñach and M. D. Baró. Title: Procedimiento para la fabricación de un artículo con zonas ferromagnéticas y zonas no ferromagnéticas (Priority Country: Spain, Priority Date: 17th February 2006, Holder Entities: Universitat Autònoma de Barcelona/Institució Catalana de Recerca i Estudis Avançats)

Other articles co-authored by E. Menéndez not directly related to this Thesis are:

- E. Menéndez, J. Sort, V. Langlais, A. Zhilyaev, J. S. Muñoz, S. Suriñach, J. Nogués and M. D. Baró: Cold compaction of metal-ceramic (ferromagnetic-antiferromagnetic) composites using high pressure torsion *J. Alloys Compd.* **434-435** 505 (2007)

- E. Menéndez, J. Sort, A. Concustell, S. Suriñach, J. Nogués and M. D. Baró: Microstructural evolution during solid state sintering of ball-milled nanocomposite WC-10 mass% Co powders *Nanotechnology* **18** 185609 (2007)

- E. Menéndez, J. Sort, S. Suriñach, M. D. Baró and J. Nogués: Tailoring deformation-induced effects in Co powders by milling them with α-Al_2O_3 *J. Mater. Res.* **22** 2998 (2007)

- J. Sort, K. S. Buchanan, J. E. Pearson, A. Hoffmann, E. Menéndez, G. Salazar-Alvarez, M. D. Baró, M. Miron, B. Rodmacq, B. Dieny and J. Nogués: Tailoring the magnetization reversal of elliptical dots using exchange bias *J. Appl. Phys.* **103** 07C109 (2008)

- E. Menéndez, G. Salazar-Alvarez, A. P. Zhilyaev, S. Suriñach, M. D. Baró, J. Nogués and J. Sort: Cold consolidation of metal-ceramic nanocomposite powders with large ceramic fractions *Adv. Funct. Mater.* **18** 3293 (2008)

Part of this work has been presented in the following *Invited Talks* which have been given in international conferences:

- J. Sort, A. Concustell, E. Menéndez, S. Suriñach, K. V. Rao, S. C. Deevi, J. Nogués and M. D. Baró: Periodic arrays of micron and submicron magnetic structures prepared

by nanoindentation of a non-magnetic intermetallic compound *III Workshop on Metastable and Nanostructured Materials (Nanomat 2006)* Rio de Janeiro (Brazil) June 5 – 8 2006

- J. Sort, A. Concustell, E. Menéndez, S. Suriñach, K. V. Rao, J. Farran, S. C. Deevi, J. Nogués and M. D. Baró: Arrays of micron and submicron magnetic structures prepared by nanoindentation of non-magnetic substrates *International Symposium on Metastable, Mechanically Alloyed and Nanocrystalline Materials (ISMANAM 2006)* Warsaw (Poland) August 27 – 31 2006

- J. Sort, E. Menéndez, M. O. Leidke. T. Strache, J. Fassbender, T. Gemming, A. Weber, L. J. Heyderman, S. Suriñach, A. Concustell, K. V. Rao, S. C. Deevi, M. D. Baró and J. Nogués: Micro- and nanoscale patterning of paramagnetic FeAl alloys by means of nanoindentation or selective ion irradiation *First workshop on nanolithography and their applications* Zaragoza (Spain) October 23 – 26 2007

- J. Sort, E. Menéndez, A. Concustell, S. Suriñach, M. D. Baró, G. Salazar-Alvarez and J. Nogués: Nous materials per a l'emmagatzematge magnètic d'alta densitat *Jornada sobre nanociència i nanotecnologia a l'Institut d'Estudis Catalans* Barcelona (Spain) November 30 2007

- E. Menéndez, J. Sort, M. O. Liedke, J. Fassbender, T. Gemming, A. Weber, L. J. Heyderman, S. Suriñach, A. Concustell, K. V. Rao, S. C. Deevi, M. D. Baró and J. Nogués: Micro-/nano-scale magnetic patterning of paramagnetic FeAl intermetallic alloys *Winter School – Women in Nano* Kranjska Gora (Slovenia) February 7 – 9 2008

- J. Sort, E. Menéndez, M. O. Liedke, T. Strache, J. Fassbender, W. Möller, T. Gemming, A. Weber, L. J. Heyderman, S. Suriñach, K. V. Rao, S. C. Deevi, M. D. Baró and J. Nogués: Magnetic lithography on paramagnetic FeAl alloys by selective ion irradiation *9th International Conference on Nanostructured Materials (NANO2008)* Rio de Janeiro (Brazil) June 1 – 6 2008

- E. Menéndez, M. O. Liedke, A. Martinavicius, G. Abrasonis, T. Strache, W. Möller, J. Fassbender, T. Gemming, J. Sommerlatte, K. Nielsch, S. C. Deevi, K. V. Rao, J. Sort, S. Suriñach, M. D. Baró and J. Nogués: Ion beam irradiation to locally generate ferromagnetism in non-magnetic intermetallic alloys and non-magnetic austenitic

stainless steels *2nd Meeting of the User Selection Panel and User Meeting* Forschungszentrum Dresden-Rossendorf (Germany) July 6 – 7 2008

- E. Menéndez, J. Sort, M. O. Liedke, T. Strache, J. Fassbender, W. Möller, T. Gemming, A. Weber, L. J. Heyderman, S. Suriñach, S. C. Deevi, K. V. Rao, J. Sommerlatte, K. Nielsch, J. Nogués and M. D. Baró: Magnetic nanoscale lithography on FeAl alloys by means of ion irradiation *International Symposium on Metastable, Mechanically Alloyed and Nanocrystalline Materials (ISMANAM 2008)* Buenos Aires (Argentina) July 6 – 10 2008

- E. Menéndez, J. Sort, M. O. Liedke, T. Strache, J. Fassbender, W. Möller, T. Gemming, A. Weber, L. J. Heyderman, S. Suriñach, S. C. Deevi, K. V. Rao, J. Sommerlatte, K. Nielsch, M. D. Baró and J. Nogués: Generation of Micro/Nano-scaled ferromagnetic entities by selective ion irradiation on FeAl alloys 16th *International Conference on Ion Beam Modification of Materials* Dresden (Germany) August 31 – September 5 2008

- E. Menéndez, J. Sort, M.O. Liedke, T. Strache, J. Fassbender, W. Möller, T. Gemming, A. Weber, L. J. Heyderman, S. Suriñach, S. C. Deevi, K. V. Rao , J. Sommerlatte, K. Nielsch, M. D. Baró and J. Nogués: Direct nanoscale magnetic patterning in FeAl alloys by means of ion irradiation *9th Trends in Nanotechnology International Conference (TNT)* Oviedo (Spain) September 1 – 5 2008

References

[1] J. I. Martín, J. Nogués, K. Liu, J. L. Vicent and I. K. Schuller *J. Magn. Magn. Mater.* **256** 449 (2003)

[2] A. O. Adeyeye and N. Singh *J. Phys. D: Appl. Phys.* **41** 153001 (2008)

[3] S. S. P. Parkin, X. Jiang, C. Kaiser, A. Panchula, K. Roche and M. Samant *Proc. IEEE* **91** 661 (2003)

[4] C. A. Ross *Annu. Rev. Mater. Res.* **31** 203 (2001)

[5] R. Skomski *J. Phys.: Condens. Mater.* **15** R841 (2003)

[6] M. J. Besnus, A. Herr and A. J. P. Meyer *J. Phys. F: Met. Phys.* **5** 2138 (1975)

[7] E. P. Yelsukov, E. V. Voronina and V. A. Barinov *J. Magn. Magn. Mater.* **115** 271 (1992)

[8] S. S. Hecker, M. G. Stout, K. P. Staudhammer and J. L. Smith *Metall. Trans. A* **13** 619 (1982)

[9] M. P. Fewell, D. R. G. Mitchell, J. M. Priest, K. T. Short and G. A. Collins *Surf. Coat. Technol.* **131** 300 (2000)

[10] O. Öztürk and D. L. Williamson *J. Appl. Phys.* **77** 3839 (1995)

1. Introduction

The most widely used fabrication methods for magnetic nanostructure production will be briefly described in this chapter. Then, the origin of ferromagnetism in paramagnetic $Fe_{60}Al_{40}$ (at. %) alloys and austenitic stainless steels (ASSs) will be addressed.

1.1. Patterning magnetic structures

In this subchapter, the main conventional techniques for patterning magnetic structures are described, distinguishing between the processes based on the use of masks and direct methods (i.e., not utilizing masks). In addition, a section concerning the fabrication of magnetically patterned materials by ion irradiation and implantation is presented since, by using this route, a pure magnetic patterning rather than topographic (i.e., with practically no alteration of the surface) can be obtained.

1.1.1. Using templates or masks

Lithography constitutes a central technique to fabricate arrays of ordered magnetic structures [1]. It is a broad term that includes several related processes, which are based on the production of a template with the desired distribution of structures, aimed at transferring its pattern to the material of interest. Namely, the working sample is coated by a specific material, which is then exposed to certain physical or chemical processes (e.g., radiation) in order to modify locally the properties of this layer (i.e., to write the wanted array of structures on the template). Subsequently, the material is treated (developed) to leave the designed pattern of the template onto the material to be magnetically patterned. Shown in Figure 1.1 is a schematic view of the process using polymeric layers (resist) exposed to radiation. As it can be seen in this illustration, positive (panel a) and negative (panel b) resists can be used, although the first type is more utilized due to its better resolving power [1]. Whereas the employed radiation breaks the polymer chains in the positive resist, it makes the polymer chains be more cross-linked in the negative layers. Therefore, after the development stage, the irradiated

zones of the polymeric layer are removed in the positive templates and, in contrast, remain at the top of the sample in the case of negative resists.

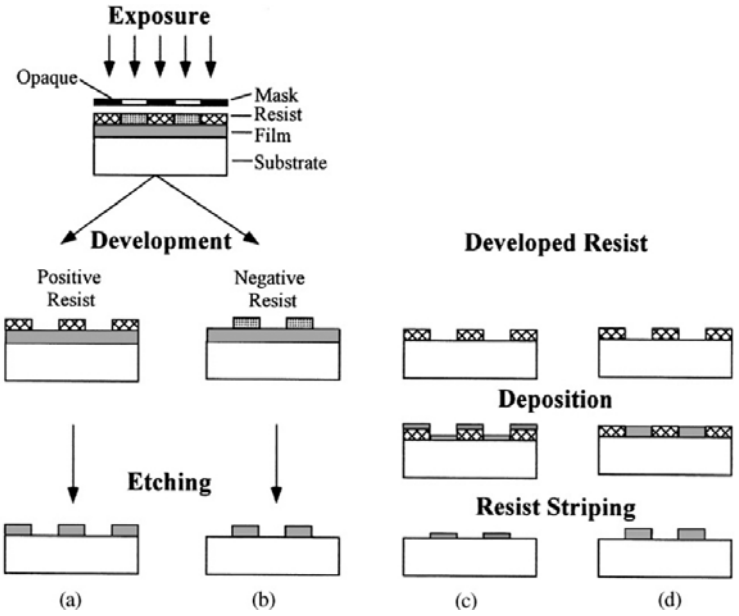

Figure 1.1. *Schematic illustration of diverse lithography processes for (a) positive and (b) negative resists together with (a) and (b) etching processes, (c) liftoff, and (d) electrodeposition. Adapted from reference [1]. Note that parts in grey correspond to magnetic material.*

In a major classification, after developing the resist and thus leaving a mask onto either a magnetic film or a non-magnetic substrate, two general routes are distinguished during the pattern transfer from the resist to the specimen to produce arrays of magnetic entities: (i) from the template to a continuous magnetic film by etching (subtractive processes of magnetic material in order to produce a pattern, see panels (a) and (b) of Figure 1.1) or (ii) post-deposition or growth of magnetic material (additive processes, see panels (c) and (d)).

Concerning (i), wet and dry etching are regularly used. Wet etching uses specific chemical or electrochemical processes [2] to dissolve selectively both the non-covered magnetic film and the remaining resist, which constitutes the pattern, thus leaving only the magnetic material below the developed resist (see panels (a) and (b) of Figure 1.1). In dry etching, the removal of the undesired parts is usually achieved by means of either physical processes, such as ion milling, which uses ion bombardment to sputter material, or chemical, such as plasma etching, which utilizes specific components to

react with the surface to form volatile products. A combination of both processes, such as reactive ion milling, takes advantage of both processes. Nevertheless, since most magnetic materials are difficult to etch using reactive ion etching [3], sputter etching processes are more frequently employed for patterning magnetic nanostructures.

On the other hand, ordered magnetic nanostructures can be also fabricated by additive processes (e.g., post-lithography deposition or growth, route (ii)) taking advantage of the topography of the developed resist. Evaporation followed by liftoff and electrodeposition have been the most widely used methods for producing magnetic arrays. In fact, evaporation is commonly used to produce flat structures which are usually much thinner than the polymeric resist and, usually, it is followed by a liftoff procedure. During resist stripping, which corresponds to the process to remove the polymeric template, the material on top of the resist is lifted off, thus leaving the portions directly deposited onto the substrate (i.e., liftoff process). It should be noted that liftoff is a general process, not only linked to conventional lithography, which takes advantage of the height of any template to divide the deposit material, which is thinner than the template thickness, and, hence, leaves only the material deposited at the holes of this template. In contrast, electrodeposition, which refers to the deposition of materials from an electrolyte by using electrical current, is mainly used when structures with high vertical aspect ratios (height/width) are wanted (i.e., structures with a high vertical dimension compared to the horizontal side). In this case, the material is selectively deposited in the holes left by the template. Then, the polymeric layer is stripped away.

Pattern generation on the polymeric resist layer can be accomplished by several techniques, such as electron-beam lithography, laser interference lithography, X-ray lithography or nanoimprint lithography, where, for instance, the lithography resolution is ultimately limited by the utilized physical process, e.g., the employed radiation wavelength [1]. It should be mentioned that although near-field photolithography is also able to produce ultrafine entities (below the sub-100 nm regime), it is not considered here since optical lithography has not been fully employed in magnetic systems [4].

Electron beam lithography (e-beam lithography) has been the most widely utilized patterning method for magnetic nanostructure fabrication down to dimensions of around 15 nm and above. Commonly, the electron beam of a scanning electron microscope (SEM) is used to write structures onto a polymethylmethacrilate (PMMA) resist, one of the most broadly used positive resist, which is then developed to leave the desired template. To obtain different magnetic nanostructures, the e-beam lithography has been used with diverse general lithography processes, such as evaporation followed by liftoff or electrodeposition. In particular, this technique is characterized by its versatility for the fabrication of different entity shapes, although it suffers from the drawback that it is a serial method. Although e-beam lithography is not suitable for making large patterned areas [3], it is excellent for producing prototypes due to its resolution. A large number of magnetic nanostructures have been fabricated by e-beam lithography, combined with liftoff, which has been mainly focused to obtain planar polycrystalline magnetic structures, such as Co [5-8], Fe [9], Ni [5], NiFe [8,10-12], etc. Furthermore, multilayered structures have been also produced, such as Co/Pt with out-of-plane anisotropy [13] or Co/Au/Ni [14]. Moreover, in combination with electrodeposition, it allows fabricating structures with high vertical aspect ratios, for instance, Ni pillars [15].

Electron beam lithography has been also employed in combination with etching processes, which allow fabricating magnetic nanostructures not only from polycrystalline films, such as Co [16] or NiFe [17], but also from epitaxial magnetic layers, such as Fe (001) [18] or Co (0001) [19].

Similar to electron beam lithography, interference lithography is based on the selective and direct exposure of a resist layer. This method uses the interference of two coherent laser beams, which produce a pattern of parallel lines, to locally expose the resist. In order to get different morphologies, subsequent exposures must be performed and the sample re-orientated to the desired position in order to define a certain shape according with the previous linear pattern. This method allows obtaining large patterned areas with a high symmetry of structures. In fact, this technique can be performed together with conventional lithography processes for magnetic pattern transfer. For example,

using this method, NiCr structures have been prepared by evaporation and liftoff or arrays of Ni pillars by electrodeposition [20].

X-ray lithography is based on the use of soft X-rays to irradiate selectively a resist-coated material (e.g., with PMMA) through a thin membrane mask (typically made of silicon nitride or diamond due to its transparency to X-rays and with a thickness of around 2 μm), which is placed in proximity (around a few micrometers) to the sensitive resist. The features to be transferred to the resist are made from an absorber (element with high atomic number) of X-ray radiation, typically of gold or compounds of tantalum or tungsten. In order to reduce the exposing time, intense X-ray sources, such as a synchrotron facility, are utilized to enable a high throughput. This technique allows obtaining large patterned areas since the mask can cover several square centimeters and the mask can be continuously used with its lifetime limited by deterioration. After developing the polymeric resist, the magnetic nanostructures are obtained using the abovementioned general pattern transfer processes. For example, polycrystalline NiFe dots have been obtained by liftoff [21], Co (0001) [22] by etching or Ni-Cu/Cu (100) multilayered structures by electrodeposition [23].

Another important technique is nanoimprint lithography, which is also capable to fabricate large patterned areas. This process is based on the parallel generation of structures by imprinting a rigid pre-patterned mold onto a resist. Namely, this mold is employed to deform physically the resist in order transfer the pattern of the mold to it. In general, the imprint resist is typically a polymer formulation that is cured by heat or ultraviolet light during the stamping process. Note that an unavoidable residual layer remains in the produced holes, which is usually removed by sputter etching. Magnetic nanostructures, such as Ni columns [24], have been prepared using this method in conjunction with electrodeposition.

In both X-ray lithography and nanoimprint, a template or a master mold of a hard material must first be patterned, for example, by means of e-beam lithography, but the large number of uses made from each mask or mold justifies the time-consuming process of the previous pre-patterning process.

Another common technique to produce pseudo-ordered magnetic structures utilizes self-assembling processes of diblock copolymers at the top of the selected working specimen. A block copolymer, which is formed of two chemically different monomeric species, is spin-coated at the surface of the sample. Since both monomers are chemically different, taking advantage of chemical processes or radiation, one of these monomers can be selectively broken or hardened and, then, removed to form a template. Next, the diverse routes for magnetic pattern transfer can be used, such as etching of a magnetic film or it can be used as a growth matrix. For example, Co nanowires have been prepared by elecrodeposition [29].

In contrast to the already described techniques, which are essentially based on a patterning process of a polymeric layer directly deposited on the material of interest, another important way to pattern magnetic nanostructures relies on the use of ex-situ shadow masks to etch magnetic material or as a template for deposition of magnetic material. Note that these masks act in a similar way as the lithographed resists mentioned before. In fact, the transferring techniques described above (i.e., liftoff, electrodeposition, etc.) are also utilized. Many types of shadow masks have been used. For example, alumina membranes, prepared by anodization processes [25], which consist of pseudo-ordered arrays of cylindrical pores in the nanometer scale, are widely used for nanostructure fabrication. For example, Fe nanodots were prepared by deposition and liftoff of alumina membranes [26]. In this method, high-density of pores can be obtained over a large area of the order of 1-10 cm^2, depending on the size of the template, which allow obtaining a large patterned area of magnetic nanostructures in a parallel process.

Finally, it should be noted that there are several different but less common nanofabrication techniques which are not reviewed. Nevertheless, extensive information can be found in specialized reviews, such as reference [1]. Furthermore, it is worth nothing that the above techniques result concomitantly in both a magnetic and topographic pattern.

1.1.2. Direct methods

Even though most of the techniques to produce arrays of magnetic structures arranged in ordered or pseudo-ordered configurations use a template to transfer the desired topography, other techniques can directly write the structures without using an intermediate layer. In general, these techniques are rather time-consuming since they are serial processes. Moreover, most of them have been only utilized as a proof-of-principle of their capabilities to produce magnetic patterning as prototypes.

For instance, an electron beam itself has been used to produce arrays of magnetic nanostructures in certain deposited films, such as FeF_2 or CoF_2 [30]. The interaction between the electrons and these materials results in the liberation of the F atoms, thus leaving isolated islands composed by the magnetic elements (i.e., Fe or Co) at zones which interact with the electron beam. In addition, a more complex way to produce a direct pattern using an e-beam relies on the use of an organometallic gas with a magnetic element in the SEM chamber. The e-beam acts dissociating the precursor gas and leads to the fabrication of magnetic entities where the e-beam and the gas interact [31].

Scanning probe microscopes, such as atomic force microscopes (AFM) or scanning tunneling microscopes (STM), have been also utilized to locally pattern magnetic structures. Either AFM or STM tips, coated or made of magnetic material, have been employed to transfer, by means of voltage pulses, part of their magnetic material to localized places of the substrate to be patterned [32]. Furthermore, if an organometallic gas containing the desired magnetic atom is added in the STM chamber, voltage pulses between the tip and the substrate can be applied in order to dissociate the gas and, subsequently, produce localized amounts of magnetic material. Actually, this technique is known as STM chemical vapor deposition [33]. Finally, if the substrate to be patterned is immersed in an electrochemical cell, the STM tip can be used as an electrode to electrodeposit locally magnetic material [34].

Another direct technique is focused ion beam milling. Since ion beam can be highly focused, material removal of a continuous film can be selectively done. For example, arrays of dots from CrCoPt-based films have been prepared using this method [35].

Note that in most of the above examples the patterning is at the same time magnetic and topographic.

1.2. Local control of magnetic properties by ion irradiation

Even though in the previous sub-section ion irradiation has been already presented as a possible method for production of magnetic nanostructures, special attention is given here since ion irradiation may lead to a new way to produce a pure magnetic patterning without any significant topography modification [36]. Nevertheless, it is worth mentioning that either lithographed layers [37] or pseudo-ordered membranes [38] are usually employed in this purely magnetic approach, although with the specific purpose to act as a shadow mask of the incoming ion irradiation.

As has been discussed in section 1.1.1., conventional processes for nanostructure fabrication usually involve either the deposition or growth of magnetic materials inside lithographically fabricated polymeric layers or nanoporous membranes or the mask-controlled selective etching of continuous films. In the late 90s, a new concept for the fabrication of magnetic nanostructures was proposed, i.e., magnetic patterning rather than topographic patterning [37]. Namely, by using ion irradiation, the local magnetic properties of Co/Pt multilayers were manipulated, rendering a material with locally dissimilar magnetic properties [37]. Interestingly, the concomitant ion-induced erosion of the surface may be minimized by means of this approach, leading to magnetic entities without topographic features, which can be interesting for certain applications, such as magnetic recording media.

Since the original report, several designs of such magnetic patterning have been proposed, e.g., nanostructures with in-plane anisotropy embedded in an out-of-plane anisotropy matrix [37,39-42], soft nanostructures in a hard magnetic matrix or vice-

versa [37,43-47], patterns with a different in-plane anisotropy than the matrix [48,49], patterns with locally different saturation magnetizations [50] and nanostructures with exchange bias different from the matrix [51-53]. However, all these strategies are composed of ferromagnetic structures embedded in a ferromagnetic matrix, which will inevitably lead to exchange interactions between the dots and the matrix. In fact, these interactions might be detrimental for certain applications, since the magnetization reversal of the nanostructures may lead to the switching of the matrix. A more appealing structure would be embedding ferromagnetic dots in a paramagnetic matrix. Four different systems with this magnetic structure have been reported in ultrathin Co layers sandwiched between Pt layers [37,54], $Co_{90}Fe_{10}$ thin films [55], CoCrPt/Cr multilayers [56], or $Ni_{80}Fe_{20}$ thin films [57]. All four processes are based on the destruction of the magnetism of the layers by irradiation-induced severe structural damage or irradiation-induced alloying, which commonly require rather large irradiation fluences (usually in excess of 1-80 displacements per atom, dpa, see chapter 2). At such large fluences, the surface roughness of the films often increases [37,54-57].

Therefore, the production of patterned magnetic materials composed of ferromagnetic entities embedded in a paramagnetic matrix without significant topography differences still remains rather challenging.

1.3. Induced magnetism in non-magnetic alloys

In this section, the origin of ferromagnetism in either paramagnetic $Fe_{60}Al_{40}$ (at. %) alloys or austenitic stainless steels will be briefly discussed.

1.3.1. Ferromagnetism induced by atomic disordering in $Fe_{60}Al_{40}$ (at. %) alloys

$Fe_{60}Al_{40}$ (at. %) alloys show an interesting combination of structural and magnetic properties. In their atomically ordered state (B2-phase), $Fe_{60}Al_{40}$ alloys consist of a body-centered cubic (BCC) structure with the Fe and the Al atoms localized in well-

defined positions. That is, one of the atomic species located at the center of the lattice and the other type of atoms at the corners. Nevertheless, note that 10 % of Fe atoms must remain in Al sites to preserve the stoichiometry of the alloy. This ordered state is paramagnetic at room temperature. Conversely, when these alloys are atomically disordered, an intermixing process between Fe and Al atoms occurs, resulting in the so-called A2-phase, which is ferromagnetic. Since this system may exist in intermediate states where the degree of ordering is not complete, the above phase transition is partially accomplished and, at the same time, the induced ferromagnetism scales accordingly [58-61].

In the case of the $Fe_{1-x}Al_x$ (at. %) system, the room temperature magnetic moment of the atomically ordered alloy decreases slowly when increasing the Al content, in agreement with dilution models, up to x = 0.2. With further dilution with aluminum, the magnetic moment decreases more rapidly, becoming zero for alloys with $x \geq 0.32$ (see Figure 1.2). Nevertheless, atomically ordered $Fe_{1-x}Al_x$ alloys with $x > 0.32$ are able to become ferromagnetic, at room temperature, after being disordered (i.e., atomically intermixed) [62].

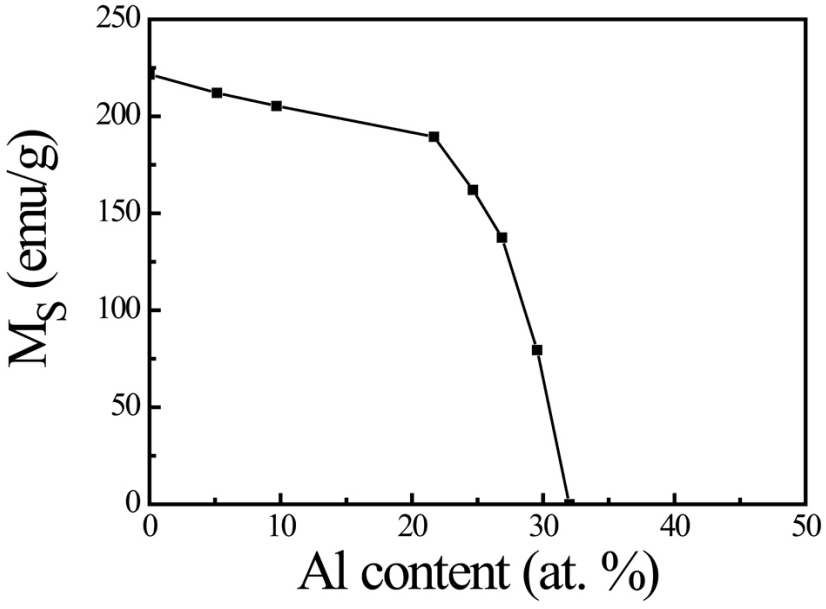

Figure 1.2. *Aluminum content dependence of the saturation magnetization, M_S, for the $Fe_{1-x}Al_x$ system. Adapted from reference [62].*

From a theoretical basis, the ferromagnetism of diluted and disordered transition metal alloys, such as $Fe_{60}Al_{40}$, has been partially explained by the so-called local environment model [63-65], which takes into account that the magnetic moment of a given atom (i.e., Fe in this case) depends on the number of nearest-neighbor atoms of the same species. Using this simple model, the effect of Al substitution and disorder in $Fe_{60}Al_{40}$ can be qualitatively explained.

However, since variations in the distance between transition metal atoms, such as Fe, have profound effects on the magnetism, it has been shown that the origin of the magnetic interactions in disordered $Fe_{60}Al_{40}$ alloys may not arise solely from nearest-neighbors magnetism (i.e., local environment model), but also from changes in the band structure of the material induced by changes in the lattice cell parameter (Δa) [59-61, 66-69]. Therefore, a two-fold origin of ferromagnetism is distinguished.

1.3.2. Ferromagnetism induced by structural phase transformations in austenitic stainless steels

Austenitic stainless steels (ASSs) are Fe-based alloys (see appendix for further information) which consist of a face-centered cubic (FCC) crystal lattice, designated as austenite (γ) phase. From a magnetic point of view, ASSs show paramagnetic behavior at room temperature, while they become antiferromagnetic below their Néel temperature, which is around 40 K [70].

However, due to strain-induced deformation, a phase transformation from the FCC austenite to a body-centered cubic (BCC) crystal structure, known as martensite (α'), can occur in these alloys. Since martensite is ferromagnetic [71-73], this stress-induced phase transformation also results in a magnetic transition at room temperature from paramagnetic γ to ferromagnetic α' ($\gamma \rightarrow \alpha'$). Although the extent of the α' transformation depends mainly on the chemical composition of the steel and the temperature at which the plastic deformation takes place, it should be noted that other important factors affecting this strain-induced phase transformation are the strain rate, grain size and deformation mode (i.e., stress state). In fact, the extent of this

transformation (i.e., $\gamma \rightarrow \alpha'$) in different grades of austenitic stainless steels can be roughly shown in decreasing order as 304L >> 316 > 316L (see appendix for compositional details) when deformed to the same amount at a given temperature [74].

Furthermore, nitriding of ASSs at moderate temperatures (around 400 ºC) leads to the formation of the supersaturated nitrogen solid solution, often called in the literature "expanded austenite" or γ_N phase [75,76], which is responsible for both microhardness and wear resistance enhancement without loss of corrosion resistance. Remarkably, this phase shows ferromagnetic behavior, whose origin is linked to the expansion of the austenite (γ) lattice due to the incorporation of nitrogen atoms into interstitial positions [77]. Since the threshold for ferromagnetism is connected with nitrogen concentrations of $\approx$ 10-15 at. % [75,77], for thick specimens not the whole nitrided layer is ferromagnetic, thus rendering two magnetically dissimilar parts (one ferromagnetic and the other paramagnetic) depending on the nitrogen concentration along the depth of the nitrided surface layer.

References

[1] J. I. Martín, J. Nogués, K. Liu, J. L. Vicent and I. K. Schuller *J. Magn. Magn. Mater.* **256** 449 (2003)

[2] *Thin Film Processes*, edited by J. L. Vossen and W. Kern (Academic Press, New York, 1978)

[3] C. A. Ross *Annu. Rev. Mater. Res.* **31** 203 (2001)

[4] T. Pokhil, D. Song and J. Nowak *J. Appl. Phys.* **87** 6319 (2000)

[5] J. I. Martín, Y. Jaccard, A. Hoffmann, J. Nogués, J. M. George, J. L. Vicent and I. K. Schuller *J. Appl. Phys.* **84** 411 (1998)

[6] T. Schrefl, J. Fidler, K. J. Kirk and J. N. Chapman *J. Magn. Magn. Mater.* **175** 193 (1997)

[7] Y. Otani, S. G. Kim, T. Kohda and K. Fukamichi *IEEE Trans. Magn.* **34** 1090 (1998)

[8] J. Raabe, R. Pulwey, R. Sattler, T. Schweinböck, J. Zweck and D. Weiss *J. Appl. Phys.* **88** 4437 (2000)

[9] P. Vavassori, V. Metlushko, M. Grimsditch, B. Ilic, P. Neuzil, R. Kumar, *Phys. Rev. B* **61** 5895 (2000)

[10] Y. Yokoyama, Y. Suzuki, S. Yuasa, K. Ando, K. Shigeto, T. Shinjo, P. Gogol, J. Millat, A. Thiaville, T. Ono and T. Kawagoe *J. Appl. Phys.* **87** 5618 (2000)

[11] K. J. Kirk, J. N. Chapman, S. McVitie, P. R. Aitchison and C. D. W. Wilkinson *J. Appl. Phys.* **87** 5105 (2000)

[12] M. Schneider, H. Hoffmann and J. Zweck *Appl. Phys. Lett.* **77** 2909 (2000)

[13] T. Ono, H. Miyajima, K. Shigeto and T. Shinjo *J. Magn. Magn. Mater.* **198&199** 225 (1999)

[14] D. J. Smith, R. E. Dunin-Borkowski, M. R. McCartney, B. Kardynal and M. R. Scheinfein *J. Appl. Phys.* **87** 7400 (2000)

[15] S. Y. Chou, M. S. Wei, P. R. Krauss and P. B. Fischer *J. Appl. Phys.* **76** 6673 (1994)

[16] R. M. H. New, R. F. W. Pease and R. L. White *J. Vac. Sci. Technol. B* **12** 3196 (1994)

[17] C. C. Yao, D. G. Hasko, Y. B. Xu, W. Y. Lee and J. A. C. Bland *J. Appl. Phys.* 85 1689 (1999)

[18] C. Shearwood, S. J. Blundell, M. J. Baird, J. A. C. Bland, M. Gester, H. Ahmed and H. P. Hughes *J. Appl. Phys.* **75** 5249 (1994)

[19] H. Demand, M. Hehn, K. Ounadjela, R. L. Stamps, E. Cambril, A. Cornette and F. Rousseaux *J. Appl. Phys.* **87** 5111 (2000)

[20] T. A. Savas, M. Farhoud, H. I. Smith, M. Hwang and C. A. Ross *J. Appl. Phys.* **85** 6160 (1999)

[21] C. Miramond, C. Fermon, F. Rousseaux, D. Decanini and F. Carcenac *J. Magn. Magn. Mater.* **165** 500 (1997)

[22] N. Bardou, B. Bartenlian, F. Rousseaux, D. Decanini, F. Carcenac, E. Cambril, M. F. Ravet, C. Chappert, P. Veillet, P. Beauvillain, R. Mégy, W. Geerts and J. Ferré *J. Magn. Magn. Mater.* **156** 139 (1996)

[23] W. Schwarzacher, O. I. Kasyutich, P. R. Evans, M. G. Darbyshire, G. Yi, V. M. Fedosyuk, F. Rousseaux, E.Cambril and D. Decanini *J. Magn. Magn. Mater.* **198-199** 185 (1999)

[24] W. Wu, B. Cui, X. Sun, W. Zhang, L. Zhuang, L. S. Kong and S. Y. Chou *J. Vac. Sci. Technol. B* **16** 3825 (1998)

[25] A. P. Li, F. Muller, A. Birner, K. Nielsch and U. Gosele *J. Appl. Phys.* **84** 6023 (1998)

[26] K. Liu, J. Nogués, C. Leighton, H. Masuda, K. Nishio, I. V. Roshchin and I. K. Schuller *Appl. Phys. Lett.* **81** 4434 (2002)

[27] H. R. Khan and K. Petrikowski *J. Magn. Magn. Mater.* **215-216** 526 (2000)

[28] P. R. Evans, G. Yi and W. Schwarzacher *Appl. Phys. Lett.* **76** 481 (2000)

[29] T. Thurn-Albercht, J. Schotter, G. A. Kästle, N. Emley, T. Shibauchi, L. Krusin-Elbaum, K. Guarini, C. T. Black, M. T. Tuominen and T. P. Russell *Science* **290** 2126 (2000)

[30] D. Streblechenko and M. R. Scheinfein *J. Vac. Sci. Technol. A* **16** 1374 (1998)

[31] D. Welipitiya, C. N. Borca, P. A. Dowben, I. Gobulukoglu, H. Jiang, B. W. Robertson and J. Zhang *Mat. Res. Soc. Symp. Proc.* **475** 257 (1997)

[32] K. Bessho, Y. Iwasaki and S. Hashimoto *J. Appl. Phys.* **79** 5057 (1996)

[33] S. Wirth, J. J. Heremans, S. von Molnár, M. Field, K. L. Campman, A. C. Gossard and D. D. Awschalom *IEEE Trans. Magn.* **34** 1105 (1998)

[34] W. Schindler, D. Hofmann and J. Kirshner *J. Appl. Phys.* **87** 7007 (2000)

[35] K. Koike, H. Matsuyama, Y. Hirayama, K. Tanahashi, T. Kanemura, O. Kitakami and Y. Shimada *Appl. Phys. Lett.* **78** 784 (2001)

[36] J. Fassbender and J. McCord *J. Magn. Magn. Mater.* **320** 579 (2008)

[37] C. Chappert, H. Bernas, J. Ferre, V. Kottler, J. P. Jamet, Y. Chen, E. Cambril, T. Devolder, F. Rousseaux, V. Mathet and H. Launois *Science* **280** 1919 (1998)

[38] S. W. Shin, S. G. Lee, J. Lee, C. N. Whang, J. H. Lee, I. H. Choi, T. G. Kim and J. H. Song *Nanotechnology* **16** 1392 (2005)

[39] B. D. Terris, L. Folks, D. Weller, J. E. E. Baglin, A. J. Kellock, H. Rothuizen and P. Vettiger *Appl. Phys. Lett.* **75** 403 (1999)

[40] S. Konings, J. Miguel, J. Goedkoop, J. Camarero and J. Vogel *J. Appl. Phys.* **100** 033904 (2006)

[41] M. Abes, J. Venuat, A. Carvalho, J. Arabski, D. Muller, G. Schmerber, E. Beaurepaire, P. Panissod, A. Dinia and V. Pierron-Bohnes *J. Magn. Magn. Mater.* **286** 297 (2005)

[42] G. J. Kusinski, K. M. Krishnan, G. Denbeaux and G. Thomas *Scr. Mater.* **48** 949 (2003)

[43] B. D. Terris, D. Weller, L. Folks, J. E. E. Baglin, A. J. Kellock, H. Rothuizen and P. Vettiger *J. Appl. Phys.* **87** 7004 (2000)

[44] T. Hasegawa, G. Q. Li, W. Pei, H. Saito, S. Ishio, K. Taguchi, K. Yamakawa, N. Honda, K. Ouchi, T. Aoyama and I. Sato *J. Appl. Phys.* **99** 053505 (2006)

[45] D. Ozkaya, R. M. Langford, W. L. Chan and A. K. Petford-Long *J. Appl. Phys.* **91** 9937 (2002)

[46] M. Albrecht, C. T. Rettner, M. E. Best and B. D. Terris *Appl. Phys. Lett.* **83** 4363 (2003)

[47] A. Dietzel, R. Berger, H. Loeschner, E. Platzgummer, G. Stengl, W. H. Bruenger and F. Letzkus *Adv. Mater.* **15** 1152 (2003)

[48] S. I. Woods, S. Ingvarsson, J. R. Kirtley, H. F. Hamann and R. H. Koch *Appl. Phys. Lett.* **81** 1267 (2002)

[49] J. McCord, T. Gemming, L. Schultz, J. Fassbender, M. O. Liedke, M. Frommberger and E. Quandt *Appl. Phys. Lett.* **86** 162502 (2005)

[50] J. Fassbender, J. von Borany, A. Muecklich, K. Potzger, W. Möller, J. McCord, L. Schultz and R. Mattheis *Phys. Rev. B* **73** 184410 (2006)

[51] A. Mougin, S. Poppe, J. Fassbender, B. Hillebrands, G. Faini, U. Ebels, M. Jung, D. Engel, A. Ehresmann and H. Schmoranzer *J. Appl. Phys.* **89** 6606 (2001)

[52] J. Fassbender, D. Ravelosona and Y. Samson *J. Phys. D: Appl. Phys.* **37** R179 (2004)

[53] K. Theis-Bröhl, M. Wolff, A. Westphalen, H. Zabel, J. McCord, V. Hoeink, J. Schmalhorst, G. Reiss, T. Weis, D. Engel, A. Ehresmann, U. Rucker and B. P. Toperverg *Phys. Rev. B* **73** 174408 (2006)

[54] T. Aign, P. Meyer, S. Lemerle, J. P. Jamet, J. Ferre, V. Mathet, C. Chappert, J. Gierak, C. Vieu, F. Rousseaux, H. Launois and H. Bernas *Phys. Rev. Lett.* **81** 5656 (1998)

[55] D. McGrouther and J. N. Chapman *Appl. Phys. Lett.* **87** 022507 (2005)

[56] M. T. Georgieva, P. J. Grundy and N. D. Telling *Appl. Phys. Lett.* **90** 042509 (2007)

[57] W. M. Kaminsky, G. A. C. Jones, N. K. Patel, W. E. Booij, M. G. Blamire, S. M. Gardiner, Y. B. Xu and J. A. C. Bland *Appl. Phys. Lett.* **78** 1589 (2001)

[58] G. K. Wertheim, V. Jaccarino, J. H. Wernick and D. N. E. Buchanan *Phys. Rev. Lett.* **12** 24 (1964)

[59] E. P. Yelsukov, E.V. Voronina and V. A. Barinov *J. Magn. Magn. Mater.* **115** 271 (1992)

[60] X. Amils, J. Nogués, S. Suriñach, M. D. Baró and J. S. Muñoz *IEEE Trans. Magn.* **34** 1129 (1998)

[61] A. Hernando, X. Amils, J. Nogués, S. Suriñach, M. D. Baró and M. R. Ibarra *Phys. Rev. B Rapid Comm.* **58** R11864 (1998)

[62] A. Taylor and R. M. Jones *J. Phys. Chem. Solids* **6** 16 (1958)

[63] P. A. Beck *Metall. Trans.* **2** 2015 (1971)

[64] G. K. Wertheim, V. Jaccarino, J. H. Wernick and D. N. E.Buchanan *Phys. Rev. Lett.* **12** 24 (1964)

[65] S. Takahashi *J. Magn. Magn. Mater.* **54-57** 1065 (1986)

[66] M. Fujii, K. Saito, K. Wakayama, M. Kawasaki, T. Yoshioka, T. Isshiki, N. Nishio and M. Shiojiri *Philos. Mag. A* **79** 2013 (1999)

[67] A. V. Smirnov, W. A. Shelton and D. D. Johnson *Phys. Rev. B* **71** 064408 (2005)

[68] E. Apiñaniz, F. Plazaola and J. S. Garitaonandia *Eur. Phys. J. B* **31** 167 (2003)

[69] J. Nogués, E. Apiñaniz, J. Sort, M. Amboage, M. d'Astuto, O. Mathon, R. Puzniak, I. Fita, J. S. Garitaonandia, S. Suriñach, J. S. Muñoz, M. D. Baró, F. Plazaola and F. Baudelet *Phys. Rev. B* **74** 024407 (2006)

[70] J. Ding, H. Huang, P. G. McCormick and R. Street *J. Magn. Magn. Mater.* **139** 109 (1995)

[71] S. S. Hecker, M. G. Stout, K. P. Staudhammer and J. L. Smith *Metall. Trans. A* **13** 619 (1982)

[72] E. Nagy, V. Mertinger, F. Tranta and J. Sólyom, *Mater. Sci. Eng. A* **378** 308 (2004)

[73] H. Ishigaki, Y. Konishi, K. Kondo and K. Koterazawa *J. Magn. Magn. Mater.* **193** 466 (1999)

[74] J. Manjanna, S. Kobayashi, Y. Kamada, S. Takahashi and H. Kikuchi *J. Mater. Sci.* doi:10.1007/s10853-008-2494-4

[75] M.P. Fewell, D. R. G. Mitchell, J. M. Priest, K. T. Short and G. A. Collins *Surf. Coat. Technol.* **131** 300 (2000)

[76] G. Abrasonis, J. P. Riviere, C. Templier, A. Declemy, L. Pranevicius and X. Milhet *J. Appl. Phys.* **97** 083531 (2005)

[77] O. Öztürk and D. L. Williamson *J. Appl. Phys.* **77** 3839 (1995)

2. Experimental methods

This chapter describes the experimental procedures that have been used to induce ferromagnetism in $Fe_{60}Al_{40}$ (at. %) alloys and austenitic stainless steels (ASSs) by means of either plastic deformation (mechanical milling and compression testing) or ion irradiation (broad beam ion irradiation and focused ion beam). Subsequently, the techniques for structural, morphological, mechanical, and magnetic characterization are surveyed.

In each section, the employed setups for either material processing or characterization are specified. Although the specific experimental details will be concisely presented at the beginning of each section of the *Results and discussion* chapter, a brief description of the main working conditions is given here.

2.1. Processing methods

2.1.1. Mechanical milling

2.1.1.1. Fundamentals

Mechanical milling is a solid state powder treatment technique involving repeated welding, fracturing, and re-welding of powder particles in a high-energy ball mill [1]. In most cases, this processing route has been successfully utilized to produce many types of solid solutions, materials in non-equilibrium states [2,3], disordered and amorphous alloys, and to induce mechanochemical reactions [4]. Furthermore, mechanical milling has established itself as a very effective process for producing nanocrystalline powders and synthesizing metal-ceramic composite powders [1,5].

Even though a large variety of milling devices, such as shaker (e.g., *Spex* mills), attritor or magnetic mills, are currently often used, this section is focused on planetary-like ball mills since a planetary ball mill (see Figure 2.1) has been used to treat the AISI 316L ASS powders. Moreover, this type of milling apparatus is characterized by their capability to carry out very energetic processes.

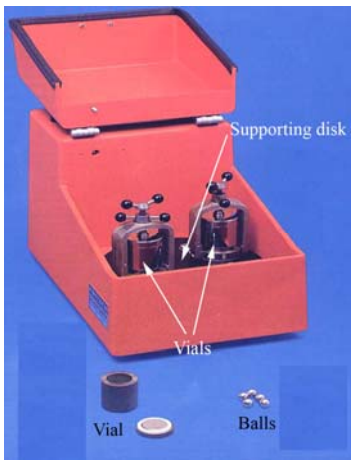

***Figure 2.1**. Photograph of the employed planetary ball mill (Fritsch Pulverisette 7). Note that the milling chamber contains a disk with two symmetrically located grinding bowls (vials).*

Concerning the operational principle, a powder load is introduced in one or more vials (grinding bowls), which are arranged, together with some balls, on a rotating support disk. After appropriate sealing, the vials rotate around their own axis and, simultaneously, around a central axis, similar to a planetary system [1,4,6]. Since the vials and the supporting disk rotate in opposite directions, the centrifugal forces of the two movements act alternately in the same and opposite directions. This causes the grinding balls to run down the inner wall of the vial –the friction effect–, followed by the material being ground and grinding balls lifting off and traveling through the inner chamber of the vial and colliding against the opposing internal wall –the impact effect– (see Figure 2.2) [1].

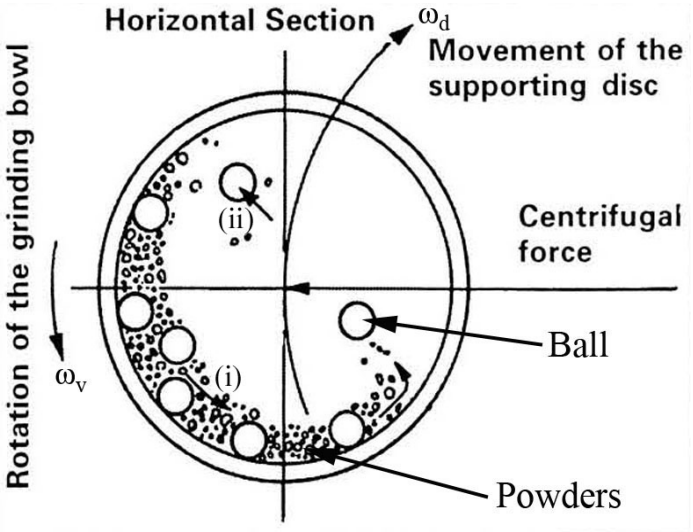

***Figure 2.2**. Schematic diagram of balls and powders movements in a planetary ball mill [1]. (i) and (ii) stand for the grinding and impact effects, respectively. ω_d and ω_v are the angular frequencies of the supporting disk and the vials, respectively.*

2.1.1.2. Milling parameters

The main experimental parameters that must be taken into account in order to control the final products of a milling process are:

- Intensity (transferred power)
- Atmosphere
- Media

- Temperature

2.1.1.2.1. Intensity (transferred power)

Several theoretical models have been developed in order to evaluate the milling intensity I (i.e., the power transferred to the load) [7]. Even though these models can differ noticeably due to their particular simplifications and approximations, I is often estimated using an expression which contains the following parameters:

$$I = \nu \cdot \Delta E \cdot n \cdot f \quad \text{(Eq. 2.1)},$$

whit ΔE being the dissipated energy in a system containing n balls, ν a variable less than unity, whose value depends on the volume occupied by the balls inside the vials, and f the frequency at which the balls are thrown to the opposite walls of the vials, which, in the case of a planetary mill, is a function of the angular frequencies of the supporting disk and the vials, ω_d and $\omega_{v,}$ respectively.

If one considers simplified models in which the energy can only be dissipated during the impacts between the balls and the walls of the vials, ΔE only depends on some intrinsic parameters of the planetary mill, such as the distance between the center of the disk and walls of the vials, and the distance between the center of the disk and the center of the vials [8,9]. Moreover, there are other relevant parameters, such as the ball-to-powder mass ratio or the milling time, that play an important role in the amount of energy transferred and, therefore, in controlling the final properties of the milled material [1].

2.1.1.2.2. Milling atmosphere

The control of the milling atmosphere is of great importance, since lack of it can lead to some undesired mechanochemical reactions or contamination in the obtained materials. For instance, if the milling is performed in air, a significant contamination from oxygen or nitrogen can be obtained [10]. Usually these effects are not desirable and, therefore,

the milling process is commonly carried out under vacuum or in an inert gas, such as argon or helium.

2.1.1.2.3. Milling media

The contamination arising from the milling media (vials and balls) can also be significant during the material processing. The amount of this type of contamination depends mainly on how energetic is the milling process and also on the mechanical properties (e.g., hardness) of the powders that are being ground with respect to those corresponding to the milling media [11]. Nevertheless, this problem can be almost ignored when the milling media are built up from the same material as the powders [12].

2.1.1.2.4. Milling temperature

In milling, the exchange of energy during both the friction and impact effects usually brings about a heating of the powders, which can, undoubtedly, affect their microstructure [4,12]. Essentially, this temperature increase is observed locally at the surface of the particles and is usually known as microscopic temperature rise. Moreover, an overall heating in the milling media, due to the motor, the friction among the components of the mill or the impacts between the vial and the balls, can be also detected (i.e., macroscopic temperature rise).

The macroscopic temperature increase that can be observed in the different types of milling apparatus is generally not very high and has been measured by several authors. For example, the average temperature during milling has been reported to be of up to 50 ºC for *Spex* mills, 120 ºC for vibratory mills and 172 ºC for attritor mills [4].

Conversely, the microscopic temperature of the powders, just after each impact, can be really high. Actually, it is unfeasible to directly measure this temperature and, for that reason, its values can only be inferred by using some theoretical models or by analyzing the microstructural changes which take place in the powders upon milling. For instance,

Schwarz and Koch estimated a temperature increase (with respect to room temperature) of 350 ºC for *Spex*-type mills [13]. Magini et al. calculated that the temperature rise could reach up to 400 ºC for planetary mills [14].

Although a wide range of microscopic temperature increases have been reported in the literature, the macroscopic temperature (and to a certain extent the microscopic one) can be occasionally controlled by means of refrigerating circuits [4].

2.1.1.3. Temporal evolution of the microstructure

Typically, in materials subjected to mechanical work in high energetic mills, the final distribution of particle sizes and shapes, after long-term milling, becomes rather stable due to the continuous processes of fracture and welding. The particle size distribution and particle morphology depend on the kind of material being processed as well as the milling intensity, the ball-to-powder mass ratio, temperature, etc. However, the homogenization process varies depending on the ductility or brittleness of the milled powders. Thus, very different microstructures are frequently obtained when the precursor powders are ductile, brittle or two-component brittle-ductile.

Most of alloys synthesized by ball milling are of ductile character, such as AISI 316L ASSs. In this case, the particles increase in size up to a maximum value and, then, tend to progressively reduce until an equilibrium dimension is reached. This behavior can be interpreted as the interplay between fracture and welding mechanisms. Hence, during the first milling stages, owing to the ductility of the powders, soldering predominates over fracturing. However, for long-term milling, both processes tend to reach some equilibrium, leading to a stationary particle size distribution. Furthermore, during milling, the particles first become elongated and later they develop in platelet or laminar shapes. As the milling time increases, the interlaminar distances decrease, the microstructure becomes more and more refined and, finally, homogenization is attained [1,15,16].

2.1.1.4. Working conditions

The AISI 316L ASS powders have been ball-milled with a *Fritsch Pulverisette 7* milling apparatus, located at the Universitat Autònoma de Barcelona, using hardened stainless steel vials (20 ml in volume) and balls (3 balls of 1 cm diameter). Note that although some iron contamination arising from the vials and balls can be found, this is expected to be lower than 1 mass % [17].

It should be mentioned that even though hardened stainless steel leads to a more energetic milling than other media, such as agate or zirconia, due to its larger density, a rather small ball-to powder mass ratio has been chosen in the Thesis in order to allow a better control of the microstructural changes with milling time.

2.1.2. Uniaxial compression testing

The response of a material to the application of a mechanical load depends on its mechanical properties. Materials can be subjected to different loading designs, such as compression, torsion or tensile modes, and the resulting properties (e.g., mechanical or magnetic) can depend on these loading conditions.

Typically, in compression testing, a specimen is subjected to a continuously increasing uniaxial compressive load until it fractures. Load (P) and displacement (Δl) are carefully recorded at a certain deformation velocity, previously programmed. The outcome of a compression test is a load-displacement curve, which is commonly converted into a (compressive) stress (σ)-strain (ε) curve as follows:

$$\sigma_{engineering} = \frac{P \cdot g}{A_0} = \frac{F}{A_0} \quad \text{(Eq. 2.2)}$$

and

$$\varepsilon_{engineering} = \frac{|\Delta l|}{l_0} = \frac{|l_0 - l|}{l_0} \text{ (Eq. 2.3),}$$

with A_0 the (initial) cross section area on which the load is applied, l_0 the initial length of the tested specimen and g the acceleration of gravity. Note that in this case, both the compressive stress (σ) and the deformation (ε) are expressed in such a way to represent them on the positive axes. Since these values of tension and deformation are referred to the initial morphology of the samples, this plot is denoted as engineering stress-strain curve [18].

2.1.2.1. Working conditions

Compression tests of either bulk $Fe_{60}Al_{40}$ (at. %) alloys or AISI 316L ASS samples have been performed with the aim to obtain different degrees of mechanical work. Specifically, a load control mode, with a fixed loading rate, is used in order to perform compression functions consisting of a loading segment until a certain target engineering stress, previously programmed, is reached, followed by a load holding segment and, then, by an unloading step executed at the same loading rate in absolute value.

The compression processes have been performed uniaxially, at room temperature, using a *MTS 858 Table Top System Universal/Tensile* apparatus, located at the Universitat Autònoma de Barcelona.

2.2. Irradiation methods

This part introduces some general issues of ion-solid interactions and describes the ion irradiation techniques (i.e., broad beam ion irradiation and focused ion beam) utilized to modify the surface of target materials (i.e., $Fe_{60}Al_{40}$ and ASSs). In addition, the lithography process to produce shadow masks on $Fe_{60}Al_{40}$ sheets by means of an electron beam writer is also presented.

Since all the irradiation processes have been performed perpendicularly to the target surface, this is the irradiation configuration that has been considered to describe the aspects related to ion-solid interactions.

2.2.1. Broad beam ion irradiation

Since it is not the goal of this work to focus on ion-solid interactions, only a brief introduction of the main phenomena which take place in a target material upon irradiation is surveyed. Furthermore, the experimental setups for the diverse broad beam ion irradiations are described.

2.2.1.1. Essentials on ion-solid interactions

The interaction of an energetic ion with a target involves several processes. As an ion penetrates a solid, it slows down by transferring energy to both the atoms and the electrons of the material. Namely, ion kinetic energy and momentum are transferred to the target through both inelastic and elastic interactions. In inelastic interactions, ion energy is lost to the electrons in the sample and results in ionization and the emission of electrons and electromagnetic radiation from the solid. Conversely, ion energy is transferred as translational energy to target atoms in elastic interactions and can result in damage (displacement of sample atoms from their initial sites) and sputtering from the sample surface.

In these interactions, the incident ion loses energy, E, at a rate of $\frac{dE}{ds}$ (also known as stopping power), which is the energy loss by the ion in the target per unit traversed distance, s. Typically, its magnitude ranges from of a few to 100 electron-volts per nanometer, depending on the energy and mass of the ion as well as on the substrate

material (i.e., target). Note that the sign of $\frac{dE}{ds}$ is negative, as it represents the energy loss per increment path. Taking into account this stopping power, a penetration path R can be defined as:

$$R = \int_{E_0}^{0} \frac{1}{\frac{dE}{ds}} dE \quad \text{(Eq. 2.4)},$$

with E_0 the incident energy of the ion. Since the ion does not traverse in a straight path due to collisions with target atoms, the projection of R measured along the vector of the ion's incident trajectory (i.e., normal to the surface), called projected range (R_p), gives the ion's net penetration into the material and, thus, allows quantifying the extent of radiation damage. As a result of the collisions, a lateral range of damage is also defined, which takes into account the horizontal (i.e., parallel to the surface) extent of ions [19-21].

Excluding the effect of the orientation of the crystal lattice with respect to the primary direction of the ion, the main parameters governing the energy-loss rate are the primary energy E_0, the atomic number of the ion (Z_{ion}) and the atomic number of the target substrate (Z_{target}). Since the distance traveled by the ion between collisions and the amount of energy lost per collision are stochastic (random) processes, all ions of a given type and incident energy do not have the same range (i.e., the collision sequence and subsequent ion deflection vary randomly from ion to ion). Essentially, there is a broad distribution in depth for ions of the same species and energy, whose shape can be characterized by its statistical moments. At low ion doses (dose or fluence is the number of ions per unit area, which is usually given in ions per square centimeter) and in the absence of crystal orientation effects, the range and the projected range distributions are roughly Gaussian and, hence, their shape can be approximately described using the first and the second statistical moments. Note that the first moment gives the mean value and the second the variance (the standard deviation of a distribution is the square-root of the

variance). Conversely, at higher doses, upper statistical moments, such as the third one, which gives a measure of the asymmetry of the distribution, are often necessary to describe more accurately ion depth distributions [19].

2.2.1.1.1. Mechanisms of energy loss

It is common to distinguish two different mechanisms of energy loss, one linked to nuclear collisions, in which energy is transmitted as translational motion to a target atom as a whole, and the other to electronic collisions, in which the moving particle (i.e., ion) excites or ejects atomic electrons. Indeed, a proper understanding of the mechanisms of energy loss is important not only to control the depth profile of implanted ions, but also in determining the nature of the lattice disorder. In a good approximation, whereas the electronic mechanism is considered as an inelastic process, the nuclear collisions are thought as an elastic one. Thus, the energy-loss rate $\frac{dE}{ds}$ is approximately composed linearly by nuclear and electronic stopping:

$$\frac{dE}{ds} = \left(\frac{dE}{ds}\right)_{nuclear} + \left(\frac{dE}{ds}\right)_{electronic} \quad \text{(Eq. 2.5).}$$

Nuclear collisions can involve large discrete energy losses and significant angular deflection of the ion's trajectory (see Figure 2.3). This process is able to bring about lattice disorder and, thus, atomic mixing by the displacement of atoms from their positions in the lattice. In contrast, electronic collisions involve much smaller energy losses per collision, insignificant deflection and negligible lattice disorder. Actually, the electronic interactions can be viewed more as continuous viscous drag phenomenon between the injected ion and the sea of electrons surrounding the target nuclei.

The relative influence of the two energy-loss mechanisms changes rapidly with the energy (E) and atomic number of the ion (Z_{ion}). Nuclear stopping predominates for low

E and high Z_{ion}, whereas electronic stopping prevails for high E and low Z_{ion}. For the energy regime normally used in heavy ion implantation (i.e., tens to hundreds of keV), the nuclear contribution to the stopping process usually dominates.

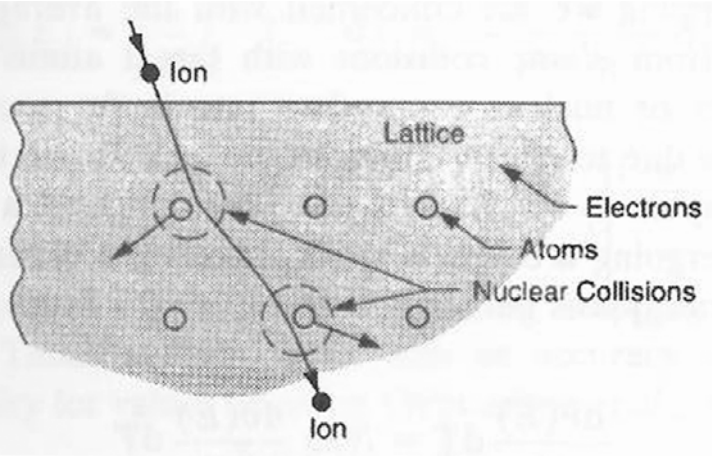

Figure 2.3*. Schematic diagram aimed at showing that the main deflection of an incident ion is owing to nuclear collisions [19].*

2.2.1.1.2. Radiation damage

Since nuclear collisions play a crucial role in the energy transfer to the atoms of the target material, radiation damage can be altered by changing the mass of the irradiating ion; increasing the mass of the ion, increases the amount of energy deposited in nuclear collisions per unit length traveled by the ion and, in principle, the produced atomic damage. Lattice atoms which are displaced by incident ions are called primary knock-on atoms (known also as recoil atoms). If the transferred energy is sufficiently large (the energy required to displace the lattice atom represents the displacement threshold and is called the displacement energy, E_d), these primary recoils will move along a trajectory similar to that of the incident ion, and may again undergo other nuclear collisions, thus creating further generations of recoils and, finally, a collision cascade (see Figure 2.4). Note that ramifications of this process are named subcascades.

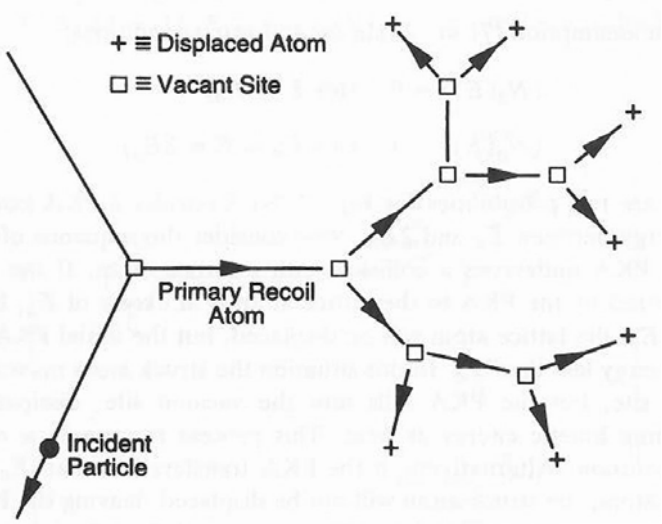

***Figure 2.4**. Schematic representation of the formation of a collision cascade by a primary knock-on atom [19].*

Each individual recoil atom, according to its initial energy, may come to rest at some distance from its original site. The cascade will continue until the energy transfer to the lattice atoms is less than E_d in the collision process. Then, the struck atoms undergo large-amplitude vibrations without leaving their lattice positions and their vibrational energy is quickly shared with nearest neighbors and appears as a localized source of heat. This leads to a distribution of defects in the region around the ion track, such as Frenkel pairs, which are produced when and original atom is displaced, thus leaving a vacancy (an empty lattice site –without an atom– which was originally occupied), and occupies a nearby interstitial position. As the number of incident ions (i.e., fluence or dose) on the crystal increases, the individual disordered regions begin to overlap. Essentially, the total amount of disorder and the distribution in depth depend on ion species, energy, total dose, temperature and channeling effects (which are related to the crystal orientation influence on ion penetration).

Depending on the amount of deposited energy per unit volume (i.e., depending on the mass of irradiating ions), the collision cascade may be more or less dense. Typically, in the case of light ions at high energy (case where the ion penetration range is large compared to the extension of individual subcascades), the complete cascade is split into many subcascades, whereas, in the case of heavy ions at low energy, the extension of

the subscascades may be in the order of the ion penetration range. The density of deposited energy does not only influence the spatial development of the cascade, but also its internal dynamics. Generally, three regimes can be defined: (i) the single collision regime, which is typical for light ions at low energy, where a cascade does not really develop and the atomic motion is stopped after a few collision events; (ii) the linear cascade, which is characterized by the presence of "non-interacting" (i.e., isolated) cascades and (iii) the thermal spike regime, where the cascade becomes especially dense (presence of several interacting subcascades); in the limit, all lattice atoms within the cascade become a thermal ensemble with a high temperature, which may exceed the melting temperature of the solid and even its evaporation temperature on a short time scale (phenomenon usually known as "dynamic annealing"), leading to a noticeable dynamic recovery of the induced structural defects [22]. Namely, there is a recombination process of interstitial atoms with vacancies during evolution of cascades and subcascades. In fact, a certain amount of "dynamic annealing" already takes place in the collisional range, but the probability of dynamic recombination of induced defects increases with increasing cascade density. In this sense, a cascade efficiency parameter ξ (T), which depends on temperature T, is defined, so that the effective number of Frenkel pairs (i.e., the quantity of Frenkel pairs which are not recombined by dynamic annealing, thus which are able to recombine once collision events vanish), N_F^{Eff}, is given by:

$$N_F^{Eff}(T) = \xi(T) \cdot N_F(T) \quad \text{(Eq. 2.6)},$$

with N_F the total number of produced Frenkel pairs. The cascade efficiency is between 1 in the low-density limit (e.g., light ions) and about 0.3 for very dense cascades for heavy ions with large nuclear stopping, which results in less mobile defects [23].

On the other hand, another type of structural recovery has to be taken into account at times long after the cascade lifetime (typically, $t > 10^{-11}$ s). The remaining vacancy-interstitial pairs (i.e., N_F^{Eff}) can contribute to atomic diffusion processes, an effect which

is commonly called radiation enhanced diffusion. Namely, the atomic displacements resulting from energetic recoiling atoms can be highly concentrated into small localized regions containing a large concentration of defects well in excess of the equilibrium value. If the defects are produced at temperatures where they are mobile, and can in part anneal out, the balance between the rate of formation and the rate of annihilation leads to a steady state of excess concentration of defects. Since the atomic diffusivity is proportional to the defect concentration, an excess concentration of defects leads to an enhancement in the diffusional process. It should be noted that atomic motion in most alloys usually takes place by the interchange between atoms and neighboring vacant sites [19].

Moreover, it is known that ordered alloys can become chemically disordered under irradiation. The effects of irradiation on the ordered alloy are described by the competing processes of chemical disordering, which is induced by atomic replacements resulting from displacement and cascade damage, and chemical ordering, which is stimulated by radiation enhanced diffusion. However, when an ordered material is irradiated with heavy ions at low temperature, complete disordering within the cascade volume may result, being the reordering (i.e., structural recovery) process minimized after irradiation due to the low mobility of produced defects [19].

A widespread way to quantify irradiation damage in a single parameter is the so-called "displacements per atom" or dpa. A unit of dpa means that, on average, every atom in the irradiated volume has been displaced once from its equilibrium lattice site [19,20]. Radiation damage quantification is based on the assumption that a lattice atom, struck by an energetic ion or recoiling target atom, must receive a minimum amount of energy in the collision to be displaced from its lattice site. Since the stopping of an ion is a stochastic process, the displacement per atom parameter varies with depth and a statistical distribution is observed.

2.2.1.1.3. Radiation damage estimation by means of ion-solid simulations: the TRIM program

The ion-solid interactions between energetic atoms and targets have been simulated by means of the TRIM (*the TRansport of Ions in Matter*) code, which is a Monte Carlo computer program [24], developed to determine principally ion range and damage distribution in amorphous materials. TRIM uses several physical approximations to obtain high computer efficiency, while still maintaining accuracy. Two significant approximations are (i) using an analytic formula for determining atom-atom collisions, relying on a binary collision model, and (ii) evaluating only the stage of damage which is caused by the permanent displacement of lattice atoms from their original sites by the energy transfer received in nuclear collisions.

In order to run TRIM, the main input parameters which must be previously set are the species of projected ion, its energy and the density of the target material. Then, after averaging over a certain amount of ion histories, the distributions of different ion-related parameters, such as collisional damage, can be obtained.

To treat damage in TRIM computer simulations, the *Detailed Calculation with Full Damage Cascades* option has been used. This approach follows every recoiling atom until its energy drops below the lowest displacement energy of any target atom (i.e., tracking only particles down to energies near the displacement threshold, E_d). In effect, the collisional damage to the target is estimated by employing the hard-sphere model of Kinchin and Pease [25]. Essentially, TRIM allows obtaining the total number of target-atom displacements produced by one incident ion along its track (N_d). Owing to the stochastic nature of ion-solid interactions, N_d also shows a distribution in depth, x.

The dpa at a certain depth x, produced in a target material with atomic density ρ_{at} and after being irradiated using a fluence F, can be quantified by using N_d (x) as:

$$dpa(x) = \frac{N_d(x) \cdot F}{\rho_{at}} \text{ (Eq. 2.7).}$$

Note that it is a dimensionless unit and increases with ion dose. Nevertheless, since no dynamic annealing in collision cascades is taken into account, TRIM can give a rather overestimated value of N_d and, therefore, of dpa(x).

2.2.1.1.4. Radiation sputtering and ion implantation

Other secondary effects accompanying ion irradiation, such as sputtering of target atoms, also depend strongly on the relative importance of nuclear and electronic stopping. Sputtering is the erosion (i.e., physical removal) of the sample by energetic ion bombardment. In this process, surface atoms are removed by collisions between the incoming ions and the atoms in the near-surface layer of a solid. The bombarding ion transfers energy in collisions to target atoms, which recoil with sufficient energy to generate other recoils. Some of these backward recoils will approach the surface with enough energy (energy larger than the surface binding energy) to escape from the solid. It is these secondary recoils which cause most of the sputtering process. This phenomenon is primarily characterized by the sputtering yield, Y, which is defined as follows:

$$Y = \frac{\text{mean number of emitted atoms}}{\text{incident particle}} \text{ (Eq. 2.8).}$$

The sputtering yield depends principally on the structure and composition of the target material, the parameters of the incident ion beam (e.g., primary energy), the ion species

and the experimental geometry [26] and, typically, lies in the range 0.5-20. Note that the TRIM program allows a rough estimation of the sputtering yield once the ion species, its energy and the chemical composition of the target material are set.

Alternatively, the sputtering process can be qualitatively characterized as a length measurement when the physical removal is large enough to be estimated by depth measurements, for instance by topographic imaging. For this, a non-sputtered area is required in order to compare both the non-irradiated and bombarded areas.

In addition, a central effect which goes together with ion irradiation and competes to some extent with sputtering is the implantation process of the projected ions into the surface layer. Namely, there is a depth distribution of the implanted atoms which typically has a maximum at the surface and drops over a distance comparable to the initial ion penetration range. In general, the maximum concentration attainable is given by the reciprocal of the sputtering yield.

Even though there is no precise definition of high-fluence irradiation regime, this is typically considered for doses $\geq 10^{17}$ ions·cm^{-2}. In this range, sputtering can occur noticeably [19] and ion implantation can lead to implanted concentrations of several atomic per cent. Note that, among others, the intrinsic properties of projected ions (e.g., chemical reactivity) have a strong influence on the implantation process.

2.2.1.2. Noble gas ion irradiation

Different noble gas ion species, such as He^+ or Xe^+, have been utilized to irradiate $Fe_{60}Al_{40}$ (at. %) alloys either homogeneously or locally through irradiation shadow masks. A brief explanation of the main components of the employed low-energy ion implanter is initially presented, followed by the working conditions used for the irradiations.

2.2.1.2.1. Ion implanter

A *1090 Danfysik* low-energy (from a few hundred electron-volts to 45 keV) ion implanter has been used for the noble gas ion irradiations. The main components of the implanter are depicted in Figure 2.5. In order to accelerate the ions out of the ion source, an extraction voltage, typically between 20 and 45 kV depending on the ion species, is used while the rest of the system is grounded. This voltage is often combined with a suppression voltage (typically 15 % of the extraction voltage) to neutralize the repelling between the all-positive loaded ions in order to avoid defocusing of the beam. Remarkably, this implanter also has a low-energy feature, where the beam line is put at a potential and only the target chamber is grounded, which allows using low-energy ion irradiation.

For pure gases, the extracted beam current primarily depends on the emitting aperture, extraction voltage and atomic mass. After extracting the ion beam from the ion source, the ions enter the analyzing magnet (mass spectrometer), which is used to sort the ions by mass so that the desired ions are inserted in the target (see Figure 2.5). The heavier the ion, the stronger the magnetic field must be in order to bend the beam to hit the target. Ions with the "wrong" (i.e., no selected) mass are bended too much or too little and are consequently lost on the sidewalls of the magnet tubes. The exit and entrance of the magnet are made with an angle, i.e., slits, where the size and intensity of the beam are limited. The beam is subsequently post-accelerated to the desired voltage and further focused upon the target with an electrostatic quadrupole magnet. Next, the beam passes an electrostatic switch before it enters the sweep system (beam scanning magnets), where the beam is swept over the target. The determination of the dose (fluence) of ions delivered to the target during ion irradiation is carried out by a moveable Faraday cup, which is also swept by the ion beam. For each positive ion that enters the Faraday cup, which is simply a grounded conducting metallic chamber, an electron is drawn through a conducting lead to neutralize the positive charge of the ion.

The fluence F can be also determined by integrating the beam current incident upon the sample by:

$$F = \frac{\int_0^t I dt'}{emA} \quad \text{(Eq. 2.9)},$$

with I the beam current, t the time, m the charge state of the ion, e the electronic charge, and A the area over which the current is monitored.

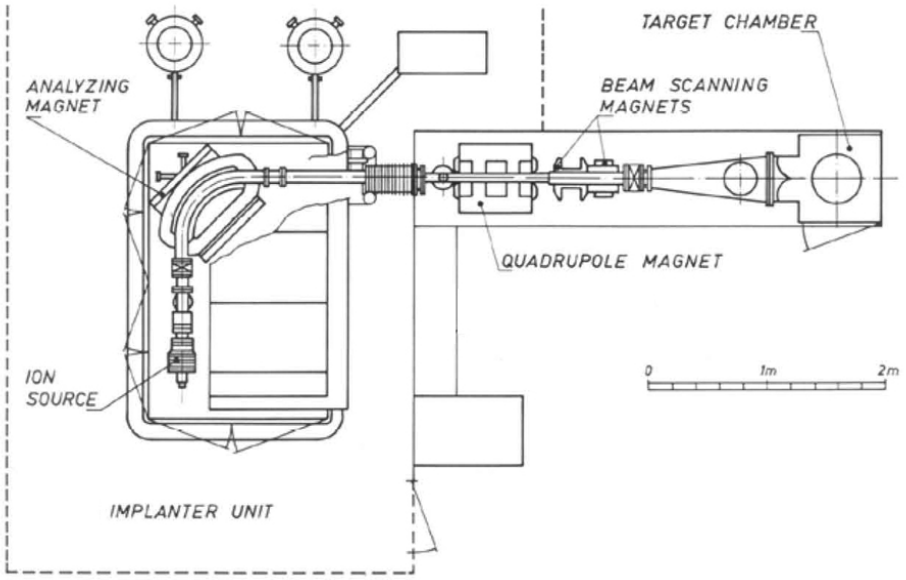

***Figure 2.5**. Schematic picture of the main components of a 1090 Danfysik ion implanter [27].*

The irradiations have been carried out at the Institute of Ion Beam Physics and Materials Research (Forschungszentrum Dresden-Rossendorf, Germany).

2.2.1.2.2. Working conditions

Regarding the homogeneous irradiation approach, the primary energy of the different ions (2 keV He^+, 11 keV Ne^+, 21 keV Ar^+, 35 keV Kr^+, 45 keV Xe^+) is adjusted to

position the maximum of the collisional damage distribution at a depth of around 10 nm (see Figure 2.6) [20,24].

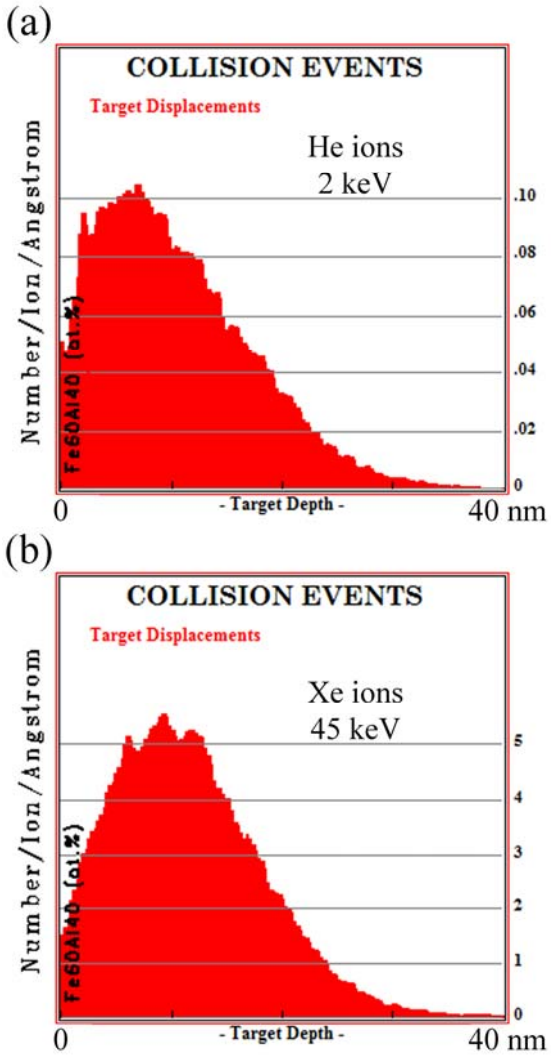

***Figure 2.6**. TRIM simulation of the target depth dependence of collision events (described by the number of target displacements per ion and crossed distance N_d, given in Number/Ion/Angstrom) in $Fe_{60}Al_{40}$ alloys after being irradiated using He^+ accelerated at 2 kV (a) and Xe^+ accelerated at 45 kV (b). Note that most of the physical damage is approximately located within a depth of 30 nm.*

The ion fluence is varied to obtain a damage between 0.05 - 5 dpa. Qualitatively, in order to differentiate between the diverse amounts of induced damage and, thus, characterize the irradiated samples, the dpa values are estimated by taking the 75% of the maximum collisional damage value (i.e., $0.75 \cdot N_d$ (10 nm) for the above conditions) and using Eq. 2.7. For instance, for the 45 keV Xe^+ irradiation at a fluence of $1 \cdot 10^{15}$

ions·cm^{-2}, the dpa estimation is performed using the following values: 0.75·N_d (10 nm) ≈ 4.1·10^8 displacements/(ion·cm) –see Figure 2.6 (b)– and ρ_{at} ≈ 8.2·10^{22} atoms/cm^3, and results in a dpa of around 5.

Moreover, in order to exclude any ion flux effects, which might arise from an interplay of ion bombardment and thermal diffusion, the ion current density is varied from 0.02 μA/cm^2 (for Xe^+) to 2 μA/cm^2 (for He^+) to achieve the same damage rate for all ion species. Note that the larger current density, the higher is the concomitant heating process, which indeed depends on the nature of the ion as well.

Regarding the local ion irradiation processes through shadow masks, the working conditions are specified in chapter 3.

2.2.1.3. Ion beam nitriding

Ion beam nitriding processes (i.e., ion irradiation using nitrogen ions) at normal incidence have been carried out with a broad beam (≈ 7.5 cm in diameter) and a high current density ion implanter, with a Kaufman type ion source (see Figure 2.7). These have been performed in the temperature range of 300-400ºC (note that the sample holder is coupled with a furnace) and under an air pressure of ≈ 10^{-2} Pa, which is low enough to minimize the oxidation during nitriding [28].

The ion energy, determined by the applied acceleration voltage, and the ion current density are ≈ 1 keV and 0.5 mA/cm^2, respectively. Although the leaving ions have an energy of 1 keV (which is the true energy of incident N^+ ions), implanted molecular ions N_2^+ break up, arriving at the sample surface with an effective energy of 0.5 keV. The ratio of the charge species in the ion beam, which depends on the applied discharge voltage between the filament and the anode of the source, is estimated to be 55% N_2^+ and 45% N^+ [29], corresponding to the flux of ≈ 3·10^{15} ions·cm^{-2}·s^{-1}. The processing

times are 5, 7 or 30 minutes, which result in fluences of 9, 13 and $54 \cdot 10^{17}$ ions·cm^{-2}, respectively.

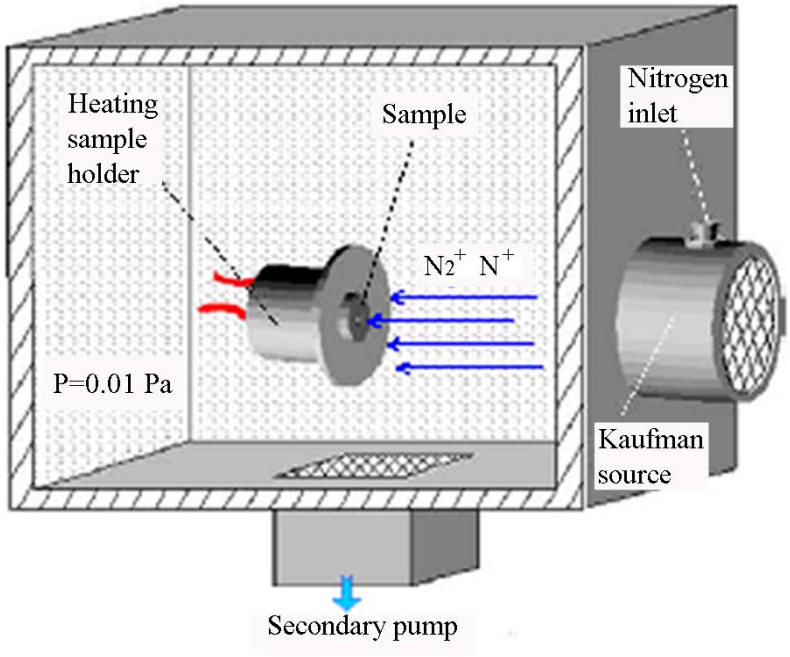

Figure 2.7*. Schematic representation of the implantation device [28].*

The ion energy has been set to allow the ions to overcome the surface barrier (i.e., to sputter-remove native oxide), to be implanted into the surface to form nitrogen enriched layers and to split the molecular ions into nitrogen atoms. The ion flux has been chosen to be high enough in order to implant enough nitrogen concentrations to produce relatively deep nitrided layers [30].

Besides, in order to perform the thermal treatments, the initial temperatures provided by the furnace before nitriding are slightly lower (e.g., 350 ºC for treatments set at 400ºC) due to the current density provides the additional heating that increased the temperature of the samples up to the target value [28].

Note that in contrast with the noble gas ion irradiations, the sputtering process is much more pronounced since the current doses are larger and the irradiations have been performed at high temperature.

The nitriding processes have been carried out at the Institute of Ion Beam Physics and Materials Research (Forschungszentrum Dresden-Rossendorf, Germany) in collaboration with Dr. G. Abrasonis.

2.2.3. Focused ion beam

The focused ion beam (FIB) microscope works in a similar way to a scanning electron microscope (SEM), except that the beam that is scanned over the sample is an ion beam rather than an electron beam. Nevertheless, most modern FIB instruments supplement the FIB column with an additional SEM column, resulting in a versatile dual-beam platform (FIB-SEM, see Figure 2.8).

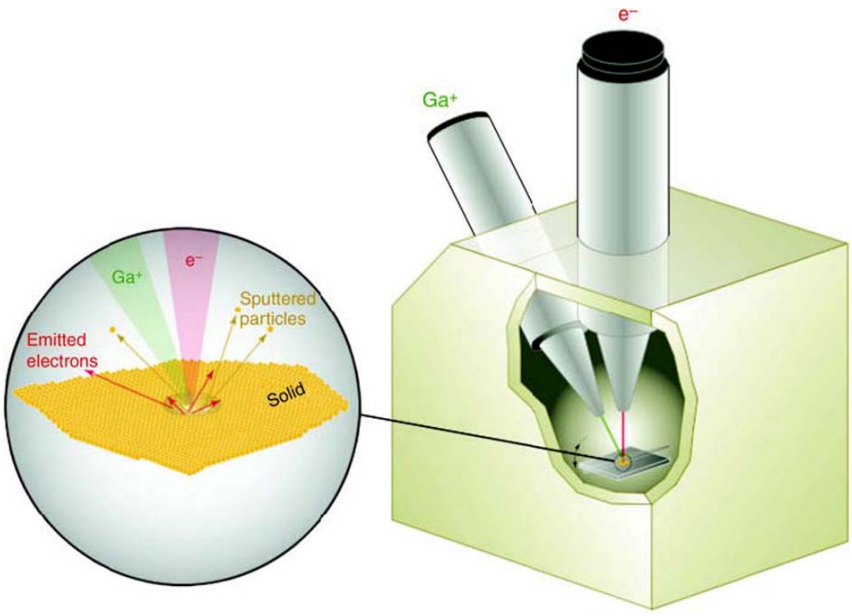

Figure 2.8. *Schematic image of a dual-beam FIB-SEM instrument. The expanded view illustrates electrons and ion beam sample interaction [31].*

The basic functions of the FIB, imaging, irradiating and sputtering with an ion beam, require a highly focused beam [31-33]. High-resolution ion beams are defined by the use of a field ionization source with a small effective source size on the order of 5 nm, therefore enabling the beam to be tightly focused. The ion source is a liquid metal ion source, being Ga the most utilized element due to its combination of properties: a low melting temperature (around 30 ºC), which makes the liquid source easy to operate, low volatility, low vapor pressure and a negligible reactivity with the material defining the needle (typically W), which make the Ga-based sources be highly stable [31].

During operation, Ga ions flow from a reservoir to the needle tip, where they are extracted by field emission. The ion beam column consist of two lenses (a condenser and objective lens) to define the beam and then focus it on the sample, beam-defining apertures to select the beam diameter and current, deflection plates to scan the beam over the sample surface, stigmation poles to ensure a spherical beam profile, and a high-speed beam blanker to quickly deflect the beam off the sample onto a beam stop, such as a Faraday cup. The ion beam is focused and steered using electrostatic components rather than the electromagnetic components used for electrons, since it is impractical to build electromagnetic lenses for ions due to the fact that the focusing strength of an electromagnetic lens is directly related to the charge/mass ratio of a particle.

The size and shape of the beam intensity profile on the sample determines the basic imaging resolution and micromachining precision. The smaller the beam diameter, the better the achievable resolution and milling precision [34]. In general, the beam spot size is limited mostly by the chromatic aberration that results primarily from the energy spread of the beam due to space charge effects at the ion source and secondarily from the spherical aberration of the lenses. However, the ultimate spatial resolution for FIB imaging is, in fact, limited by sputtering and, therefore, it depends on the specimen. In modern FIB systems, the imaging resolution, determined by the sputter-limited signal/ noise, is usually about 10 nm.

The sample is mounted on an electrically grounded stage with three-axis translation, rotation and tilt capabilities.

Finally, note that imaging with Ga ions may result in Ga incorporation near the sample surface, thus modifying the chemical composition of the sample [32].

2.2.3.1. Working conditions

In order to generate periodic arrays of magnetic structures on $Fe_{60}Al_{40}$ (at. %) sheets, areas of 50 × 50 μm^2, containing arrays of circular and rectangular nanostructures, have been prepared by means of a focused ion beam (FIB, *Crossbeam 1540 XB*, *Zeiss*) using Ga^+ accelerated at 30 kV.

The FIB irradiations have been carried out at the IFW (Leibniz-Institut für Festkörper- und Werkstoffforschung) Dresden (Germany) in collaboration with Dr. T. Gemming.

2.2.4. Electron beam lithography

Electron beam lithography (often abbreviated as e-beam lithography, EBL) consists in locally exposing an electron-sensitive resist (i.e., a polymeric film which coats the surface of the material to be lithographed) by a beam of electrons (exposure step) and, then, in selectively removing either exposed (positive resists) or non-exposed regions (negative resists) of the resist (developing stage). The purpose is to fabricate nanostructures in the resist that can be subsequently transferred onto the substrate material [35,36].

Namely, the substrate to be lithographed is first spin-coated with a uniform layer of resist dissolved in an organic liquid solvent. Depending on both the resist viscosity and

the spinning speed, different resist thicknesses can be prepared (typically, the thicknesses range from tens of nanometers to a micron). Afterwards, a soft thermal treatment of the resist is necessary to remove the resist solvent and promote adhesion. Selected areas of the resist, controlled by a computer through a position generator interface, are then usually exposed to the e-beam in a scanning electron microscope. Upon sufficient exposure, the polymer chains in the resist are either broken (positive resist) or become cross-linked (negative resist). By choosing the right developer, temperature and developing time, the programmed structures are obtained. Polymethylmethacrilate (PMMA) and trichlorobenzene are the most utilized positive resist and developer, respectively, in wet etching processes [37].

2.2.4.1. Working conditions

In order to generate periodic arrays of magnetic structures at the top of $Fe_{60}Al_{40}$ (at. %) sheets, shadow masks have been produced by electron beam lithography, generating patterns in both a 90 nm and 70 nm thick PMMA resist layers spin-coated on $Fe_{60}Al_{40}$ sheets. 50×50 μm^2 areas containing different types of nanostructures (circles, squares and rectangles) have been designed on the resist.

The e-beam lithography has been carried out by means of a Leica LION LV1 Electron Beam Writer at the Paul Scherrer Institut (Villigen PSI, Switzerland) in collaboration with Dr. L. Heyderman's group.

2.3. Structural, morphological and mechanical characterization techniques

In this subchapter, the experimental techniques to perform the structural, morphological and mechanical characterization are surveyed.

2.3.1. X-ray diffraction

2.3.1.1. Fundamentals

X-ray wavelengths are comparable with inter-atomic distances in crystals and, therefore, are an excellent probe for this length scale since X-rays can be diffracted [38]. To obtain constructive interference in X-ray diffraction (XRD) experiments, the phase shift should be proportional to 2π or that the difference in the length of the path for rays reflected from successive planes should be equal to an integer number of wavelengths, as illustrated in Figure 2.9.

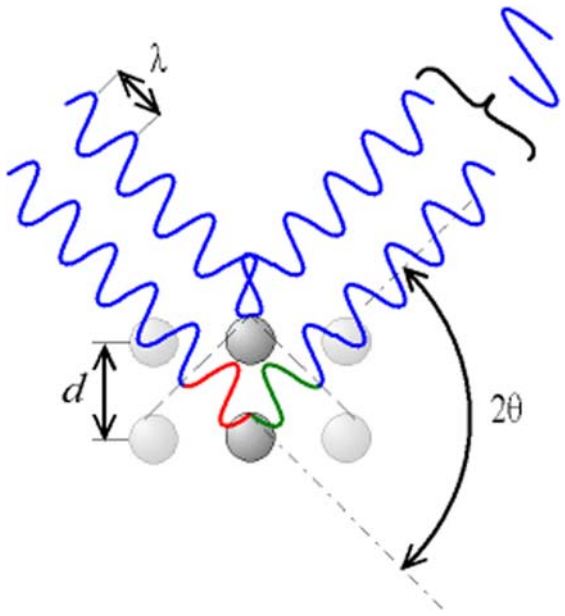

Figure 2.9. *Schematic representation of the conditions for constructive interference, resulting in Bragg's law.*

Hence, a maximum diffracted intensity of the crystallographic planes corresponding to the interplanar distance d will appear in the diffraction pattern. If, for a certain

wavelength λ of the X-ray radiation and a certain incident angle θ, Bragg's law is obeyed, which is given by:

$$n\lambda = 2d\sin\theta \quad \text{(Eq. 2.10)},$$

where the integer n, which gives the number of wavelengths in the difference in path for waves coming from successive planes, is the order of reflection [1-3].

The Bragg's law assumes the crystal is ideal (without structural defects) and the incident beam is perfectly monochromatic and collimated. These conditions are however never fulfilled completely. Usually, crystalline materials are found to be composed of several grains, with different orientation and with certain amount of defects. Each of these grains is called a crystallite. Small crystallite sizes and presence of microstrains among others lead to a broadening of the X-ray diffraction peaks. Namely, the size of these crystallites and the microstrains present in them can also be obtained from the XRD pattern, since both effects contribute to the width of the diffraction peaks [39,40]. The most frequent procedure to evaluate these effects is to consider that the peaks can be fitted using a pseudo-Voigt function, which is a linear combination of a Gaussian and a Lorentzian (or Cauchy) profile [41,42]. Using this formalism, the crystallite size (<D>) can be deduced from the Cauchy contribution to the integral width of the diffraction peak, β_C, as follows:

$$< D >= K\frac{\lambda}{\beta_C \cos\theta} \quad \text{(Eq. 2.11)},$$

with θ the angular position of the peak, λ the wavelength and K a constant which depends on crystallite shape [39], but generally is close to unity. The value of <D> represents the coherent diffraction domain. This equation is commonly known as the

Scherrer formula [39]. Analogously, microstrains can be determined from the Gaussian contribution to the integral peak width, β_G, using the expression:

$$\text{microstrains} =< e >= \frac{\beta_G}{4\tan\theta} \quad \text{(Eq. 2.12)},$$

where <e> stands for the upper limit of microstrains. However, it is more frequent to use the root-mean-square of microstrains, $<\varepsilon^2>^{1/2}$ (rms strain), which is related to <e> in the following way: $<e> = 1.25 <\varepsilon^2>^{1/2}$ [39].

When a specimen, composed of several phases, is analyzed by XRD, each phase originates its own diffraction pattern. The relative intensity of the several peaks in the pattern depends on the relative concentration of the different phases and the phase identification can be carried out by comparison using a proper database [43].

2.3.1.2. Modes of structure analysis

2.3.1.2.1. Bragg diffractometer

This method is often used for phase-identification and uses highly monochromatic X-rays. The sample, placed in the center of a flat goniometer, rotates with an angular velocity of $\theta/\Delta t$. The X-ray detector moves around the circumference of the goniometer with an angular velocity of $2\theta/\Delta t$ and counts the number of photons per second. Since the detector has to follow the diffracted radiation, when the sample rotates θ, the detector has to rotate 2θ, since the diffracted beam is deviated 2θ with respect to the incident beam. As a consequence, this Bragg-Brentano geometry is also known as "θ-2θ" scanning. After diffracting and before entering the detector, the diffracted X-rays pass through a slit in order to keep the X-rays diffracted by the sample collimated. The

width of this slit determines the maximum intensity in the detector. These different parts of the Bragg diffractometer are illustrated in Figure 2.10.

Note that diffraction of a crystallographic plane (hkl) will only occur when this plane is parallel to the sample surface. Hence, crystallographic texture will have a very strong influence on the intensities of the pattern.

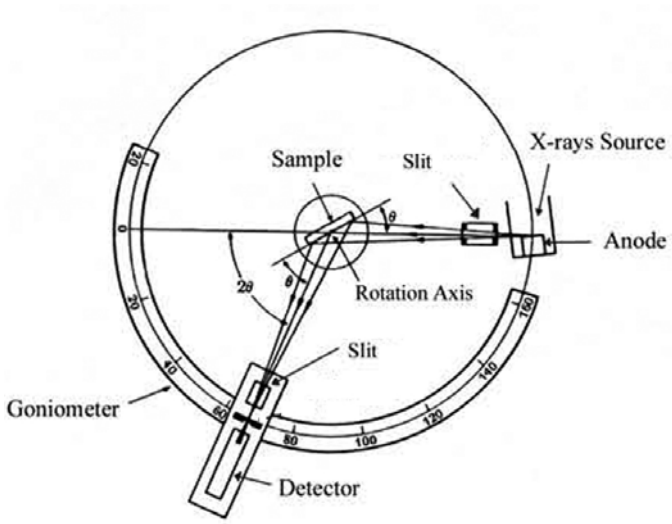

***Figure 2.10**. Schematic picture of an X-ray diffractometer in Bragg-Brentano configuration [39].*

2.3.1.2.2. Glancing incidence

In glancing (or grazing) incidence X-ray diffraction (GIXRD), the incident beam is fixed at very low angles (e.g., 1º) to restrict the material volume contributing to diffraction signal. Typically, only the first hundreds of nanometers are characterized, whereas, in conventional XRD, several micrometers are usually analyzed. Interestingly, this method allows assessing changes in structural properties along depth by measurements at different angles of the incident beam (i.e., depth profiles of a certain parameter can be obtained).

Note that, in this case, the sample remains fixed (at a certain angle of the incoming radiation) and the 2θ scans are obtained by the movement of the detector. Regarding the X-ray generation and beam collimation, a similar scheme as in Bragg-Brentano configuration is followed [44].

2.3.1.3. X-ray penetration depth

The X-ray penetration depth, d_p, can be roughly estimated by means of X-ray absorption from a homogeneous substance. Experiment shows that the fractional decrease in the intensity, I, of an X-ray beam as it passes through any homogeneous substance is proportional to the distance traversed, s. In differential form:

$$-\frac{dI}{I} = \mu ds \quad \text{(Eq. 2.13)},$$

where the proportionality constant μ is called the linear absorption coefficient and is dependent on the substance considered, its density, and the wavelength of the X-rays. Integration of Eq. 2.13 gives:

$$I_s = I_0 \exp(-\mu s) \quad \text{(Eq. 2.14)},$$

with I_0 the intensity of incident X-ray beam and I_s the intensity of transmitted beam after passing through a distance s.

The linear absorption coefficient μ is proportional to the density ρ, which means that the quantity μ/ρ is a constant of the material and independent of its physical state. This later quantity, called the mass absorption coefficient, is the one usually tabulated. Eq. 2.14 may then be rewritten in a more usable form:

$$I_s = I_0 \exp\left[-\left(\frac{\mu}{x}\right)\rho s\right] \text{ (Eq. 2.15).}$$

The mass absorption coefficient of a substance containing more than one element is the weighted average of the mass absorption coefficients of its constituent elements. If ω_1, ω_2, etc. are the weight fractions of elements 1, 2, etc., in the substance and $(\mu/\rho)_1$, $(\mu/\rho)_2$, etc., their mass absorption coefficients, then the mass absorption coefficient of the substance is given by:

$$\frac{\mu}{\rho} = \omega_1\left(\frac{\mu}{\rho}\right)_1 + \omega_2\left(\frac{\mu}{\rho}\right)_2 + \ldots \text{ (Eq. 2.16) [39].}$$

The penetration depth d_p is taken when the intensity of the transmitted beam is 1 % of the intensity of the incident beam (i.e., $\frac{I_s}{I_0} = 0.01$). Therefore, taking into account the above considerations, the penetration depth can be estimated geometrically using the optical path of the X-ray beam (see Figure 2.11) as:

$$d_p = L \cdot \sin\theta = -\frac{\ln(0.01)}{2\left(\frac{\mu}{\rho}\right)\rho}\sin\theta \text{ (Eq. 2.17),}$$

with θ the incident angle of the X-ray beam. Note that the penetration depth depends on the Bragg's angle, θ.

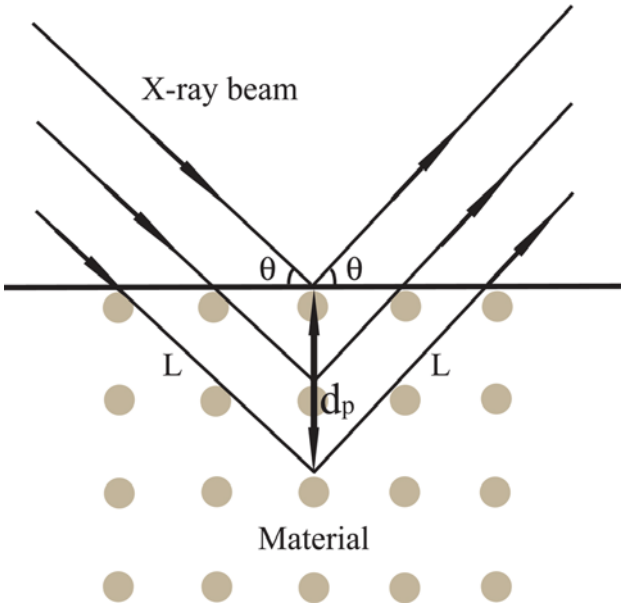

***Figure 2.11**. Geometrical reasoning for penetration depth estimation.*

2.3.1.4. The long-range order parameter

Systems that exhibit order-disorder transitions, such as $Fe_{60}Al_{40}$ (at. %) alloys, may exist in intermediate states where the degree of ordering is not complete. In an atomically ordered state (B2-phase), these alloys consist in a BCC structure with one of the atoms (for instance, Al atoms) located at the center of the lattice with atomic coordinates, referred to the lattice spacing, of (0.5,0.5,0.5) and the other type of atoms (i.e., Fe) at the corners with coordinates (0,0,0). Nevertheless, note that 10 % of Fe atoms must remain in Al sites to preserve the stoichiometry of the alloy. Conversely, when these alloys are atomically disordered (i.e., intermixed), leading to the so-called A2-phase, the above atom positions may be exchanged, thus Al atoms might occupy Fe positions or vice versa. Hence, it is useful to describe these possible structural configurations, and thus the different degrees of ordering, using the following parameters:

- $\mathbf{r_{Fe}}$: fraction of Fe lattice sites occupied by "correct" atoms (i.e., Fe atoms); this type of iron atoms are denoted as Fe_1 and occupies the (0,0,0) sites.

- $\mathbf{r_{Al}}$: fraction of Al lattice sites occupied by "correct" atoms (i.e., Al atoms); these atoms are denoted as Al_1 and occupy the (0.5,0.5,0.5) positions.
- $\mathbf{w_{Fe}}$: anti-site probability of Fe atoms at the Al sites; fraction of Al lattice sites occupied by "wrong" atoms (i.e., Fe atoms); Fe atoms located at (0.5,0.5,0.5) are denoted as Fe_2.
- $\mathbf{w_{Al}}$: anti-site probability of Al atoms at the Fe sites; fraction of Fe lattice sites occupied by "wrong" atoms (i.e., Al atoms); Al atoms located at (0,0,0) positions, which are denoted as Al_2.

The above parameters can be quantified by means of the site occupancy factors, O, of the different atoms, which can be obtained by fitting the XRD patterns. Actually, the above parameters correspond to the site occupancy factors of Fe_1, Al_1, Fe_2 and Al_2, respectively. Since BCC structures have two atoms per cell and (0,0,0) and (0.5,0.5,0.5) atomic coordinates are enough to generate a BCC structure, the above parameters (i.e., occupancies) can be related.

According to the stoichiometry of the alloy,

$$OAl_1 + OAl_2 = 0.8 \text{ (Eq. 2.18)}$$

$$OFe_1 + OFe_2 = 1.2 \text{ (Eq. 2.19).}$$

Moreover, at (0,0,0) positions, it is accomplished:

$$OFe_1 + OAl_2 = 1 \text{ (Eq. 2.20).}$$

Then, combining Equations 2.19 and 2.20, OFe_2 can be also written as a function of OAl_2 ($OFe_2 = 0.2 + OAl_2$ (Eq. 2.21)). Therefore, there is only one independent site occupancy factor.

The degree of ordering can be characterized by means of the so-called long-range order parameter (LRO), defined as:

$$S = \frac{x_{Fe} - w_{Fe}}{y_{Fe}} \text{ (Eq. 2.22),}$$

with x_{Fe} the atomic concentration of iron ($Fe_{60}Al_{40}$ (at. %) $\Rightarrow x_{Fe}=0.6$), w_{Fe} the anti-site probability of Fe atoms at the Al sites (=site occupancy factor of Fe_2, obtained by fitting the XRD pattern) and y_{Fe} is the iron site probability (for a B2 structure, it is equal to 0.5) [45].

In the $Fe_{60}Al_{40}$ (at. %) case, for a completely ordered alloy, $S \rightarrow 0.8$, and, for a completely disordered one, $S \rightarrow 0$. Essentially, the degree of ordering is within $0 < S < 0.8$ [45,46]. In summary, as the atomic disordering increases, the occupancy of atom Fe_2 increases and, therefore, the long-range order parameter decreases.

2.3.1.5. The Rietveld refinement using the MAUD program

The overall microstructural parameters, such as lattice cell parameters (*a*), crystallite sizes (<D>, average coherently diffracting domain sizes), microstrains ($<\varepsilon^2>^{1/2}$, atomic level deformations) and anti-site probabilities of Fe atoms at the Al positions (w_{Fe}, i.e. fraction of Al lattice sites occupied by Fe atoms) have been evaluated by fitting the full X-ray diffraction patterns (i.e., X-ray line profile analysis) by means of the Rietveld refinement program MAUD (*Materials Analysis Using Diffraction*). Essentially, the Rietveld method uses a least squares approach to refine a theoretical line profile until it matches the measured pattern [47].

MAUD fits the XRD profiles deconvoluting the "pure" material profile from the instrumental broadening [47]. A well crystallized Si standard (i.e., a crystal with sufficiently large crystallites and very low defects concentration leading to near zero microstrains, thus assumed to have no size and strain broadening) has been used as the reference sample to correct for the instrumental broadening. Specifically, the MAUD program fits the diffraction XRD patterns by describing the peaks using pseudo-Voigt

analytical functions having both Lorentzian and Cauchy components [41,42]. For deconvoluting size and strain contributions to line broadening, once the instrumental broadening is extracted, MAUD uses a Williamson-Hall like formalism [48]. From the integral width of each of the components (Cauchy and Gaussian) corresponding to the "pure" profile, the crystallite size and the microstrains are obtained respectively.

Interestingly, MAUD also includes the Warren's formalism to quantitatively evaluate stacking fault (SF) probabilities from anomalous peak broadening and the relative variations in intensity of some of the XRD peaks [49], thus allowing an accurate assessment of these planar defects, which are particularly important in the case of ASSs, since they are low-energy stacking fault alloys [50]. According to Warren's description of stacking faults, two types of these planar defects can be distinguished, deformation and twin faults, whose probabilities are denoted as α and β, respectively. Specifically, $1/\alpha$ and $1/\beta$ designate the average number of layers between two consecutive deformation and twin faults, respectively [49].

2.3.1.6. Working conditions

The X-ray diffraction patterns have been recorded by means of a *Philips X'Pert* diffractometer in Bragg-Brentano geometry using Cu K_α radiation (note that both wavelengths $\lambda(K_{\alpha1})$= 1.5406 Å and $\lambda(K_{\alpha2})$= 1.5444 Å have been used in a intensity proportion of $I(K_{\alpha2})/I(K_{\alpha1})$=0.5). The experiments have been carried out at the Servei de Difracció of the Universitat Autònoma de Barcelona.

On the other hand, glancing incidence X-ray diffraction experiments were performed using a *Siemens D5005* diffractometer with the Cu $K_{\alpha1}$ (λ=0.15406 nm) radiation with a fixed incident angle of 1º. The experiments have been carried out at the Institute of Ion Beam Physics and Materials Research (Forschungszentrum Dresden-Rossendorf, Germany).

All diffraction patterns have been recorded using a step-scan mode. This means that the sample and/or the detector rotate in steps instead of in a continuous way. The step size (between 0.02 - 0.06º) and the dwell time (between 5 - 10 s) at each step have been selected in order to have well-defined XRD peaks with a sufficient signal-to-noise ratio to properly fit the patterns.

2.3.1.6.1. X-ray penetration depth in $Fe_{60}Al_{40}$ (at. %) alloys

The mass absorption coefficients of Fe and Al (for Cu K_α radiation) are 308.0 and 48.7 cm^2/g, respectively. Therefore, the mass absorption coefficient of the alloy, (μ/ρ) [$Fe_{60}Al_{40}$ (at. %)], is about 244.8 cm^2/g. Taking into account the atomic masses of Fe and Al (55.85 and 26.98 amu, respectively), the density of the $Fe_{60}Al_{40}$ (at. %) alloy is estimated to be around 5.4 g/cm^3.

Since the X-ray penetration, d_p, depends on the Bragg's angle θ in conventional XRD, d_p has been estimated for 20, 40 and 60º angles, which correspond to the minimum, middle and maximum angles of the employed 2θ scan values (40-120º) to characterize the pressed samples:

$$\theta = 20º \rightarrow d_p \approx 6\ \mu m$$

$$\theta = 40º \rightarrow d_p \approx 11\ \mu m$$

$$\theta = 60º \rightarrow d_p \approx 15\ \mu m.$$

In contrast, for GIXRD measurements at an angle of incidence of 1º, the penetration depth evaluated using the above formalism is ≈ 300 nm. Remarkably, the penetration of X-rays is roughly two orders of magnitude larger in XRD than in GIXRD.

2.3.1.6.2. X-ray penetration depth in AISI 316L ASS

The AISI 316L austenitic stainless steel is essentially a Fe-Cr-Ni alloy (see appendix). The overall mass absorption coefficient (for Cu K_α radiation) of this alloy, (μ/ρ) [AISI 316L ASS], is about 262.1 cm^2/g and its density around 7.95 g/cm^3.

In order to estimate the X-ray penetration depth, the minimum, middle and maximum angles of the used 2θ scan (40-100º) values to record the XRD patterns of the compressed and ball-milled samples have been used:

$$\theta = 20º \rightarrow d_p \approx 4\ \mu m$$

$$\theta = 35º \rightarrow d_p \approx 6\ \mu m$$

$$\theta = 50º \rightarrow d_p \approx 9\ \mu m.$$

2.3.2. Nuclear reaction analysis

Nuclear reactions analysis (NRA) has been used to quantitatively determine nitrogen depth profiles in AISI 304L ASSs samples upon being ion beam nitrided.

Qualitatively, the working principle of this technique relies on the induction of atomic nuclear reactions in a target material (i.e., AISI 304L ASS) by means of an energetic ion beam (e.g., deuteron ions, d^+, with $E \approx 1$ MeV) and the subsequent analysis of the reaction products. In the used energy range, when the incoming ions penetrate the target material, an energy loss process occurs mainly due to the interaction of the beam with atomic electrons (electronic stopping). Since the energy of the reaction products is a function of the energy of incoming ions, it is possible in this way to calculate from the energy distribution of the reaction products the depth distribution of the atoms that react with the impinging ions.

Namely, N depth profiles have been determined by using the $^{14}N(d^{+},\alpha)^{12}C$ nuclear reaction between deuteron ions and nitrogen atoms. From the energy of the emitted α ($^{4}_{2}He^{2+}$) particles, which as mentioned depends on the depth where the deuterium atom reacts in the sample, the nitrogen depth distribution can be quantified.

The employed energy of the deuteron ion beam was 1.4 MeV. In steel, the reaction cross section is constant in the energy range 1.4 down to 1.05 MeV corresponding to an analyzed depth of around 2.5 μm, thus allowing determination of quantitative nitrogen depth profiles until 2.5 μm and qualitative profiles for thicker nitrided layers. Since the nominal energy resolution of the detector is about 15 keV, the depth resolution of NRA technique is around 150 nm near the surface.

In order to obtain the nitrogen depth distribution (given in at. %), the NRA spectra has been fitted using the software *IBA Data Furnace WinDf version 6.5.39 Alpha* [28].

The experiments have been carried out at the Institute of Ion Beam Physics and Materials Research (Forschungszentrum Dresden-Rossendorf, Germany).

2.3.3. Scanning electron microscopy

The working principle of a scanning electron microscope (SEM) is based on the utilization of an electron beam to scan the surface of a material. From the interaction products between the electron beam and the sample, information about the topography or composition can be obtained upon collection of either emitted electrons and radiation of the sample or primary electrons which have already interacted with the target material [51].

2.3.3.1. Interaction between the electron beam and the sample

Due to the consecutive interactions of incident electrons with both nuclei and electrons of the atoms of the sample, an interaction volume (see Figure 2.12) is defined.

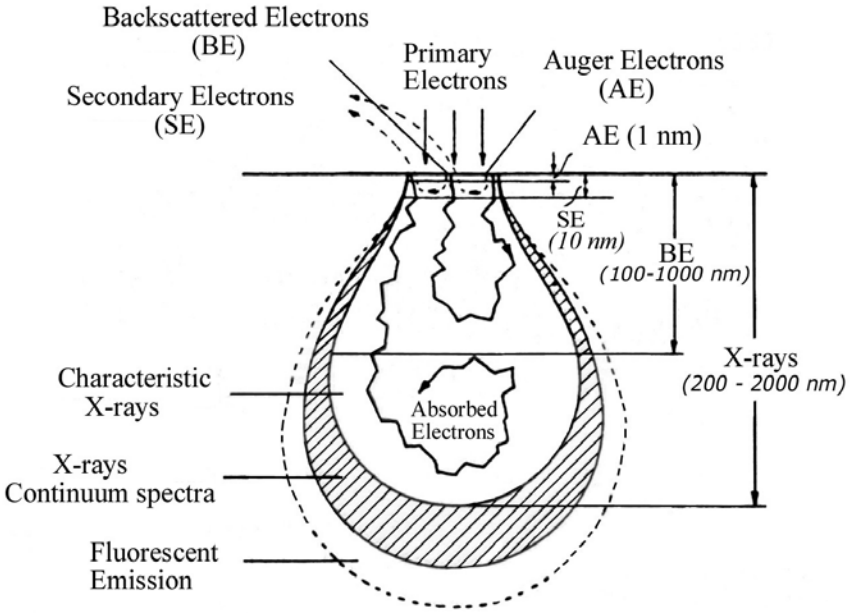

Figure 2.12. *Types of electrons and radiation generated after the interaction between the primary beam and the sample.*

When an electron beam penetrates into the sample, part of these primary electrons will immediately be reflected back without any significant loss of energy (< 1 eV), and only a change in direction occurs due to the interaction with the atomic nuclei of the sample. These electrons are called backscattered electrons and are a form of elastic incoherent scattering. These backscattered electrons have a typical energy between 15 and 30 keV, depending on the primary beam energy. Electrons with lower energies are likely to be absorbed. Since heavier elements backscatter more, information on composition can be obtained from this signal; elements with a higher atomic number will be seen brighter on the resulting image. Furthermore, these backscattered electrons can also provide information about topographical aspects of the surface, because the intensity of this signal depends on the angle between the primary beam and the surface. The electrons

that are not backscattered immediately will lose their kinetic energy by interaction with the electrons of the atoms of the sample [52].

A primary electron with sufficiently high energy can react with one of the core electrons of the atoms of the sample, providing the electron with sufficient energy to leave its shell, with a kinetic energy expressed by $\Delta E_{secondary} = E_{primary} - E_{binding,X}$, with $E_{primary}$ the energy of the incident electron beam and $E_{binding,X}$ the binding energy of the electron at a core shell X. If its kinetic energy $\Delta E_{secondary}$ is high enough, this type of electrons (named secondary) can escape from the sample. However, typical values for the energy of secondary electrons is in the order of 0-50 eV, therefore only the secondary electrons created in the surface layer can escape from the sample and thus information is limited to come from a maximum depth of around 10 nm, while the signal of backscattered electrons usually comes from a depth up to 1 μm, as shown in Figure 2.12. Due to this inner-shell ionization, the atom finds itself in a highly unstable state and, therefore, the corresponding "hole" is immediately occupied by a third electron, located in a more external electronic shell with lower binding energy. During this relaxation process, an amount of energy is liberated, which can be expressed as $\Delta E_{binding} = E_{binding,X} - E_{binding,Y}$,

whit $E_{bind,X}$ and $E_{bind,Y}$ the respective binding energies of the electron of the more inner shell X where the hole was created and the binding energy of the electron at a more outer shell Y that will refill shell X. This "refilling" process must obey some quantum mechanical rules [52]. The energy released can be used to emit another electron from one of the outer shells, called an Auger electron, or can be emitted directly under the form of X-rays, both carrying information (energies) characteristic for the atom where they were generated, and thus providing information about the composition of the sample. The probability of emitting an X-ray (instead of an Auger electron) is represented by the fluorescence yield, which shows that this fluorescence is a strong function of the atomic number. While the emission of Auger electrons results mainly from elements with a low atomic number, X-ray emission is more efficient for higher mass elements [52-54].

Finally, it should be mentioned that the different types of radiation emerging from the sample (X-rays, secondary electrons, backscattered electrons, etc.) are collected by adequate detectors located within the SEM column.

2.3.3.2. Working conditions

The SEM observations corresponding to the arrays of structures prepared by FIB have been performed using the SEM column of the FIB apparatus (FIB, *Crossbeam 1540 XB*, *Zeiss*) at the IFW Dresden (Germany). On the other hand, the morphology characterization of the ball-milled AISI 316L ASS powders has been carried out by means of a *JEOL JSM 6300* microscope at the Servei de Microscòpia of the Universitat Autònoma de Barcelona. In both cases, the images have been taken using secondary electrons.

2.3.4. Atomic force microscopy

In atomic force microscopy (AFM), a probe consisting of a sharp tip arranged near the end of a cantilever is scanned across a sample surface (see Figure 2.13), using a piezoelectric positioning device, at distances where the tip-sample atomic interactions (for instance, due to van der Waals or chemical bonding forces) are significant. Note that the sample remains stationary in this configuration, even though other arrangements maintain the tip immobile while the sample holder is in motion [55].

Qualitatively, while keeping the tip-sample interaction constant upon scanning, the topography of the sample can be assessed by measuring the vertical deflection of the cantilever. To achieve this, most atomic force microscopes use a laser beam which is reflected from the backside of the cantilever, often coated by a thin metal layer to increase reflectivity, onto a position-sensitive photodetector consisting of two side-by-side photodiodes (see Figure 2.13). In this arrangement, a small deflection of the

cantilever will tilt the reflected beam and change the position of the beam on the detector. The difference between the two photodiode signals indicates the position of the laser spot on the detector and, hence, the angular deflection of the cantilever [55].

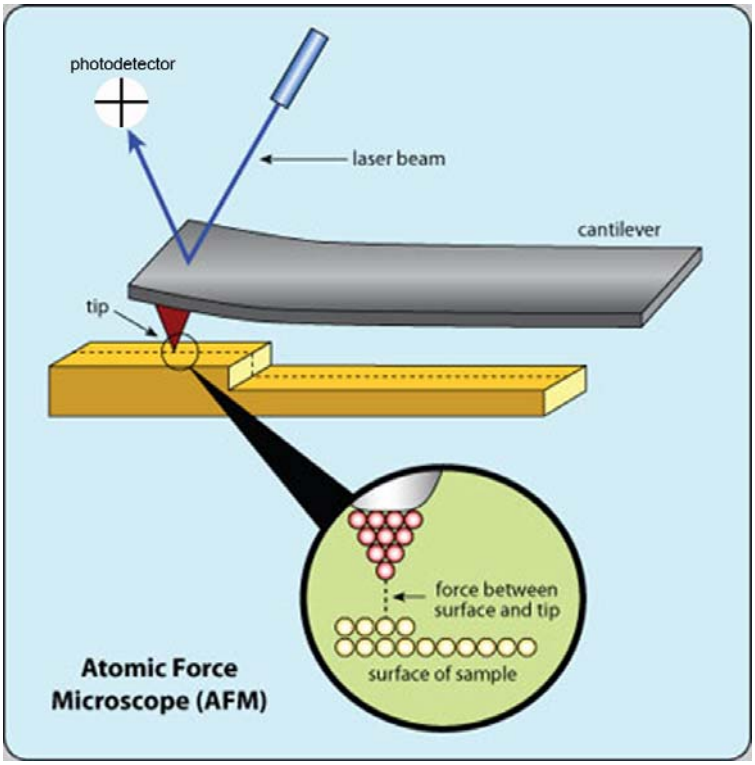

***Figure 2.13**. Schematic illustration of the working principle of an atomic force microscope. A sharp tip is scanned over the surface of the assessed material [56].*

In general, imaging types are divided into static (also called contact) and dynamic modes, where the non-contact and the intermittent contact modes (usually known as *TappingMode*, name registered by *Veeco Instruments* [57]) are distinguished.

In contact mode, the probe is essentially dragged across the sample surface, leading to a repulsive overall force. During scanning, a constant bend in the cantilever is maintained, which constitutes the feedback signal. As the topography of the sample changes, the piezoelectric device moves the relative position of the tip with respect to the sample to keep the set deflection of the cantilever. Using this feedback mechanism, the topography of the sample is thus mapped during scanning since the motion of the

piezoelectric scanner corresponds directly to the sample topography. Regrettably, when the combination of the applied forces and the contact areas involved results in high contact stresses, tips can be extremely damaged. Therefore, dynamic modes are preferred since at least the contact between the tip and the surface is minimized.

To reduce or eliminate the damaging forces associated with contact mode, the cantilever can be oscillated near its first bending mode resonance frequency (normally on the order of 100 kHz) as the probe is scanned above the surface in either non-contact mode or intermittent contact mode (i.e., *TappingMode*). In non-contact dynamic mode, the cantilever is externally oscillated at or close to its resonance frequency. The oscillation amplitude, phase and resonance frequency are modified by tip-sample interaction forces. In effect, these changes in oscillation with respect to the external reference provide the feedback signal and therefore information about the sample. Schemes for dynamic mode operation include primarily frequency modulation and the more common amplitude modulation. In frequency modulation, changes in the oscillation frequency provide the information about tip-sample interactions. In amplitude modulation, changes in the oscillation amplitude or phase provide the feedback signal for imaging. Since in ambient conditions, most samples develop a liquid meniscus layer due to the atmospheric humidity, keeping the probe tip close enough to maintain short-range forces detectable, but without touching the sample, presents a major impediment for the non-contact dynamic mode in ambient conditions [55].

Nevertheless, to circumvent this, the so-called intermittent dynamic regime is utilized. In *TappingMode*, the cantilever is driven to oscillate up and down at near its resonance frequency by a small piezoelectric element mounted in the AFM tip holder. The amplitude of this oscillation is greater than in the non-contact regime. Due to the interaction of forces acting on the cantilever when the tip comes close to the surface, the amplitude of this oscillation tends to decrease as the tip gets closer to the sample. Therefore, preserving this amplitude allows assessing the sample surface. A constant amplitude is maintained through a feedback loop with the scanner and, in contact mode, the motion of the scanner is used to generate the topographic image. Furthermore, by

using the changes in phase angle of the cantilever probe, a second image, called a phase image or phase contrast image, can be obtained. This image has been shown to be sensitive to material surface properties, such as mechanical or chemical composition [57].

Specific details of the apparatus used to record the AFM images are presented in section 2.4.3.

2.3.5. Vickers macro/microindentation

2.3.5.1. Fundamentals

Indentation testing is a simple method that consists essentially of touching the material of interest, whose mechanical properties, such as elastic modulus and hardness, are unknown, with another material whose properties are known. In a typical indentation test, whether on the macroscopic, microscopic or nanometric scale, load (P) is applied to an indenter that is in contact with the surface of a specimen. Hardness can be qualitatively defined as the resistance of a material to be penetrated by an indenter.

In any indentation experiment, evaluation of hardness, H, is carried out by dividing the applied force, F (perpendicular to the specimen surface), by the contact area, A, between the indenter and the sample surface. However, different shapes can be used for the indenter and, if A is taken as the curved surface area under the indenter, the shape of the indenter will clearly have a strong impact on the hardness values obtained [58,59]. Therefore, a more physical meaning is assigned to H when A is taken as the projection of the area of contact, A_p, between the indenter and the surface onto the specimen surface. This definition has become known as Meyer hardness [60], the physical meaning of which is the mean pressure over the surface of the indentation, if the friction between the surface of the indenter and the sample can be neglected. In conventional macro/microhardness tests, the projected contact area is calculated after unloading from

the residual impression left in the surface of the assessed specimen by optical measurements.

In particular, the Vickers hardness (H_V) test has been formally known as the *diamond pyramid hardness* test. The Vickers hardness can roughly be divided in two distinct load ranges of working conditions, i.e., micro –from 10 g to 1000 g– and macro –from 1 kg to 100 kg–. For nomenclature purposes, the load in kg is often specified together with the symbol H_V. For instance, $H_{V0.1}$ is employed to give the Vickers hardness value when the test has been carried out using a load of 0.1 kg. With the exception of test loads below around 200 g, Vickers values are generally considered test force independent, although it is known that hardness values increase slightly when applied force decreases. In other words, if the material tested is uniform, the Vickers values will be the same if tested using loads larger than 200 g. But, below this "threshold" value, caution must be used when trying to compare results.

The Vickers hardness test method consists of indenting the test material with a diamond indenter, in the form of a right pyramid with a square base and an angle ψ of 136 degrees between opposite faces, subjected to a certain load. The two diagonals of the indentation left in the surface of the material after removal of the load are measured using an optical microscope and their average calculated (see Figure 2.14). The Vickers hardness is defined as:

$$H_V = \frac{P \cdot g \cdot \sin\left(\frac{\Psi}{2}\right)}{2 \cdot a^2} \quad \text{(Eq. 2.23)},$$

with P the full load, g the acceleration gravity, Ψ the tip angle and a the mean semi-diagonal of the indentation [61].

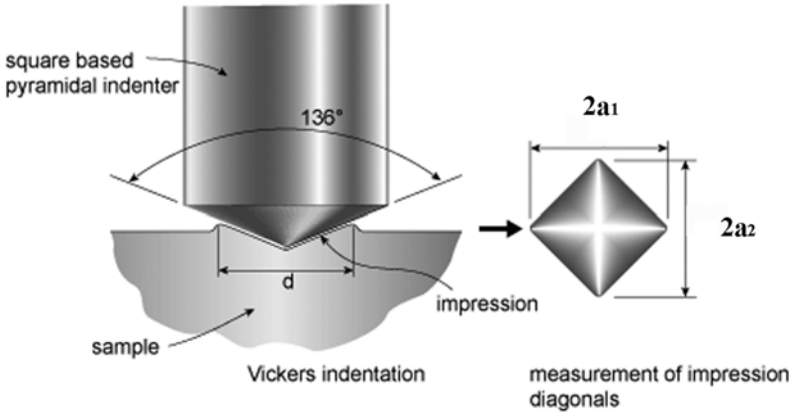

Figure 2.14*. Schematic picture of a Vickers indentation.*

2.3.5.2. Working conditions

Microhardness measurements have been performed according to the rules of ISO 6507-1 standard [61].

The microhardness corresponding to the compressed samples of $Fe_{60}Al_{40}$ and AISI 316L ASS has been assessed by means of a *MHT-10* microindenter and a *FV700* indenter (*Future-Tech*), respectively, located at the Universitat Autònoma de Barcelona.

2.3.6. Nanoindentation

For sub-micron testing (i.e., nanoindentation), the size of the residual impression is too small to be measured accurately using optical techniques. Therefore, load and depth of penetration (h) are recorded during the whole experiment, both during loading and unloading. The depth of penetration together with the known geometry of the indenter provides an indirect measure of the area of contact at full load, from which the mean contact pressure, and thus hardness, may be estimated. For this reason, nanoindentation testing is often referred to as depth-sensing indentation testing.

When load is removed from the indenter, there is some degree of recovery due to the relaxation of elastic strains within the material. An analysis of the initial portion of this elastic unloading response can be used to estimate the elastic modulus of the indented material. By analyzing the initial (linear) portion of the elastic unloading response, also referred to as the stiffness ($S = \frac{dP}{dh}$), and the area of contact, A, the elastic modulus, E^*, is calculated as:

$$E^* = \frac{\sqrt{\pi}}{2\eta\sqrt{A}}\frac{dP}{dh} \text{ (Eq. 2.24).}$$

The value of η can be set to 1 in a first approximation. However, when very accurate values of the mechanical properties are required, a more accurate value of η should be determined, which is usually done by simulations [62]. The contact area is determined from the value of h_c (the depth along which contact is made with the indenter, i.e. "plastic" depth) and the known geometry of the indenter (see Figure 2.15). The value of h_c is usually found by analysis of the load-displacement data using the method of Oliver and Pharr [63,64].

Analysis of the elastic modulus by the method described above is only valid in the part where there is only elastic recovery. Note that the elastic modulus measured by depth-sensing indentation techniques does not have the same meaning as the term Young's modulus. The "indentation" or "reduced" (i.e., elastic) modulus contains contributions of both the material and the indenter, since the elastic displacements occur both in the specimen and the indenter. The reduced modulus, E^*, is related to the Young's modulus of the material by:

$$\frac{1}{E^*} = \frac{1-\nu^2}{E} + \frac{1-\nu_i^2}{E_i} \text{ (Eq. 2.25),}$$

with E and ν the Young's modulus and the Poisson's ratio of the sample and E_i and ν_i the corresponding properties of the indenter, respectively.

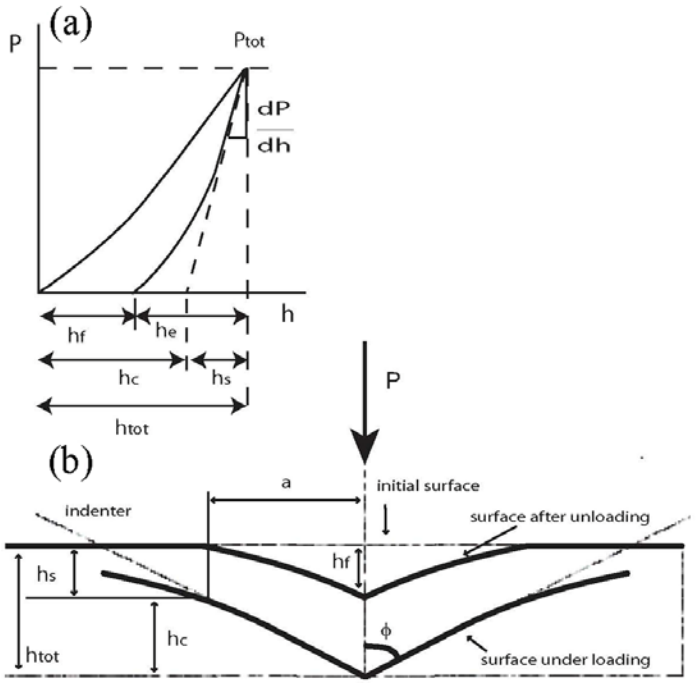

***Figure 2.15**. (a) Load versus displacement for elastic-plastic loading followed by elastic unloading from a typical nanoindentation experiment [58]. (b) Schematic illustration of the indenter and specimen surface at full load and unload and the parameters characterizing the contact geometry: h_{tot} is the total depth at full load, P_{tot}, from the original specimen surface. The depth of the contact circle h_c and slope of the elastic unloading dP/dh allow specimen modulus and hardness to be calculated. h_f is the depth of the residual impression and h_e is the displacement associated with the elastic recovery during unloading. h_s is the distance from the edge of the contact to the specimen surface at full load [63].*

The value of the indentation modulus may be affected greatly by the material behavior, e.g. pile-up around the indenter, which is not always accounted for in the analysis of the load-displacement data. For this reason, care has to be taken when comparing the modulus for materials generated by different testing techniques and on different types of specimens. Similarly, in materials which are able to recover a large amount of the elastic deformation during unloading (e.g., rubbers), hardness values measured by conventional methods after unloading can differ quite a lot from the results from nanoindentation tests, since the latter ones are calculated at the moment of maximum load, before unloading.

2.3.6.1. Working conditions

Nanoindentation experiments have been carried out with a *MTS Nanoindenter XP* at MATGAS (Bellaterra). All experiments have been performed at room temperature, in load control mode using a Berkovich indenter tip. This indenter has a resolution of 50 nN in load determination, 0.02 nm in displacement and an accuracy of 0.5 μm in positioning the tip on the specimen surface.

The indentation function consists of a loading segment, followed by a load holding segment and an unloading segment. The maximum applied loads, P_{tot}, range from 4 to 500 mN. Note that, in this Thesis, the nanoindenter has been mainly used as a lithography method rather than a mechanical testing tool.

The thermal drift has been set to stay below ± 0.05 nm/s. The hardness and modulus values have been evaluated at the end of the load holding segments using the model of Oliver and Pharr. The contact area between the diamond indenter and the specimen has been calculated from a calibration on a fused-quartz standard material. Prior to nanoindentation, the samples were carefully polished to mirror-like appearance using diamond paste and then annealed to remove any traces of ferromagnetism induced by the polishing step.

2.4. Magnetic characterization techniques

2.4.1. Vibrating sample magnetometry

A vibrating sample magnetometer (VSM), with a maximum applied magnetic field of 1.1 T, has been used to quantify the saturation magnetization values of the compressed samples (either $Fe_{60}Al_{40}$ or AISI 316L ASSs) and the AISI 316L ASS powders.

2.4.1.1. Fundamentals

The principle of this magnetometry is to measure the electromotive force induced by a ferromagnetic sample when it is vibrating at a constant frequency, under the presence of a static and uniform magnetic field, H. According to the Faraday's law, the electromotive force induced in a coil, V_{fem}, is proportional to the temporal variation of the magnetic flux passing through it:

$$V_{fem} = -\frac{d\phi}{dt} \text{ (Eq. 2.26),}$$

whit ϕ the magnetic flux and t the time [65,66].

Considering a solenoid consisting of N turns of constant cross section A, the magnetic induction inside the coil, B, can be written as follows:

$$B = \frac{\phi}{A} N \text{ (Eq. 2.27).}$$

Therefore:

$$V_{fem} = -NA\frac{dB}{dt} \text{ (Eq. 2.28).}$$

Since the sample is vibrating, the magnetic moment can be represented as $m(t)=m_0 \cdot \sin(ft)$, whit m_0 the moment amplitude and f the frequency. Since $B = \mu_0(H + M)$, $M = m/V$ (being B the magnetic induction, M the magnetization and V the volume of the sample) and the fact that H is constant, dB/dt becomes $dB/dt = (\mu_0 m_0 f/V)\cos(ft)$.

Hence, the amplitude of the induced voltage is proportional to the amplitude of the magnetic moment of the sample:

$$V_{fem} \propto fm_0G(z) \text{ (Eq. 2.29)},$$

with G(z) a function that defines the dependence of V_{fem} with respect to the sample position in the holder relative to the coils and, therefore, it depends on the design of the coils.

Essentially, the VSM measures the difference of magnetic induction between one region of space with the sample and another without the sample, thus allowing calculation of the magnetic moment, m.

2.4.1.2. Working conditions

The measurements have been carried out in an *Oxford Instruments 1.2 VSM*, at the Universitat Autònoma de Barcelona, with a maximum applied magnetic field of 1.1 T, which is generated by an electromagnet. The sample is located at the end of a rigid holder which is oscillated in the vertical direction, perpendicular to the magnetic field. The oscillation amplitude and frequency are 1.5 mm and 67 Hz, respectively. Shown in Figure 2.16 is a schematic diagram of the employed VSM.

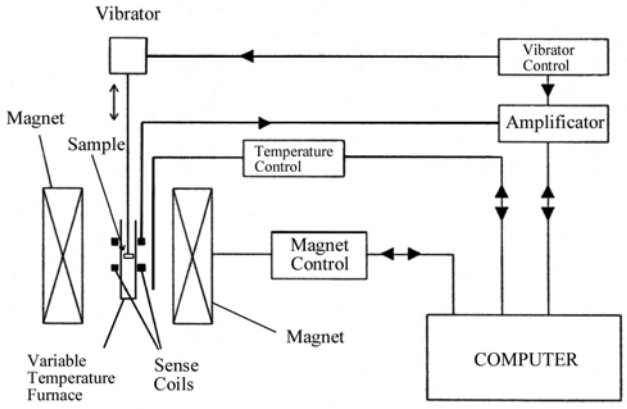

Figure 2.16. *Schematic diagram of the different components of the VSM.*

To get optimum signal the samples are previously centered in angle and height and, then, demagnetized using a sequence of alternating decreasing fields.

2.4.2. Magneto-optical Kerr effect

The magneto-optical Kerr effect (MOKE) is observed as a net rotation and elliptical polarization of incident vertically linearly polarized light as it is reflected off a magnetized sample [67]. This change in the polarization state of an incident electromagnetic wave (e.g., laser) arises due to the interaction of the electric and magnetic fields of the laser with the spin of the electrons in the material. The magnitude of this change in polarization is proportional to the magnetization of the sample. Linearly polarized light can be depicted as a combination of equal amounts of right and left circularly polarized light. Right and left circularly polarized light effectively have different indices of refraction in magnetized media as they are absorbed and emitted differentially depending on the direction and strength of the magnetization of the sample [68]. The reflected light is then the sum of unequal proportions of right and left circularly polarized light; that is, the reflected light is now elliptically polarized with its axis of polarization rotated by an amount θ_k, called the Kerr angle.

For homogeneous ferromagnetic materials, the magneto-optical effects can be considered to be linear with magnetization [69]. Therefore, by measuring the rotation or ellipticity changes as a function of the field one can probe the magnetic hysteresis curve. When used on materials with a large absorption coefficient the technique is very surface sensitive. The Kerr signal stems only from about twice the penetration depth of the employed light, which is typically about 15-30 nm for metals in the visible wavelength range. This makes the technique very surface sensitive.

In reflection mode, MOKE measurements can be made in three different optical and magnetic geometries [70], depending on the relative orientation of the magnetization M with respect to the plane of incidence of the light: the polar, the longitudinal and transverse Kerr effect.

Since the MOKE technique seldom yields an absolute value for the sample magnetization, the corresponding hysteresis loops are typically normalized to unity at saturation or given in arbitrary units.

2.4.2.1. Magneto-optical Kerr effect setup

Figure 2.17 shows a schematic illustration of the employed MOKE magnetometer. There are two optical systems combined in the apparatus, one for performing MOKE measurements and the other for imaging the sample. A plane polarized (i.e., linearly polarized) laser beam with 635 nm of wavelength is expanded and then focused to a diffraction-limited spot of up to 3 μm diameter (full width at half maximum) on the sample surface. The reflected cone is then collimated and its polarization analyzed. In addition to this magneto-optical ray path, a conventional optical microscope is formed by the halogen lamp, focusing lens, collimating and the charge-coupled device (CCD) camera. The sample surface can then be viewed by the optical microscope, while the laser spot is moved over the surface until focused on top of the working zone [71,72].

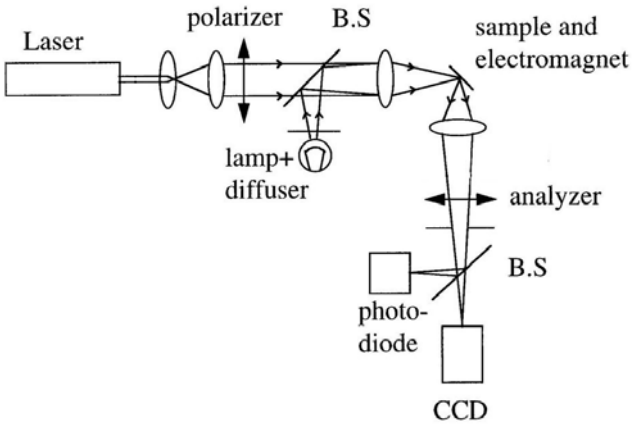

Figure 2.17*. A schematic illustration of a MOKE setup. B.S.=beam splitter [71,72].*

2.4.2.2. Working conditions

The MOKE measurements have performed in longitudinal configuration by means of either a calibrated home-made setup at the Institute of Ion Beam Physics and Materials

Research (Forschungszentrum Dresden-Rossendorf, Germany), where the changes in magnetization are given as changes in Kerr rotation, or a *Durham Magneto-Optics* apparatus at the Institut Català de Nanotecnologia. The minimum sizes of the laser spot are around 200 and 3 μm, respectively. Note that in order to present the hysteresis loops, the linear background, which takes partially into account the paramagnetic contribution, has been subtracted.

2.4.3. Magnetic force microscopy

Magnetic force microscopy (MFM) is a secondary imaging mode derived from the intermittent contact mode (*TappingMode*) of an AFM that maps magnetic force gradients above the sample surface. This is performed through a two-pass method, which is commonly known with the patented name *LiftMode* [57]. This mode separately measures topography and magnetic force gradients by using the topographical information obtained during the first pass to track the probe tip at a constant height above the sample surface during the second pass (*LiftMode*, see Figure 2.18).

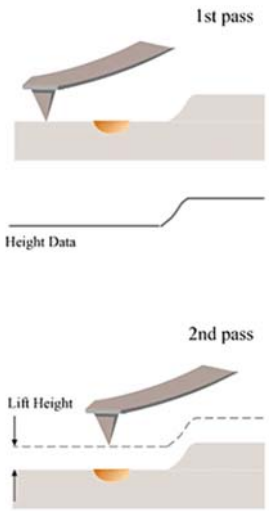

***Figure 2.18**. A schematic illustration of the two-pass method employed for MFM characterization [57].*

The MFM probe tip is coated with a ferromagnetic thin film. While scanning, it is the magnetic field's dependence on tip-sample separation that induces changes in the phase, which constitutes the feedback signal [73].

2.4.3.1. Working conditions

The AFM and MFM images corresponding to the ferromagnetic structures prepared by nanoindentation have been taken using a *Veeco/DI Multimode* apparatus at the Serveis Cientificotècnics of the Universitat de Barcelona. The AFM and MFM images of the ferromagnetic entities produced by ion irradiation have been taken using a *Veeco/DI Multimode* apparatus, with a coupled electromagnet, at the Institute of Ion Beam Physics and Materials Research (Forschungszentrum Dresden-Rossendorf, Germany). In both equipments, high-sensitivity magnetic tips have been used.

Namely, the AFM images have been recorded during the first scan and the MFM ones during the second pass at a constant height above the sample. As an order of magnitude, a lift height of around 100 nm has been utilized.

References

[1] C. Suryanarayana *Prog. Mat. Sci.* **46** 1 (2001)

[2] A. E. Ermakov, E. E. Yurchikov and V. A. Barinov *Phys. Met. Metall.* **52** 50 (1981)

[3] C. C. Koch, O. B. Cavin, C. G. McKamey and J. O. Scarbrough *Appl. Phys. Lett.* **43** 1017 (1983)

[4] B. S. Murty and S. Ranganathan *Internat. Mater. Rev.* **43** 101 (1998)

[5] D. L. Zhang *Prog. Mat. Sci.* **49** 537 (2004)

[6] P. S. Gilmann and J. S. Benjamin *Ann. Rev. Mater. Sci.* **13** 279 (1983)

[7] M. Magini, A. Iasonna and F. Padella *Scr. Mater.* **34** 13 (1996)

[8] M. Abdellaoui and E. Gaffet *Acta Metall. Mater.* **43** 1087 (1995)

[9] M. Abdellaoui and E. Gaffet *J. Alloys Compd.* **209** 351 (1994)

[10] W. A. Kaczmarek *Mat. Sci. Forum* **179-181** 313 (1995)

[11] B. S. Murty, J. Joardar and S. K. Pabi *Nanostruct. Mater.* **7** 691 (1996)

[12] C. C. Koch *Processing of Metals and Alloys, Materials Science and Technology –A Comprehensive Treatment* vol. 15, edited by R. W. Cahn (VCH, Weinheim, 1991)

[13] R. B. Schwarz and C. C. Koch *Appl. Phys. Lett.* **49** 146 (1986)

[14] M. Magini, N. Burgio, A. Iasonna, S. Martelli, F. Padella and E. Paradiso *J. Mater. Synth. Process.* **1** 135 (1993)

[15] Z. Caamaño, G. Pérez, L. E. Zamora, S. Suriñach, J. S. Muñoz and M. D. Baró *J. Non-Cryst. Solids* **287** 15 (2001)

[16] M. A. Morris and D. G. Morris *Mater. Sci. Eng. A* **136** 59 (1991)

[17] E. Menéndez, J. Sort, A. Concustell, S. Suriñach, J. Nogués and M. D. Baró *Nanotechnology* **18** 185609 (2007)

[18] E. Dieter *Mechanical Metallurgy* (McGraw-Hill, London, 1988)

[19] M. Nastasi, J. W. Mayer and J. K. Hirvonen *Ion-solid interactions: fundamentals and applications* (Cambridge University Press, Cambridge, 1996)

[20] J. F. Ziegler, J. P. Biersack and U. Littmark *The stopping and range of ions in solids* (Pergamon Press, Inc., New York, 1985)

[21] *Ion implantation Science and Technology* edited by J.F. Ziegler (Academic Press, Inc., London, 1988)

[22] W. Möller *Fundamentals of Ion-surface Interaction* Resume of a lecture held at the Technical University of Dresden 2003/04

[23] R. S. Averback, R. Benedek and K. L. Merkle *J. Nucl. Mater.* **69&70** 786 (1978)

[24] TRIM program is included in the SRIM (*the Stopping Range of Ions in Matter*) package, see http://www.srim.org, J. F. Ziegler, M. D. Ziegler and J. P. Biersack

[25] G. H. Kinchin and R.S. Pease *Rep. Prog. Phys.* **18** 1 (1955)

[26] N. Matsunami, Y. Yamamura, Y. Itikawa, N. Itoh, Y. Kazumata, S. Miyagawa, K. Morita, R. Shimizu and H. Tawara *Energy dependence of the ion-induced sputtering yields of monoatomic solids*, *atomic data and nuclear data tables* **31** 1 (1984)

[27] Adapted from http://www.danfysik.com

[28] G. Abrasonis *Doctoral Dissertation* Université de Poitiers, France (2003)

[29] M. Zeuner, J. Meichsner, H. Neumann, F. Scholze and F. Bigl *J. Appl. Phys.* **80** 611 (1996)

[30] C. Blawert, B. L. Mordike, G. A. Collins, K. T. Short, J. Tendys *Surf. Coat. Technol.* **103&104** 240 (1998)

[31] *Focused ion beam microscopy and micromachining* C. A. Volkert and A. M. Minor Guest Editors *MRS Bulletin* **32** 389 (2007)

[32] J. Mayer, L. A. Giannuzzi, T. Kamino and J. Michael *MRS Bulletin* **32** 400 (2007)

[33] W. J. MoberlyChan, D. P. Adams, M. J. Aziz, G. Hobler and T. Schenkel *MRS Bulletin* **32** 424 (2007)

[34] J. Orloff *Rev. Sci. Instrum*. **64** 1105 (1993)

[35] J. F. Smyth, S. Schultz, D. Kern, H. Schmid and D. Yee *J. Appl. Phys.* **63** 4237 (1988)

[36] P. B. Fischer and S. Y. Chou *Appl. Phys. Lett.* **62** 2989 (1993)

[37] J. I. Martín, J. Nogués, K. Liu, J. L. Vicent and I. K. Schuller *J. Magn. Magn. Mater.* **256** 449 (2003)

[38] W. L. Bragg *Proc. Camb. Phil. Soc.* **17** 43 (1912)

[39] B. D. Cullity *Elements of X-Ray Diffraction* (Addison-Wesley Publishing Company, Inc., Boston, 1978)

[40] H. P. Klug and L. E. Alexander *X-Ray Diffraction Procedures* (Wiley, New York, 1974)

[41] L. Lutterotti and P. Scardi *J. Appl. Cryst.* **23** 246 (1990)

[42] S. Enzo, G. Fagherazzi, A. Benedetti and S. Polizzi *J. Appl. Cryst.* **21** 536 (1988)

[43] *PCPDFWIN* JCPDS-ICDD (1997)

[44] J. I. Langford and D. Louër *Rep. Prog. Phys.* **59** 131 (1996)

[45] X. Amils, J. Nogués, S. Suriñach, J. S. Muñoz, L. Lutterotti, S. Gialanella, M. D. Baró *Nanostruct. Mater.* **11** 689 (1999)

[46] S. Gialanella, X. Amils, M. D. Baró, P. Delcroix, G. Le Caër, L. Lutterotti, S. Suriñach *Acta Mater.* **46** 3305 (1998)

[47] R. A. Young *The Rietveld Method* (International Union of Crystallography, University Press, Oxford, 1995)

[48] G. K. Williamson and W. H. Hall *Acta Metall.* **1** 22 (1953)

[49] B. E. Warren *X-ray Diffraction* (Addison-Wesley, Massachusetts, 1969)

[50] F. Lecroise and A. Pineau *Metall. Trans.* **3** 387 (1972)

[51] J. I. Goldstein *Scanning Electron Microscopy and X-Ray Microanalysis* (Plenum Press, New York, 1981)

[52] B. C. De Cooman *Observation techniques in materials science* Lecture notes Ghent University (2000)

[53] L. Reimer *Scanning Electron Microscopy* (Springer Verlag, New York, 1985)

[54] G. Lawes *Scanning Electron Microscopy and X-Ray Microanalysis* (John Wiley & Sons, New York, 1987)

[55] E. Meyer, H. J. Hug and R. Bennewitz *Scanning Probe Microscopy: The Lab on a Tip* (Springer-Verlag, New York, 2003)

[56] Adapted from http://nisenet.org

[57] http://www.veeco.com

[58] A. C. Fischer-Cripps *Nanoindentation* (Springer-Verlag, New York, 2004)

[59] N. K. Mukhopadhay and P. Paufler *Int. Mater. Rev.* **51** 209 (2006)

[60] E. Meyer *Phys. Z.* **9** 66 (1908)

[61] *Hardness Testing* edited by H. Chandler (ASM International, 1999)

[62] W. C. Oliver and G. M. Pharr *J. Mat. Res.* **19** 3 (2004)

[63] W.C. Oliver and G.M. Pharr *J. Mat. Res.* **7** 1564 (1992)

[64] A.C. Fischer-Cripps *Vacuum* **58** 569 (2000)

[65] J. R. Reitz, F. J. Milford and R. W. Christy *Foundations of electromagnetic theory* (Addison-Wesley, New York, 1979)

[66] S. Chikazumi *Physics of Magnetism* (John Wiley & Sons, Inc., New York, 1964)

[67] P. N. Argyres *Phys. Rev.* **97** 334 (1954)

[68] S. D. Bader *J. Magn. Magn. Mater.* **100** 440 (1991)

[69] W. Geerts *Ph.D. Thesis* University of Twente, The Netherlands (1992)

[70] A. Hubert and R. Schafer *Magnetic Domains. The Analysis of Magnetic Microstructures* (Springer, Berlin, 1998)

[71] D. A. Allwood, G. Xiong, M. D. Cooke and R. P. Cowburn *J. Phys. D: Appl. Phys.* **36** 2175 (2003)

[72] R. P. Cowburn, D. K. Koltsov, A. O. Adeyeye and M. E. Welland *Appl. Phys. Lett.* **73** 3947 (1998)

[73] D. Sarid *Scanning Force Microscopy: With Applications to Electric, Magnetic, and Atomic Forces* (Oxford University Press, New York, 1994)

3. Results and discussion

This chapter deals with the main results of this Thesis and their discussion. Since this work is primarily focused on the generation of ferromagnetism on either $Fe_{60}Al_{40}$ (at. %) alloys or austenitic stainless steels (ASSs), this leads to the division of the chapter in two major sections, each dealing with one of the studied materials. Both sections start reporting on the origin of ferromagnetism by mechanical deformation (part A) in a macroscopic approach. Next, the results regarding the generation of micro/nanoscaled ferromagnetic entities (i.e., magnetic patterning) by means of local mechanical deformation are presented. Finally, the irradiation-induced ferromagnetism investigation (part B) is reported starting from the macroscopic approach, followed by the magnetic patterning using ion irradiation.

3.1. $Fe_{60}Al_{40}$ (at. %) alloys

3.1.A. Ferromagnetism induced by mechanical deformation

3.1.A.1. Macroscopic approach: compression tests

The transition from the atomically ordered B2-phase to the chemically disordered A2-phase, accomplished by means of compression procedures, and the concomitant deformation-induced ferromagnetism have been investigated in bulk polycrystalline $Fe_{60}Al_{40}$ (at. %) alloys. A detailed correlation between structural, magnetic and mechanical properties has been carried out.

3.1.A.1.1. Experimental details

Gas atomized $Fe_{60}Al_{40}$ (at. %) powders have been pressure-less sintered at 1150 ºC during 30 minutes of isothermal holding, in a tubular furnace under vacuum (air pressure < 10^{-5} mbar), in order to produce bulk specimens. The heating and cooling rates have been chosen to be of 5 ºC/min in order to promote the sintering process. Note that since the employed processing temperature is below any transition temperature of the Fe-Al binary system [1], the process can be considered as solid state sintering. Subsequently, cubic-shaped specimens (8 mm^3 in volume) have been cut and polished from two opposite sides up to mirror-like appearance, with the aim of obtaining parallel faces. Since both cutting and polishing steps already induce disorder (i.e., atomic intermixing and, thus, ferromagnetism), the samples have been annealed for 30 minutes at 650 ºC, under vacuum (air pressure < 10^{-5} mbar), in order to remove these ferromagnetic contributions, taking advantage of the annealing-induced atomic reordering processes which recover the non-ferromagnetic state.

The compression processes have been performed uniaxially, at room temperature, using a loading of 1 kN/s and a dwell time of 100 s. Different engineering stresses have been applied: 0.5, 2, 3, 4, 6 and 8 GPa. In addition, in order to investigate the loading rate

influence on the induced magnetic properties, additional compression tests have been also carried out at 0.1 kN/s.

The overall microstructural parameters, such as lattice cell parameters (*a*), crystallite sizes (<D>), microstrains ($<\varepsilon^2>^{1/2}$) and anti-site probabilities of Fe atoms at the Al positions (w_{Fe}) have been evaluated by fitting the full XRD patterns by means of the Rietveld refinement program MAUD. The Vickers microhardness of the bulk samples has been determined using a maximum load of 0.1 kg ($H_{V0.1}$), a holding time of 10 s and a slope (ratio between the applied force and time to obtain the target force value) of 0.16 N/s.

Finally, the magnetic characterization has been performed at room temperature by means of VSM. The saturation magnetization has been calculated from a least square fitting of the initial magnetization curves to the classical law of approach to saturation:

$$M = M_S \cdot (1 - \frac{a}{H} - \frac{b}{H^2}) + \chi \cdot H \quad \text{(Eq. 3.1)},$$

with H the applied magnetic field, M_S the saturation magnetization, χ the field independent susceptibility, and a and b coefficients which depend on the magnetic properties of the material [2].

3.1.A.1.2. Structural characterization

The XRD patterns of the as-annealed $Fe_{60}Al_{40}$ (at. %) sample and the bulk specimens compressed up to 2, 4 and 8 GPa (using a loading rate of 1 kN/s and a dwell time of 100 s) are shown in Figure 3.1.

The virgin sample (i.e., as-annealed) exhibits a XRD pattern consistent with an atomically ordered body-centered cubic (BCC) lattice structure (i.e., B2-phase). Conversely, for the pressed samples at applied engineering stresses ≥ 3 GPa, super-lattice XRD peaks –denoted as SLP– essentially vanish (see Figure 3.1), evidencing that

a severe atomic disordering process occurred upon deformation (i.e., leading to the so-called A2-phase). Nevertheless, for the mildest conditions (i.e., 0.5 and 2 GPa), some traces of the SLP peaks are still detectable (e.g., see the (210) super-lattice peak, located at $2\theta \approx 73º$, for the sample compressed at 2 GPa), indicating that a less intense atomic intermixing (i.e., disordering) process takes place.

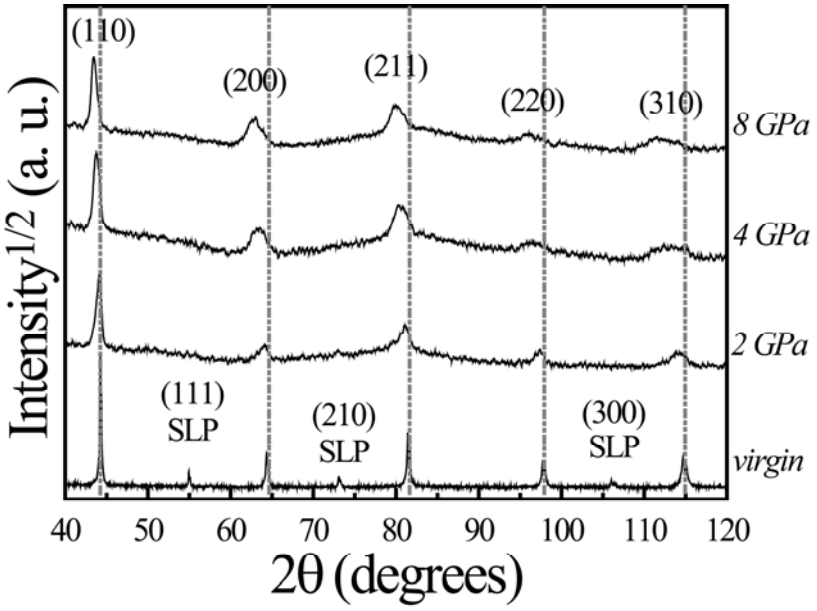

Figure 3.1. *X-ray diffraction patterns of the as-annealed $Fe_{60}Al_{40}$ (at. %) sample and the specimens compressed uniaxially up to 2, 4 and 8 GPa using a loading rate of 1 kN/s and a dwell time of 100 s. The Miller indexes of the different peaks have also been indicated in the figure. Note that SLP denotes super-lattice peaks.*

From the X-ray line profile analysis, it can be inferred that a highly ordered structure is obtained for the as-annealed sample ($w_{Fe} = 0.25$, thus LRO = 0.70), whereas a nearly fully disordered state is already attained for samples tested at ≥ 3 GPa ($w_{Fe} \approx 0.50$, thus LRO ≈ 0.20). However, intermediate states are achieved for specimens tested at 0.5 and 2 GPa ($w_{Fe} = 0.34$, thus LRO = 0.52 and $w_{Fe} = 0.41$, therefore LRO = 0.38, respectively) –see Table 3.1–. Hence, two clear regimes can be identified: a low-stress regime where disorder is generated by the stress and a high-stress regime where disorder remains virtually unchanged despite the increased stress. Nevertheless, given the restricted penetration of X-rays (limited to a few microns, see section 2.3.1.6.1.) [3], the obtained long-range order parameter values are to some extent upper limits since the surface might have suffered more plastic deformation than the inner parts.

As the applied engineering stress increases, a broadening of the XRD peaks is observed due to either crystallite size refinement or increase of microstrains (see both Figure 3.1 and Table 3.1), since the amount of plastic deformation increases with the applied stress. Interestingly, while the crystallite size decreases slightly with the applied stress, the microstrain increases considerably (see Table 3.1). Similar to the LRO parameter, they both tend to saturate for applied stresses above 3 GPa.

Engineering Stress (GPa)	a ($\pm 5\cdot10^{-4}$ Å)	LRO	<D> ($\pm$ 5 nm)	$\langle\varepsilon^2\rangle^{1/2}\cdot10^{-3}$ ($\pm$ 0.5)	M_S ($\pm$ 2 emu/g)	$H_{V0.1}$ (GPa)
0 (virgin)	2.8943	0.70 ± 0.02	> 200	< 0.5	< 2	2.9 ± 0.2
0.5	2.8947	0.52 ± 0.02	165	1.1	< 2	3.2 ± 0.2
2	2.9118	0.38 ± 0.03	120	6.1	8	5.0 ± 0.3
3	2.9195	0.22 ± 0.05	101	8.9	21	6.4 ± 0.3
4	2.9250	0.21 ± 0.05	96	8.5	46	7.3 ± 0.3
6	2.9325	0.23 ± 0.05	86	8.2	55	7.6 ± 0.3
8	2.9329	0.20 ± 0.05	85	8.7	65	7.6 ± 0.3

Table 3.1. *Lattice cell parameter, a, long-range order parameter, LRO, crystallite size, <D>, microstrain, $\langle\varepsilon^2\rangle^{1/2}$, saturation magnetization, M_S, and microhardness, $H_{V0.1}$, of the as-annealed sample and the uniaxially compressed specimens up to 0.5, 2, 3, 4, 6 and 8 GPa using a loading rate of 1 kN/s and a dwell time of 100 s.*

Furthermore, as the applied engineering stress increases, the lattice cell parameter, a, expands –see Table 3.1– up to $\Delta a/a$ values of around 1.3 % for the sample pressed at 8 GPa. This phenomenon is clearly evidenced by the shift of the XRD peaks to lower scattering angles (i.e., larger lattice cell parameters) as the stress increases. Remarkably, in contrast with the LRO parameter which remains rather constant for high-stress regime (≥ 3 GPa), the lattice cell parameter exhibits a continuous increase.

3.1.A.1.3. Magnetic characterization

The dependence of the magnetization of the as-annealed sample on the applied magnetic field evidences a clear paramagnetic behavior (i.e., a linear relationship between magnetization and applied magnetic field, see the inset of Figure 3.2), confirming the existence of an atomically ordered structure (B2-phase). This is in agreement with previously reported results on annealed $Fe_{60}Al_{40}$ (at. %) powders, where the ordered B2-phase shows no hysteretic behavior [4-6].

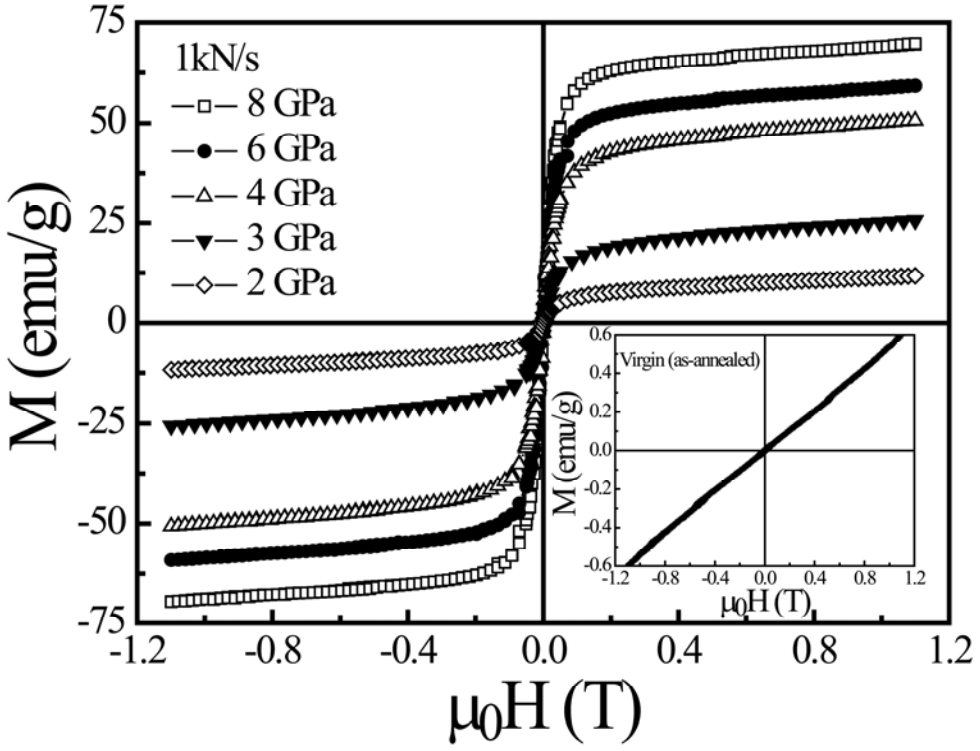

Figure 3.2. *Vibrating sample magnetometry (VSM) measurements of the $Fe_{60}Al_{40}$ (at. %) specimens compressed uniaxially up to 2, 3, 4, 6 and 8 GPa using a loading rate of 1 kN/s and a dwell time of 100 s. Shown in the inset is the VSM measurement of the as-annealed sample.*

In addition, the specimen compressed at 0.5 GPa also evidences practically no ferromagnetism. Conversely, the rest of the compressed samples show a clear hysteretic behavior (see Figure 3.2). The saturation magnetization, M_S, increases with the applied engineering stress (see Table 3.1), therefore confirming the increase of the ferromagnetic counterpart. The augment in M_S can be ascribed to the simultaneous increase of both atomic intermixing and lattice cell parameter [7,8]. However, when comparing LRO and M_S values –Figure 3.3 (a)–, it can be observed that while the LRO

already reaches a small constant value (disordered state) for tests carried out above 3 GPa, the ferromagnetism continuously increases up to 8 GPa. Contrarily, in the high-stress regime, the lattice parameter continues to increase with higher stress in a way similar to M_S –see Figure 3.3 (b)–. Consequently, from these results it can be inferred that the contribution from the lattice cell expansion to the ferromagnetic response seems to be significant, especially, at the high applied stresses regime. Interestingly, although the contribution of the lattice expansion to the magnetism of FeAl alloys was proposed for ball-milled powders [5,6], it was only confirmed through complex high pressure dichroism experiments [8]. Here, the two-fold origin to the ferromagnetic response of FeAl alloys is directly observed.

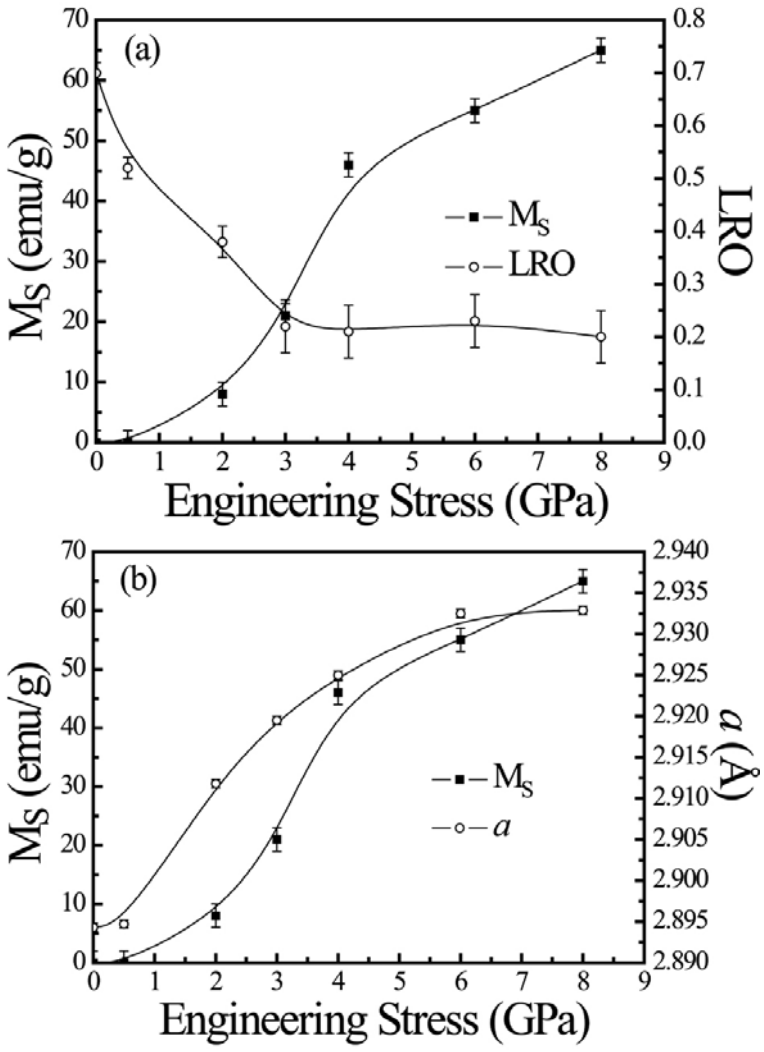

Figure 3.3. *(a) Dependence of the saturation magnetization, M_S, and long-range order parameter, LRO, on the applied engineering stress. (b) Dependence of M_S and lattice cell parameter, a, on engineering stress. The lines are guides to the eye.*

In addition, the current experiments indicate that probably two regimes exist in the deformation-induced magnetism in these alloys. Note that in ball milling experiments, due to the high strain rate conditions of milling, these two regimes are difficult to separate.

According to the literature, the saturation magnetization of $Fe_{60}Al_{40}$ powders in the A2-phase (with a long-range order parameter and a lattice cell spacing of LRO = 0.14 and a = 2.9170 Å $-\Delta a/a \approx 0.7$ %–, respectively), achieved after long-term milling, is around 75 emu/g [5,8]. Here, the obtained value of saturation magnetization for the sample pressed at 8 GPa is around 65 emu/g (highest value). Nevertheless, slightly greater lattice cell expansions are achieved in the present investigation. This difference in the attained saturation magnetization values may be somewhat due to the fact that the obtained level of disorder is slightly lower than that reported in ball-milled samples, although a gradient of induced defects (i.e., more disorder at the surface) cannot be ruled out.

The possible influence of the strain rate has also been investigated. In fact, strain rate is often one of the factors affecting the mechanical response of materials (e.g., the austenite (γ) to martensite (α') transformation in austenitic stainless steels, see section 3.2.A.) [9]. Thus, compression tests at 0.1 kN/s have been also performed and the resulting magnetic response investigated. As it can be seen in Figure 3.4, the VSM measurements of specimens pressed at 0.1 kN/s render similar results to compression at 1 kN/s, indicating that this order-disorder transformation is not especially sensitive to strain rate changes, at least within the assessed strain rate regime (i.e., quasi-static range).

However, in the dynamic (i.e., high strain rate range) regime (e.g., impact shock loading), differences have been observed when decreasing/increasing the strain rate. Namely, ball milling processes of $Fe_{60}Al_{40}$ (at. %) powders at higher milling intensities (i.e., larger angular frequencies) lead to a larger ferromagnetic response [10]. Thus, since the deformation modes used in compression (quasi-static) and ball milling

(dynamic) are different, the univocal comparison between the results of both types of specimens may be rather complex.

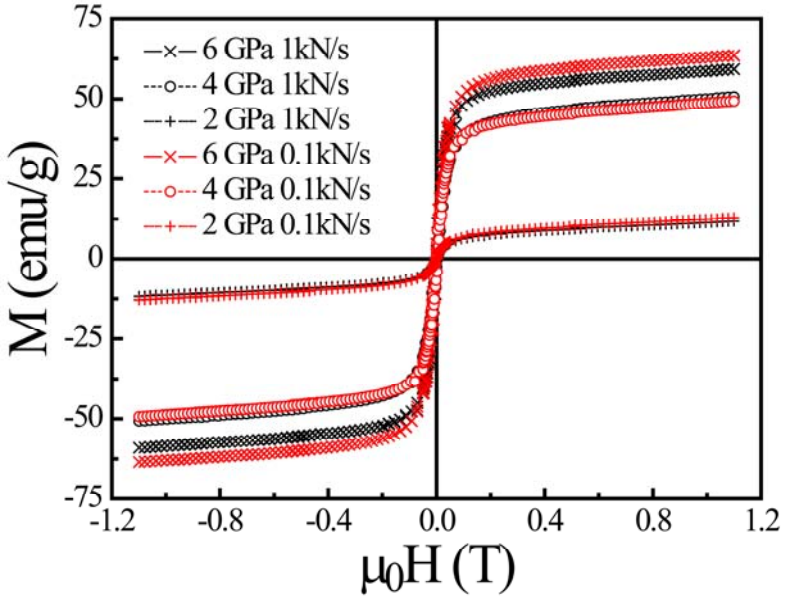

***Figure 3.4**. Vibrating sample magnetometry measurements of the $Fe_{60}Al_{40}$ (at. %) samples compressed uniaxially up to 2, 4 and 6 GPa using a loading rate of 0.1 kN/s (in red) and 1 kN/s (in black) and a dwell time of 100 s.*

3.1.A.1.4. Mechanical hardness characterization

In FeAl alloys, plastic deformation causes simultaneously both a magnetic transformation and a mechanical hardening process [10]. Concerning the studied samples, the mechanical hardness, measured by means of Vickers microhardness using a load of 0.1 kg, shows a progressive increase with the applied engineering stress from $H_{V0.1}$ = 2.9 GPa (as-annealed sample) to $H_{V0.1}$ = 7.6 GPa (specimen compressed at 8 GPa). Hence, the order-disorder transition can be also indirectly assessed by means of hardness measurements. In fact, there is a pronounced microhardness increase for low-stress range followed by a steady-state like behavior. Therefore, the hardening effect is particularly significant for low processing stresses. Interestingly, as it can be seen in Figure 3.5, the $H_{V0.1}$ vs. engineering stress and M_S vs. engineering stress curves show a similar trend during compression tests, as observed for ball-milled powders [6].

Several processes are responsible for the mechanical hardening phenomena. Actually, it is known that disorder-solution processes (i.e., solution of anti-sites in the ordered matrix –formation of anti-phase boundary walls–) play an important role in hardening. Nevertheless, other structural effects (vacancies, dislocations or grain refinement processes –i.e., Hall-Petch behavior–) could also contribute to some extent to the aforementioned mechanical hardening [11-13].

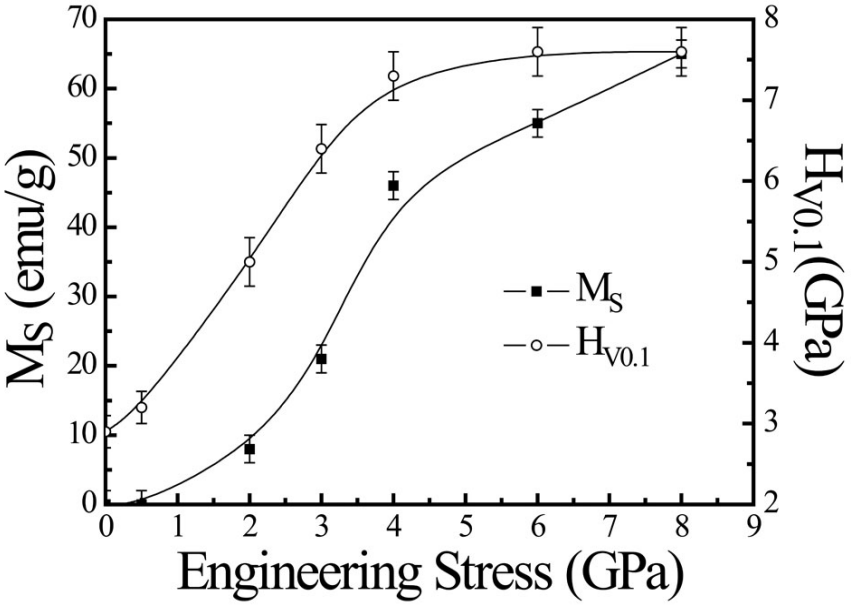

Figure 3.5*. Dependence of the induced saturation magnetization, M_S, and the microhardness, $H_{V0.1}$, on the applied engineering stress. The lines are visual guides.*

3.1.A.2. Micro and nanoscaled approaches: nanoindentation

Periodic arrays of micron and sub-micron magnetic structures have been prepared, in a single step, by means of nanoindentation experiments, taking advantage of the property of $Fe_{60}Al_{40}$ (at. %) alloys to become ferromagnetic when subjected to plastic deformation.

3.1.A.2.1. Experimental details

A fully dense sheet of $Fe_{60}Al_{40}$ (at. %) with thickness of around 200 μm, prepared by repeated cold rolling and annealing of the alloyed powders [14,15], has been mechanically polished using diamond paste until mirror-like appearance. Subsequently, in order to completely eliminate possible magnetic contributions introduced during the synthesis process, the sheet has been annealed at 650 ºC for 30 min, under vacuum (air pressure < 10^{-5} mbar), and slowly cooled down to room temperature. Note that this temperature is well above the temperature range within which atomic reordering of this alloy occurs [16,17].

Arrays of 12 × 12 triangular indentations with lateral sizes of 0.8 and 1.7 μm have been prepared by means of nanoindentation, operating in the load control mode, using a Berkovich-type diamond indenter (pyramidal-shaped). The indentation function consists of a loading segment of 30 s, applying a peak force of 3 mN and 12 mN respectively, a load holding segment of 10 s and an unloading segment of 15 s. Larger indentations have been also performed by increasing the peak force (up to 500 mN, with produced indentations with lateral size of approximately 19 μm). An array of lines (30 μm long) has been also prepared by dragging the indenter tip at 10 μm/s applying a constant load of 12 mN.

The morphology of the locally deformed regions has been examined by SEM and AFM. Hysteresis loops of the deformed and non-deformed areas have been recorded using MOKE magnetometry. MFM has been used to check the local character of the induced ferromagnetism and to probe possible domain patterns within the indented regions.

3.1.A.2.2. Magnetic patterning

Shown in Figures 3.6 (a) and (b) are the scanning electron microscopy images, obtained using secondary electrons, of the arrays of indentations produced on a $Fe_{60}Al_{40}$ (at. %) sheet applying peak forces of 3 and 12 mN, respectively. Due to the pyramidal shape of the indenter, the indentations exhibit a roughly triangular shape –also evidenced from

the atomic force microscopy image shown in Figure 3.6 (c)– and, for these force values, have a lateral size of approximately 0.8 μm –panel (a)– and 1.7 μm –panel (b)–.

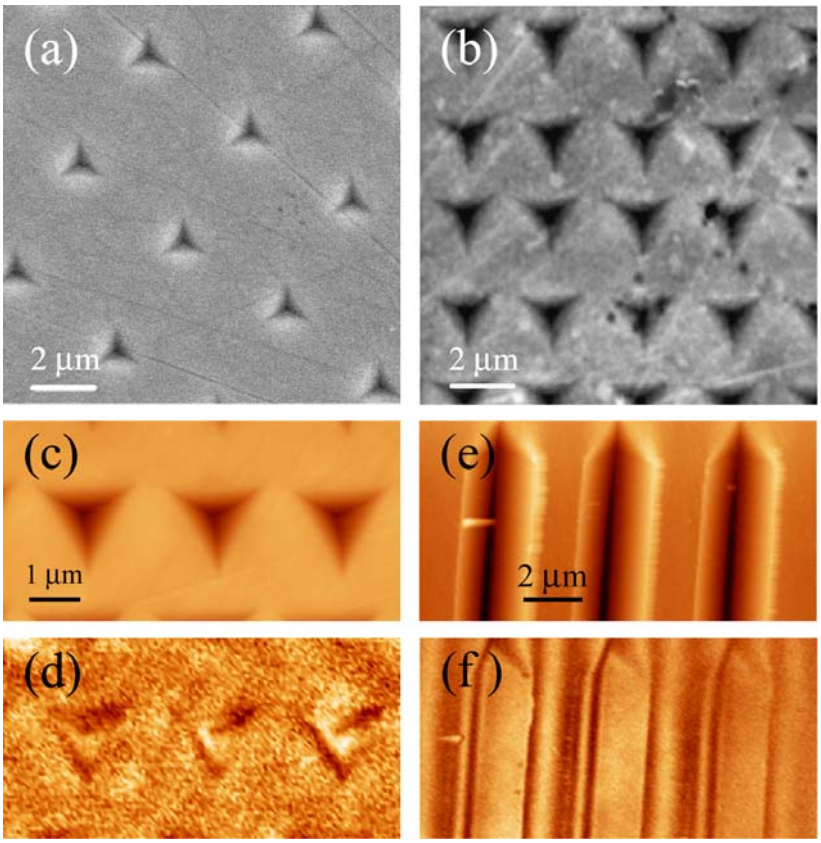

***Figure 3.6**. (a) Scanning electron microscopy (SEM) image of the array of indentations obtained applying a peak force of 3 mN. (b) SEM image of the array of indentations after applying 12 mN. (c) Atomic force microscopy (AFM) of the array of indentations obtained applying 12 mN with (d) the corresponding magnetic force microscopy (MFM) image; (e) AFM picture of the array of lines obtained by dragging the nanoindenter at a constant load of 12 mN with (f) the corresponding MFM image.*

Note that although triangular-shaped structures have been imprinted, other morphologies, such as squares or circles, are also possible to prepare by simply changing the nanoindenter tip. Moreover, other patterns, e.g., lines, can also be easily produced by dragging the indenter tip on the surface –see Figure 3.6 (e)–.

The dependence of the displacement into the sample, penetration depth, on the applied force, F, during the loading, load holding and unloading segments, for the indentations performed with an applied peak force of 3 mN, is shown in Figure 3.7 (a). From the analysis of the whole array of 12 × 12 indentations, an average hardness of 5.5 GPa

(whose order of magnitude is in agreement with ball-milled $Fe_{60}Al_{40}$ (at. %) powders and pressed specimens) and a reduced elastic modulus of 210 GPa are obtained [18]. The shape of the curve in Figure 3.7 (a) reveals that the material behaves rather plastically in spite of the relatively small value of the applied peak force. Essentially, if the peak force during loading is increased, the size of the indentations concomitantly increases, as indicated in Figure 3.7 (b). From the curve, it is clear that smaller nanostructures, well in the sub-micron range, should be also feasible.

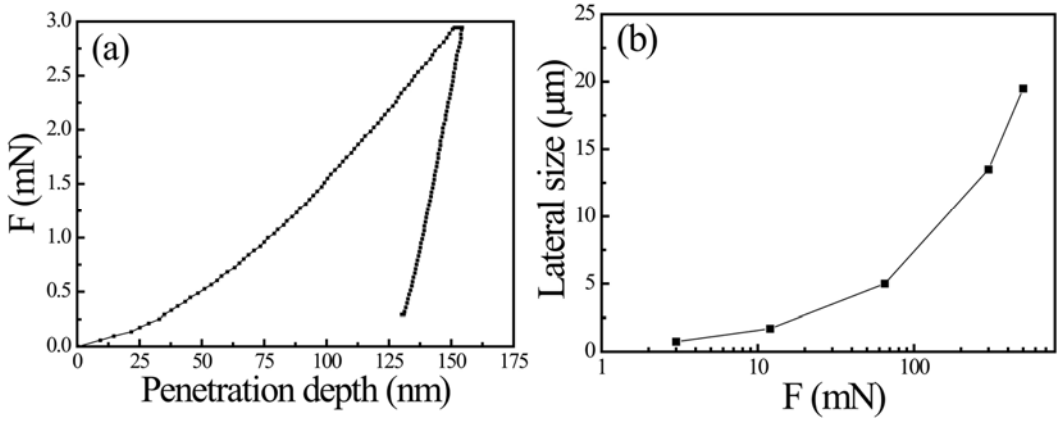

***Figure 3.7**. (a) Relationship between the applied force, F, and the displacement into the sample (i.e., penetration depth) during the loading, load holding and unloading segments for the indentations performed with a applied peak force of 3 mN; (b) dependence of the lateral size of the indentation on the applied force during the nanoindentation. The lines are visual guides.*

The magnetic properties of these sheets have been investigated by means of MOKE magnetometry. Figure 3.8 (a) reveals that when the MOKE measurement is carried out away from the array of indentations (i.e., undeformed material), a straight line is obtained, which is characteristic of a non-ferromagnetic material. This is expected since the unprocessed material should remain atomically ordered (and, hence, paramagnetic [5,16,17,19-21]). Conversely, when MOKE measurements are carried out in the indented region, a hysteresis loop, consequence of ferromagnetic behavior, is obtained –Figure 3.8 (b)–. The coercivity is approximately $\mu_0 H_C$ = 5.5 mT, which is slightly larger than those ones corresponding to the compressed samples, obtained by vibrating sample magnetometry (e.g., $\mu_0 H_C$ = 1.7 mT for the sample pressed at 8 GPa). Note that the laser spot of the MOKE system is focused down up to 3 μm in diameter, therefore only a few structures are measured in Figure 3.8 (b). However, similar results are obtained when the laser spot is defocused, covering the complete array, attesting the homogeneity of

the produced ferromagnetic entities. The hysteresis loop corresponding to larger structures, with size of 1.7 μm (obtained by applying a peak force of 12 mN) is shown in Figure 3.8 (c). The loop shape is similar to the one from the smallest magnetic elements, although the coercivity is slightly smaller, $\mu_0 H_C$ = 4.5 mT, since constraints in domain wall propagation are less pronounced [2]. Similar H_C values are obtained for larger indentations.

For the array of lines, H_C is found to depend on the direction of measurement. Namely, the coercivity evaluated from the loop recorded along the direction of the lines is $\mu_0 H_C$ = 4.0 mT and it increases progressively as the angle of measurement approaches 90º from the direction of the lines, reaching a maximum value of 10 mT. Similar H_C angular dependences have been observed in other arrays of ferromagnetic lines and can be interpreted as a result of the competition between magneto-static energy and anisotropy energy [22-24].

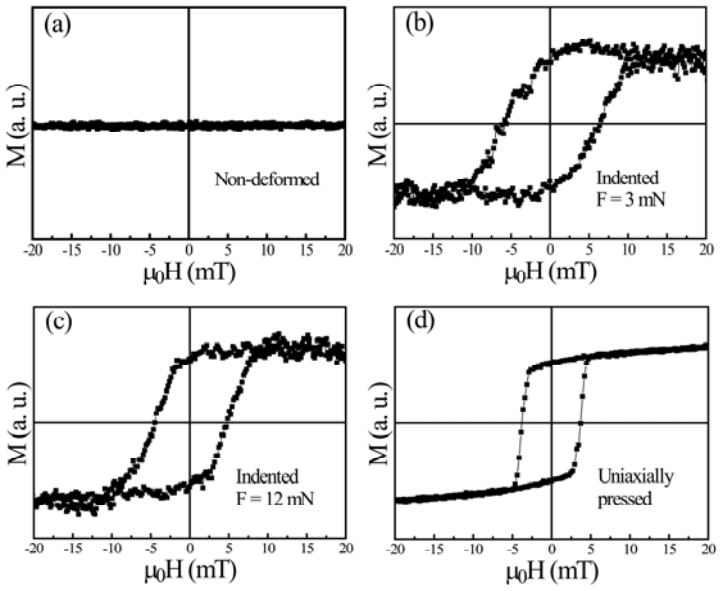

***Figure 3.8**. (a) Dependence of the magneto-optical Kerr effect (MOKE) signal on the applied magnetic field for a non-deformed region; (b) and (c) hysteresis loops corresponding to the locally deformed (i.e., full array of indentations) regions when loading with a peak force of 3 mN and 12 mN, respectively; (d) MOKE hysteresis loop recorded on a piece of sheet uniaxially pressed at 2 GPa (1kN/s).*

Unfortunately, it is not possible to easily determine the amount of atomic disorder locally introduced to these alloys during the nanoindentation experiments. Nevertheless,

taking into account the results of the macroscopic approach, it is plausible to ascribe the occurrence of the ferromagnetic behavior to deformation-induced atomic disorder. In fact, the sample pressed uniaxially at 2 GPa and 1 kN/s has been also characterized by MOKE. Even though this pressure is slightly smaller than the pressure applied during nanoindentation, which is typically of the order of several GPa [25], X-ray diffraction measurements (see Figure 3.1) reveal that application of such pressure already decreases the intensity of the super-lattice peaks, which is an indication of the induced atomic disorder. Indeed, after uniaxially pressing the FeAl sheet at 2 GPa, the order parameter (extracted by adjusting the XRD pattern using the Rietveld method) is reduced to LRO = 0.38 [26]. The corresponding hysteresis loop of the pressed sheet has been also recorded by MOKE –see Figure 3.8 (d)–. On the one hand, the coercivity, $\mu_0 H_C$ = 3.3 mT, is slightly larger than that one obtained by VSM (see Figure 3.2) because of MOKE is a surface sensitive technique and, thus, surface may contain larger amounts of structural defects. On the other hand, H_C for the uniaxially pressed sample is slightly smaller than those for the arrays of sub-micron and micron structures. Moreover, the loop is less tilted and more square-shaped. Specifically, the tilted shape of the hysteresis loops in the indented regions is probably due to the existence of structural and/or morphological differences among the indentations, which is known to broaden the switching field distribution [27]. H_C, in magnetic patterned elements, is usually larger than for continuous films with the same composition. This is typically ascribed to the constrains that the reduced dimensions of the dots impose on the nucleation and propagation of magnetic domain walls [22,27]. Furthermore, the differences in coercivity may be due to different degrees of structural disorder. Actually, H_C is known to depend on the degree of atomic disorder in a rather complex way [21]. Note that, since locally the stress fields generated by the indenter are much more pronounced than in the experiments using uniaxial pressure, the magnetic effects from atomic disorder could be probably exacerbated in nanoindentation experiments. Therefore, although the saturation magnetization value corresponding to the uniaxially pressed sample at 2 GPa is around 8 emu/g (see Table 3.1), magnetization values could reach in excess of 70 emu/g within the indented structures [5].

The local character of the ferromagnetism induced by nanoindentation has been examined by MFM. Some MFM images, with the corresponding atomic force

microscopy images, of the array of indentations with 1.7 μm lateral size and the array of lines are shown in Figures 3.6 (d) and (f), respectively. Dark and bright areas are observed inside the indentations, indicating a multidomain structure, while no contrast is observed outside the indentations (except for the material surrounding each of the written lines –i.e., pile-up phenomenon–, which is also affected, to some extent, by the plastic deformation induced during the scratch experiment). Similar images have been obtained for the indentations with 0.8 μm lateral size. These MFM images are not straightforward to interpret because the surfaces are not flat and both in-plane and out-of-plane magnetization components probably coexist. However, MFM confirms that the nanoindentation experiments can induce ferromagnetism locally.

The indented FeAl sheet has been finally annealed at progressively higher temperatures. For annealing temperatures higher than 450 ºC, this process results in a MOKE signal without hysteresis, resembling the straight line shown in Figure 3.8 (a). Namely, the magnetic information is removed, although the physical topography caused by the indentations still remains.

3.1.B. Ferromagnetism induced by ion irradiation

3.1.B.1. Macroscopic approach: broad beam irradiation

In this section, the capability to induce ferromagnetism on paramagnetic sheets of $Fe_{60}Al_{40}$ (at. %) by noble gas ion irradiation has been investigated. In particular, the effect of different ion masses on the disordering efficiency (and thus on the generated ferromagnetism) of the atomically ordered $Fe_{60}Al_{40}$ alloys has been enlightened. Finally, the induced ferromagnetism has been correlated with the structural modifications caused by the irradiation procedures.

3.1.B.1.1. Experimental details

Bulk polycrystalline $Fe_{60}Al_{40}$ (at. %) sheets of around 200 μm thickness, prepared by repeated cold rolling and annealing, have been employed [14]. First, the sheets have been mechanically polished using diamond paste until mirror-like appearance and, then, annealed to 650 ºC for 30 min, under vacuum (air pressure < 10^{-5} mbar), in order to remove any magnetic contributions which might have been introduced during the preparation process. For the irradiations, a low-energy ion implanter has been used. The primary energy of the different ions (2 keV He^+, 11 keV Ne^+, 21 keV Ar^+, 35 keV Kr^+, 45 keV Xe^+) is adjusted to position the maximum of the collisional damage distribution at a depth of around 10 nm [28]. The ion fluence is varied to obtain approximately a damage within the top 30 nm in the range of 0.05 - 5 dpa.

The structure of the modified surface layer has been investigated by glancing incidence XRD. The microstructural parameters (crystallite sizes, microstrains, lattice parameters and atomic occupancies) have been evaluated by adjusting the patterns by means of the Rietveld refinement program MAUD. The magnetic characterization has been performed by MOKE magnetometry.

Furthermore, to study the recovery of the effects caused by irradiation, high fluence He^+ ($3.5 \cdot 10^{15}$ ions/cm^2, 2 keV) and Xe^+ ($6 \cdot 10^{13}$ ions/cm^2, 45 keV) irradiated samples have

been annealed in high vacuum ($p_{air} < 10^{-7}$ mbar). The temperature has been cycled with rise and fall times of 20 °C/min and 5 min at the specified temperature.

3.1.B.1.2. Magnetic and structural characterization

In Figure 3.9, the hysteresis loops after 45 keV Xe^+ irradiation for different fluences and, thereby, damage levels are shown.

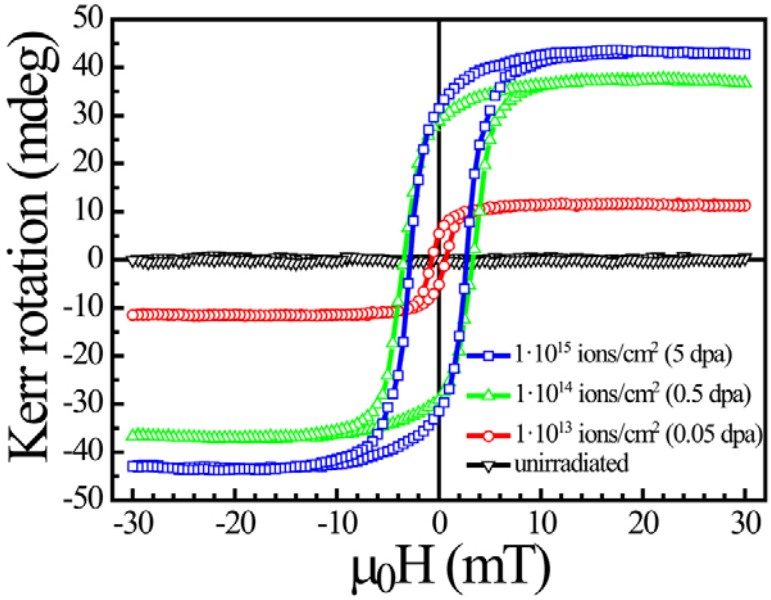

***Figure 3.9**. Hysteresis loops investigated by means of magneto-optic Kerr effect of an $Fe_{60}Al_{40}$ alloy, before and after being irradiated with three different fluences of 45 keV Xe^+. In addition, the damage is specified in each case.*

As expected, prior to ion irradiation, no ferromagnetic behavior is detectable. Interestingly, a rather low Xe^+ fluence of 10^{13} ions/cm^2 already leads to a substantial ferromagnetic signal with the hysteresis loop exhibiting a coercivity of 0.7 mT. The transformation to the ferromagnetic state in the near-surface region saturates at a damage level well above 0.5 dpa. At 45 keV Xe^+, the sputter yield is around 7.5 atoms/ion, thus the irradiation induced erosion is below 0.1 monolayer at such low fluence (i.e., 10^{13} ions/cm^2). For 0.5 dpa, the coercivity increases up to 3.5 mT, and the squareness improves to M_R/M_S = 0.75 (where M_R and M_S are the remanent magnetization and the saturation magnetization, respectively). At this fluence, the sputtering is still less than 1 monolayer. No significant in-plane anisotropy could be

detected by measuring the hysteresis curves as a function of in-plane angle of measurement, in agreement with the random orientation of the grains in the sheet. Increasing the average damage to 5 dpa results only in a slight reduction in coercivity and squareness. Subsequent annealing of the sample to 650 ºC for 30 minutes completely restores the initial paramagnetic state.

In order to further quantify the evolution of the ferromagnetic phase, the amplitude of the MOKE signal (the total Kerr rotation at saturation), which is a measure of the magnetic moment, is shown in Figure 3.10 (a) as a function of the fluence of the different ions (note the logarithmic scale).

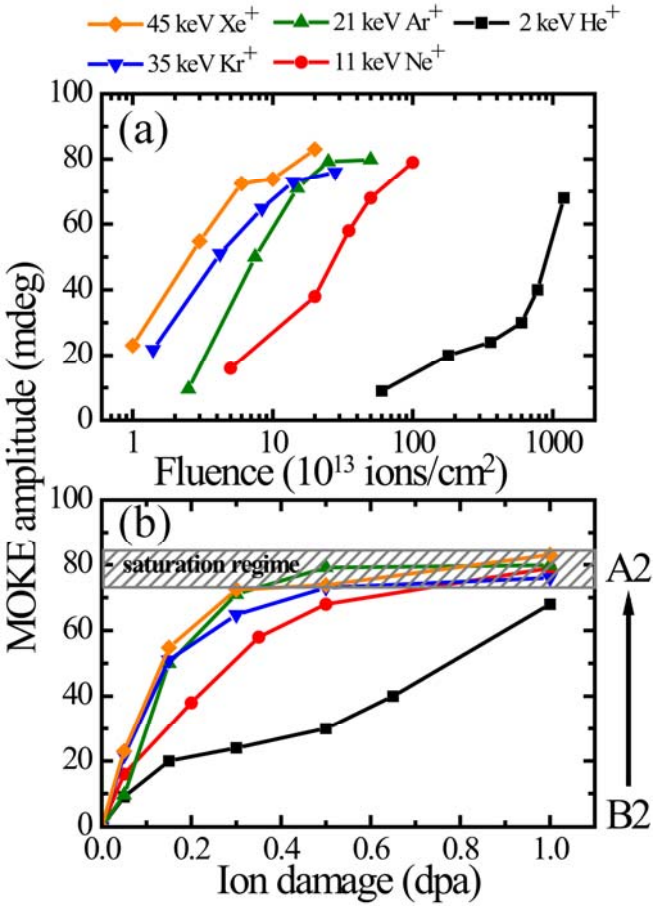

***Figure 3.10**. Magneto-optic Kerr effect (MOKE) amplitude as a function of ion fluence (a) and as a function of ion damage (b) for five different ion species (He^+, Ne^+, Ar^+, Kr^+, Xe^+). The primary energy is adjusted to achieve the maximum number of displacements per atom at 10 nm depth from the surface of the $Fe_{60}Al_{40}$ sheets.*

At lower ion mass, a larger ion fluence is required to obtain the same magnetic moment. For example, to obtain the same MOKE amplitude, the irradiation fluence for He^+ is about 3 orders of magnitude larger than for Xe^+.

Shown in Figure 3.11 are the hysteresis measurements after annealing steps of a sample irradiated using 2 keV He^+ with a fluence of $3.5 \cdot 10^{15}$ ions/cm^2. Note that the coercivity decreases as the annealing temperature increases, evidencing the concomitant structural recovery induced by the thermal treatment, which results in less pinning sites for magnetization reversal.

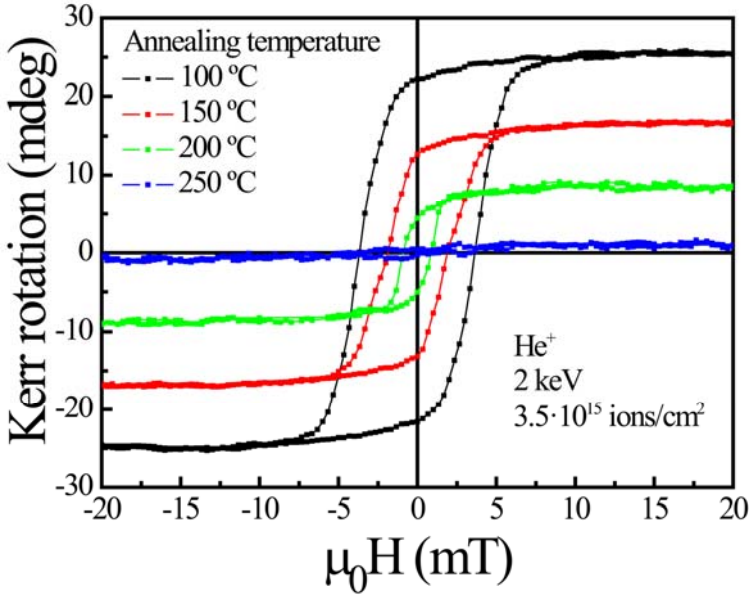

Figure 3.11. *Hysteresis loops recorded by magneto-optic Kerr effect (MOKE) after annealing procedures at different temperatures for the sample irradiated using 2 keV He^+ with a fluence of $3.5 \cdot 10^{15}$ ions/cm^2.*

If the MOKE amplitude is plotted versus damage –see Figure 3.10 (b)–, the data spread is considerably reduced, and a universal behavior is observed for the heavy ion species Ar^+, Kr^+ and Xe^+. As above, at about 0.5 dpa, the saturation regime of the ferromagnetic behavior is reached, which indicates that the phase transformation to the disordered A2-phase in the near-surface region due to ballistic mixing processes is completed. However, for lighter ions, a distinct deviation from this universal curve is observed, i.e. a significantly larger nominal damage is required to induce the transition. This can be explained by the different topologies of the collision cascades associated with different

ion masses, which can be visualized by TRIM computer simulation [28]. Light ions tend to create dilute vacancy-interstitial pairs along the ion track, which are essentially all available for diffusion into the surrounding matrix, with the mobile vacancies leading to chemical reordering in the environment. On the other hand, heavy ions develop sequences of spatially dense collision subcascades, with a high probability of dynamic annealing within the subcascades [29]. Thus, at equal nominal damage, less mobile vacancies will be available and, consequently, less reordering will occur in comparison to light ions. Furthermore, the dense subcascades, which are generated preferentially by heavier ions, may result in local regions where the chemical order is lost, in analogy to amorphous pockets found in semiconductors [30,31]. These regions might be more resistant to reordering than the isolated defects which are preferentially created during light ion irradiation. Hence, while ballistic mixing arguments satisfactorily explain heavy ion irradiation effects, a dynamic recovery of thermodynamically stable phases has always to be considered for light ion irradiation.

In order to further support the above interpretation, glancing incidence X-ray diffraction (GIXRD) has been used to investigate the virgin sample and two irradiated samples (He^+ and Xe^+) with a similar damage level (0.2 ($3.5 \cdot 10^{15}$) and 0.3 dpa ($6 \cdot 10^{13}$ ions/cm^2), respectively). In this range, the difference in magnetic signal is maximal. Note that the GIXRD signal is always a superposition of the modified top 20 nm and the unaffected bulk beneath. However, analyzing the GIXRD data (see Figure 3.12) leads to the parameters given in Table 3.2.

At similar damage levels, Xe^+ irradiation, in comparison to He^+ irradiation, leads to a stronger reduction in long-range order parameter LRO and a slight increase in lattice spacing *a*. Since both are required in order to achieve ferromagnetic order, this is consistent with the stronger ferromagnetic signal for Xe^+ irradiation.

A remarkable analogy is found if ion irradiation induced amorphization of metallic alloys is considered [32]. In these investigations the resistivity which is a measure of the amorphized fraction exhibits a similar course as a function of ion fluence and also displays a distinct difference if light or heavy ions are used. This proves that the concept

of the collision cascade topology can be applied in a wider range of experiments to explain various ion irradiation induced phenomena.

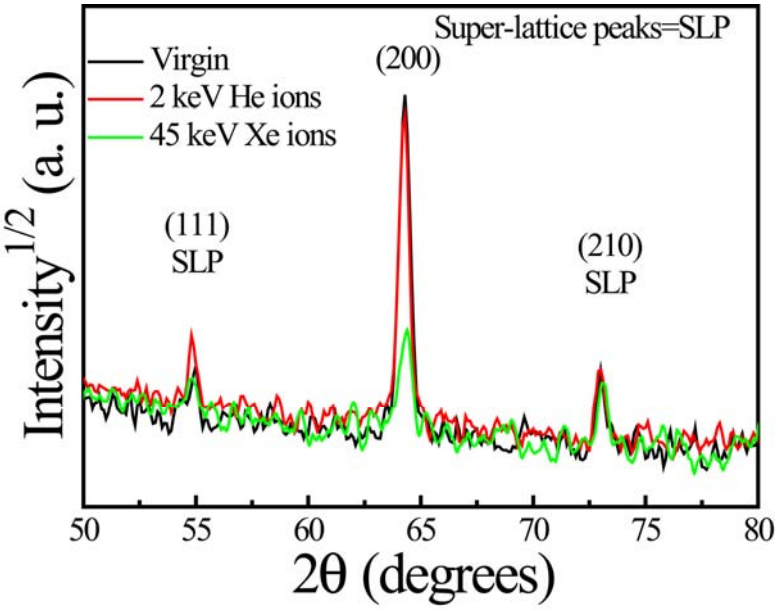

Figure 3.12. *Glancing incidence X-ray diffraction (GIXRD) patterns of the $Fe_{60}Al_{40}$ (at. %) alloy after being annealed (i.e., virgin) and homogeneously irradiated using either He^+ (2 keV, 0.2 dpa) or Xe^+ (45 keV, 0.3 dpa). The Miller indexes of the $Fe_{60}Al_{40}$ (at. %) alloy are also indicated in the figure. Note that SPL denotes the super-lattice peaks.*

$Fe_{60}Al_{40}$ (at. %)	Virgin	He^+	Xe^+
Damage (dpa)	0	0.2	0.3
Long-range order parameter LRO	0.66	0.52	0.34
Lattice spacing *a* (Å)	2.8977	2.8985	2.8995
MOKE amplitude (mdeg)	0	23	73

Table 3.2. *Summary of parameters determined from fitting the glancing incidence X-ray diffraction patterns and magneto-optic Kerr effect for the virgin as well as the He^+ or Xe^+ irradiated samples –(2 keV, 0.2 dpa) and Xe^+ (45 keV, 0.3 dpa), respectively–.*

3.1.B.2. Micro and nanoscaled approaches: lithography through shadow masks

3.1.B.2.1. Broad beam irradiation through TEM grids

Here, it is demonstrated that micro-patterning can be achieved by homogeneous ion irradiation through a transmission electron microscope (TEM) grid, acting as shadow mask, fixed at the surface of a $Fe_{60}Al_{40}$ sheet. As a result, ferromagnetic structures over large areas have been generated by means of this technique.

3.1.B.2.1.1. Experimental details

For a proof of principle, a patterning experiment using a 2000 mesh grid (with a mesh size of 7.5 x 7.5 μm^2, 12.5 μm pitch and 20 μm thickness) has been carried out. The irradiation process has been performed using Xe ions, accelerated at 45 kV, and a fluence of $2 \cdot 10^{14}$ ions/cm^2. The produced magnetic entities have been characterized by both MOKE magnetometry and MFM.

3.1.B.2.1.2. Magnetic patterning

The parallel generation of ferromagnetic arrays over large areas (in the order of mm^2) by means of this technique has been demonstrated. For this purpose, broad beam irradiation through a grid used as a mask has been performed. In Figure 3.13 (a), an atomic force microscopy image of the $Fe_{60}Al_{40}$ sheet is shown. Interestingly, no change in topography is observed between the irradiated and non-irradiated areas.

Figures 3.13 (b) - (d) are the corresponding MFM images acquired in different applied in-plane magnetic fields. If an in-plane magnetic field of ± 40 mT is applied, which is sufficient to saturate the magnetization (see Figure 3.9), there are single-domain ferromagnetic regions as can be nicely observed by the stray field contrast at the boundaries of the embedded magnets. The magnetic origin of the contrast is proven by the stray field reversal upon magnetic field switching –see Figures 3.13 (c) and (d)–. If

no magnetic field is applied, the single domain state decomposes into multi-domain states –Figure 3.13 (b), which has been taken after recording the panel (d)–. However, some remanent magnetization remains, which is consistent with the hysteresis loops shown in Figure 3.9. In order to achieve a single domain behavior also in the remanent state, the ferromagnetic features may be shrunk in size.

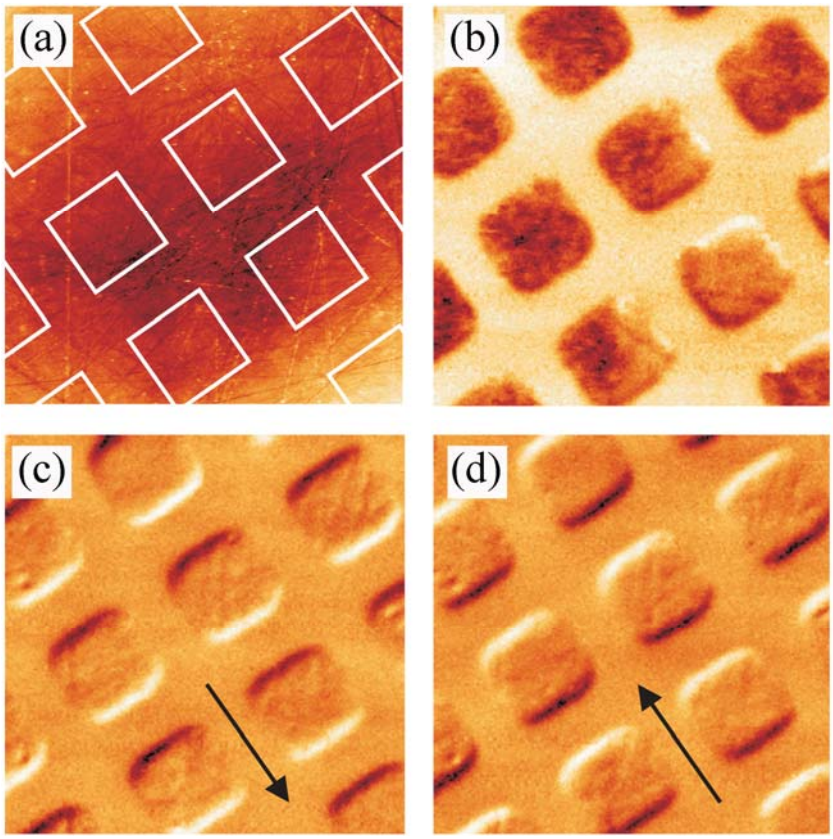

***Figure 3.13**. Atomic force microscopy (a) and magnetic force microscopy (MFM) (b)-(d) images of the $Fe_{60}Al_{40}$ sheet after the Xe^{+} irradiation. The squares in (a) indicate the 7.5 × 7.5 μm^2 regions which have been irradiated. For the series of MFM images, different magnetic fields have been applied: (b) 0 mT, (c) -40 mT, (d) 40 mT. The arrows in (c) and (d) indicate the direction of the applied magnetic field.*

In addition, it is noteworthy to mention that there is almost no difference between the MOKE loops of the homogeneously irradiated area and the patterned material since the induced ferromagnetic structures are relatively large (micrometer range), leading to entities with magnetic multidomain configurations.

3.1.B.2.2. Broad beam irradiation through alumina masks

Arrays of circular-shaped magnetic entities with in-plane magnetization have been prepared, in a single step, using an aluminum oxide membrane, with self-organized and ordered arrays of holes in the nanometer range, as a shadow mask on a $Fe_{60}Al_{40}$ sheet. Large arrays can be obtained depending on the dimensions of the employed alumina template. It should be noted that these membranes have been prepared by anodization processes at the Max Planck Institute of Microstructure Physics (Halle, Germany) in collaboration with Professor K. Nielsch's group.

3.1.B.2.2.1. Experimental details

Ion irradiation has been carried out using 40 keV Xe ions with a fluence of $1 \cdot 10^{15}$ ions/cm^2 (5 dpa) through pseudo-ordered alumina membranes (see Figure 3.14) of 5 μm of thickness.

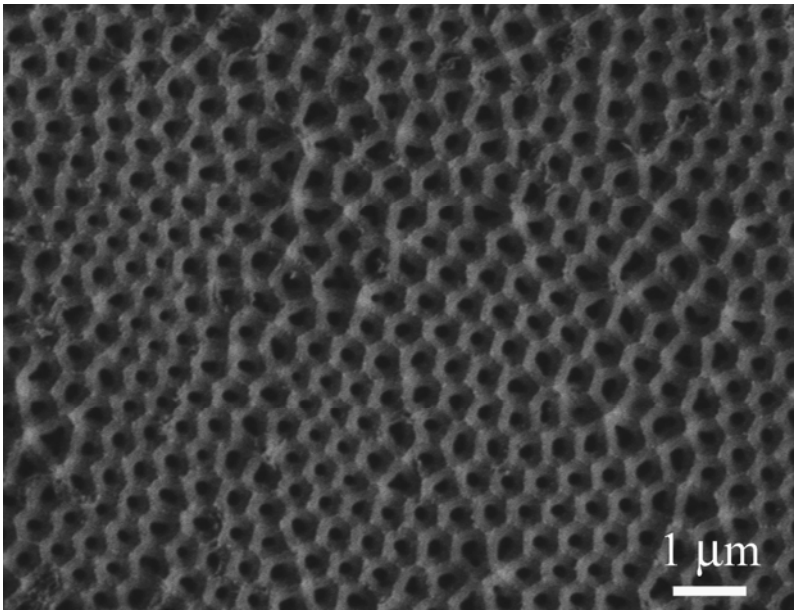

Figure 3.14. *Scanning electron microscopy image, obtained using secondary electrons, of an employed alumina template.*

3.1.B.2.2.2. Magnetic patterning

Shown in Figure 3.15 (a) is the magnetic force microscopy image, taken in an applied magnetic field of 50 mT, of a hexagonal array of circular dots (300 nm in diameter approximately), which reveals the dipolar contrast in each entity. As it can be seen in panel (b), the corresponding hysteresis loop shows a central constriction, evidencing that magnetization reversal occurs via formation of a vortex state [27].

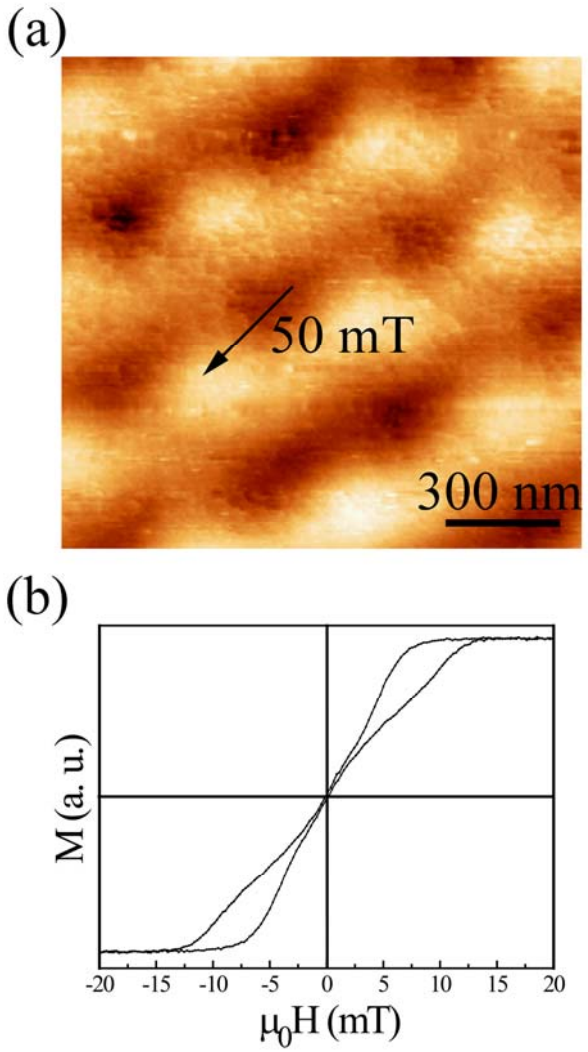

Figure 3.15. *(a) Magnetic force microscopy image (obtained applying a field of 50 mT) of a pseudo-ordered array of magnetic dots obtained by ion irradiation of a paramagnetic $Fe_{60}Al_{40}$ sheet through an alumina membrane; (b) corresponding magneto-optic Kerr effect hysteresis loop, typical of magnetization reversal via formation of a vortex state.*

3.1.B.2.3. Broad beam irradiation through electron beam lithographed specimens

Arrays of ferromagnetic structures embedded in a non-magnetic matrix (i.e., paramagnetic), with sizes in the range 100 - 400 nm, have been controllably fabricated by means of broad beam Xe^+ ion irradiation through lithographically defined masks, designed on $Fe_{60}Al_{40}$ (at. %) sheets.

3.1.B.2.3.1. Experimental details

In order to generate periodic arrays of magnetic structures, shadow masks have been produced by electron beam lithography, generating patterns in both a 90 nm and 70 nm thick polymethylmethacrylate (PMMA) resist layers coated on the $Fe_{60}Al_{40}$ sheets. 50 × 50 μm^2 areas containing different types of dots have been designed on the PMMA (circular with a 100 - 1000 nm diameter, square with a 300 nm edge, rectangles with dimensions 100 × 300 nm^2 to 300 × 900 nm^2 and lines of 100 - 300 nm width).

Ion irradiation has been carried out using Xe ions, accelerated at 40 kV, with a fluence of $1 \cdot 10^{15}$ Xe ions/cm^2 (≈ 5 dpa) for the samples with a 90 nm thick PMMA layer on the top and accelerated at 25 kV, with a fluence of $2 \cdot 10^{14}$ ions/cm^2 (≈ 1 dpa), for those with a 70 nm PMMA layer. Subsequently, the polymeric resist is removed using trichloroethylene.

The topography of the samples has been examined by AFM. The hysteresis loops of the irradiated areas have been measured using a MOKE setup capable of focusing the laser beam down to 3 μm. MFM imaging has been carried out in fields up to 75 mT using high sensitivity hard magnetic tips.

3.1.B.2.3.2. Magnetic patterning

To demonstrate the viability of patterning all magnetic nanostructures simultaneously in a fast parallel process, the $Fe_{60}Al_{40}$ sheets have been irradiated through 90 nm thick PMMA masks patterned with a series of holes produced by electron beam lithography.

The polymer resist thickness has been calculated [28] to stop the incoming ions before reaching the metallic sheet, thus preventing the matrix (i.e., the areas covered by the PMMA) from becoming magnetic (see Figures 3.16 and 3.17).

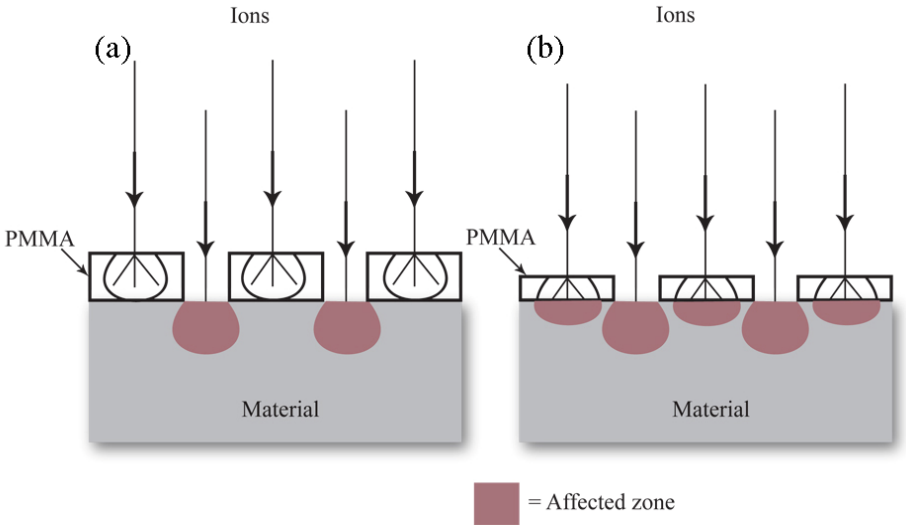

***Figure 3.16**. Schematic diagram showing contrary cases (a) when the polymer resist is thick enough to stop the incoming ions and (b) when it is not. Panel (a) allows obtaining a magnetic patterned medium but, in contrast, panel (b) leads the whole surface to become ferromagnetic.*

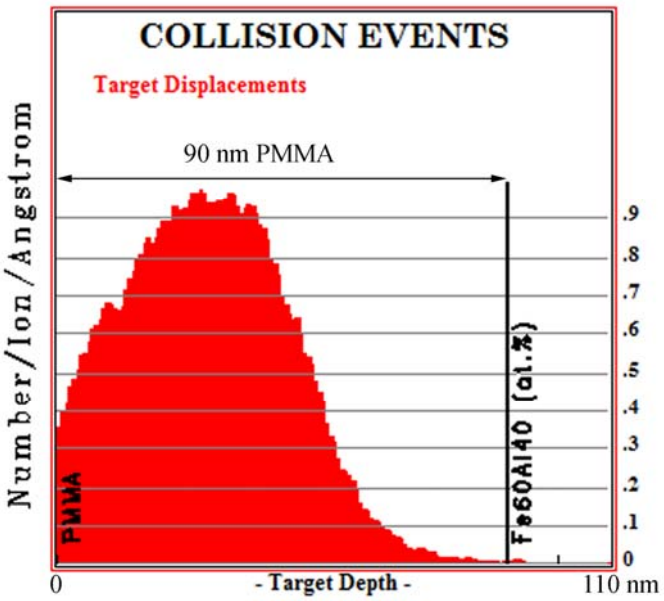

***Figure 3.17**. TRIM simulation showing that a 90 nm PMMA layer is thick enough to stop the incoming Xe ions accelerated at 40 kV.*

Note that although Xe^+, accelerated at 40 kV, with a fluence of $1 \cdot 10^{15}$ ions/cm^2 (equivalent to 5 dpa) have been used for most experiments, much smaller fluences (down to $1 \cdot 10^{13}$ ions/cm^2 –i.e., 0.05 dpa–) can be used to induce magnetism in $Fe_{60}Al_{40}$.

As shown in Figure 3.18 (a), magnetic imprinting is confirmed by MFM imaging of the square-shaped dots.

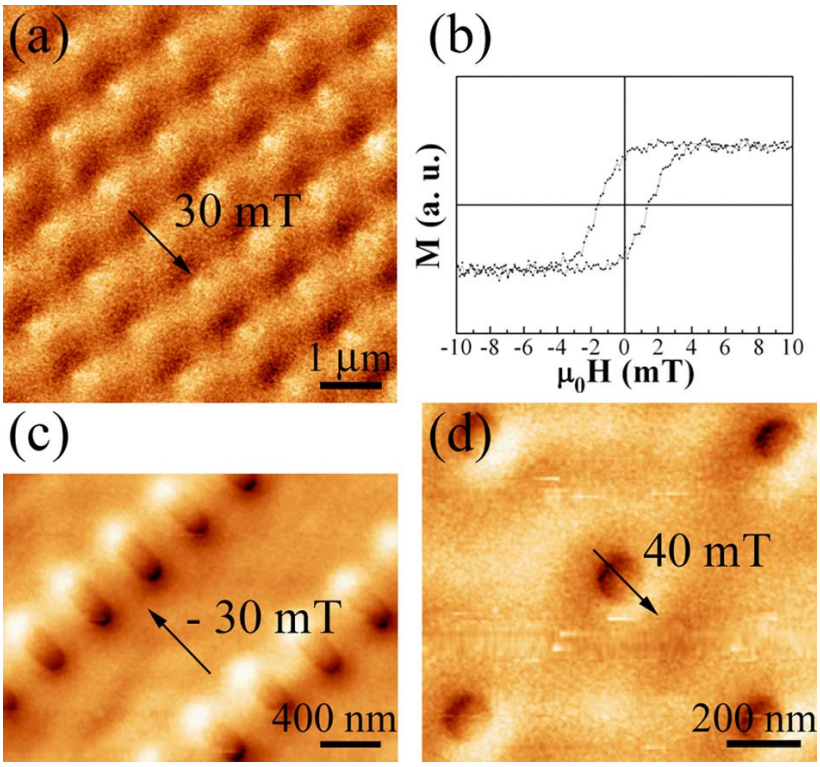

Figure 3.18. *Magnetic patterning of different types of geometries using lithographed masks. (a) Magnetic force microscopy (MFM) image of an array of 300 nm^2 square-shaped dots, irradiated through a lithographed PMMA mask, in an external magnetic field of 30 mT with (b) the corresponding magneto-optic Kerr effect hysteresis loop. (c,d) MFM images of different patterned areas ((c) rectangles –100 × 300 nm^2– and (d) circular-shaped dots –100 nm–) irradiated using a lithographed PMMA mask. The images were recorded in -30 mT and 40 mT magnetic fields, respectively.*

The overall magnetization of the array of square dots (around 300 nm of lateral dimension) –Figure 3.18 (a)–, obtained by MOKE, is shown in Figure 3.18 (b). This particular type of array exhibits a hysteresis loop with a squareness close to 1. All different types of arrays created on the $Fe_{60}Al_{40}$ sheet (down to the smallest one of about 100 nm in diameter) show ferromagnetic behavior and, as can be seen in Figures 3.18 (c) and (d), the various morphologies of the nanostructures exhibit different magnetic

behavior. For example, while the rectangular dots and lines present a strong uniaxial (shape) anisotropy, square dots have virtually no shape anisotropy and some larger circular dots show vortex behavior.

Furthermore, arrays of circular holes with different sizes (interdot distance of 1 μm) have been also prepared by electron beam lithography on a 70 nm thick PMMA. The energy to irradiate the samples is reduced in order to avoid the penetration of ions in the non-lithographed parts. Namely, a lower fluence of $2 \cdot 10^{14}$ ions/cm^2 (≈ 1 dpa) is utilized in order to be in the safe side and avoid making the whole surface become ferromagnetic. Shown in Figure 3.19 are the MOKE hysteresis loops of the arrays containing circular dots with average diameters of 410 and 215 nm –panels (a) and (b), respectively–.

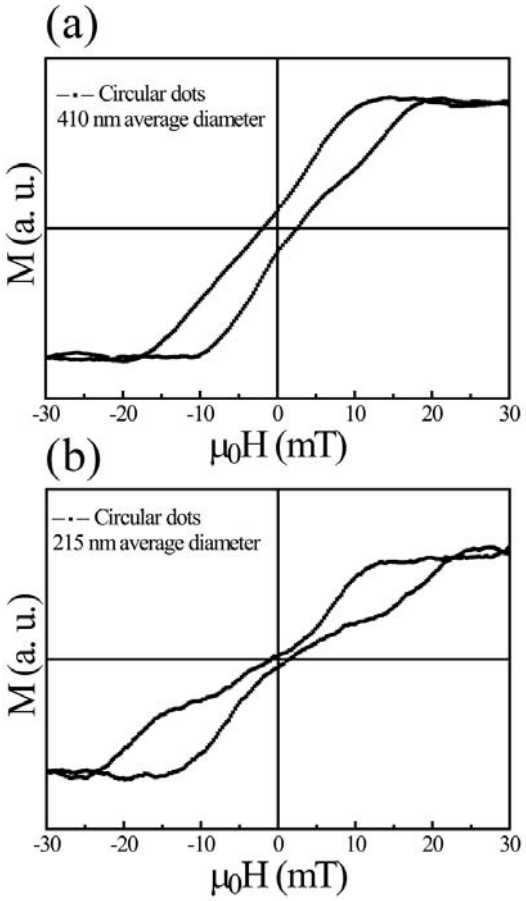

Figure 3.19. *Magneto-optic Kerr effect measurements of arrays of 410 and 215 nm diameter circular-shaped dots –panels (a) and (b)–, respectively, irradiated through a lithographed PMMA mask. Note that the interdot distance is around 1 μm in both arrays.*

Interestingly, even though the current irradiation conditions are different from those performed in section 3.1.B.2.2., vortex states are also obtained in this approach. As it can be seen in Figure 3.19, the corresponding hysteresis loops show a central constriction, which is more pronounced in panel (b), since the structures are smaller, evidencing that magnetization reversal occurs via formation of a vortex state. Actually, all different types of magnetic response are the ones expected from the diverse sizes and shapes of the nanostructures [22,27].

For industrial purposes, nanoimprint lithography (NIL) could be employed to speed up the patterning process [33,34] using, e.g., electron beam lithography to create the NIL master. Moreover, the results (especially the sizes) shown here are intended only as a proof of principle and even smaller sub-20 nm masks can be ultimately obtained from both electron beam lithography and nanoimprint [33,35].

Finally, it is worth mentioning that the "magnetic" patterning of metallic alloys ($Fe_{60}Al_{40}$ alloys) by nanoindentation (see section 2.3.6.) [36] suffers from some drawbacks compared to ion irradiation. Specifically, the surface topography created by the indentation, which is minimized using the irradiation approach, may be detrimental for certain applications. Moreover, using conventional nanoindentation, simultaneous processing of large arrays would be a challenge, especially in the sub-100 nm regime. In addition, plastic deformation effects (i.e., topographic) would remain even after high temperature annealing (which removes the magnetic patterning). In contrast, the current irradiation processes through either TEM grids or alumina membranes are parallel processes which allow producing large patterned areas (of the order of mm) in a few minutes according to the employed fluences. Nevertheless, although by irradiation through lithographed masks it is also feasible to fabricate several magnetic dots at once, it becomes ultimately a serial process since the mask is fabricated using electron beam lithography, which is a serial technique.

3.1.B.2.4. Local irradiation by focused ion beam

Sub-100 nm magnetic dots, embedded in a non-magnetic matrix, have been also controllably generated by selective ion irradiation of paramagnetic $Fe_{60}Al_{40}$ (at. %) sheets via sequential (i.e., serial) focused ion beam (FIB) procedures.

3.1.B.2.4.1. Experimental details

In order to generate periodic arrays of magnetic structures, areas of 50 × 50 μm^2 containing arrays of circular (40 nm in diameter) and rectangular nanostructures with shortest dimensions ranging from 50 to 350 nm and longest lateral sizes from 100 to 600 nm have been prepared by means of FIB using Ga ions in the fluence range of 1 - $5 \cdot 10^{15}$ ions/cm^2 (3 - 15 dpa) on $Fe_{60}Al_{40}$ sheets. The settings used for patterning have been 1 pA beam current at 30 keV which results in a beam diameter of nominally 8 nm. Nevertheless, after defocusing the beam to reduce the maximum fluence and thus the surface etching, an effective beam diameter of 32-50 nm has been used depending on the pattern size (e.g., the fluence and the effective beam diameter utilized to pattern the circular dots are $1 \cdot 10^{15}$ ions/cm^2 and around 32 nm, respectively). Note that the shape of the dots is not exactly the one in the FIB designs (i.e., rectangular structures become somewhat rounded at the edges –see Figure 3.20– and circular dots become elliptical-shaped –see Figure 3.21 (a)–). This phenomenon may be ascribed to the defocusing process of the beam, in combination with a slight misalignment of the lenses from the axis and some remaining astigmatism when producing the smallest structures. Limitations of the beam control in the FIB process make it necessary to use a relatively large round spot to write the structures, leading to non-rectangular spatial confinement of the edges in the case of the rectangular entities and an effectively elliptical appearance for the smallest ones.

The topography of the samples has been examined by AFM. SEM imaging, with a secondary electron detector, has been used for element mapping in the case of FIB irradiated samples, since the secondary electrons are sensitive to the composition given the difference in work function between Fe or Al and Ga.

The hysteresis loops of the irradiated areas have been measured using MOKE magnetometry. MFM imaging has been carried out in fields up to 75 mT using high sensitivity hard magnetic tips.

3.1.B.2.4.2. Magnetic patterning

To determine whether it is possible to generate sub-100 nm structures by ion irradiation, FIB irradiation of $Fe_{60}Al_{40}$ sheets has been carried out. Similar to broad beam ion irradiation, in FIB, the irradiation produces collision cascades between Ga^+ and Fe and Al atoms of the alloy. However, in this case the beam is confined to a few tens of nm. Figure 3.20 (a) shows the AFM image together with the corresponding MFM image – Figure 3.20 (b)– for the 350 × 500 nm^2 rectangular patterns.

The local character of the induced magnetism is evidenced by the MFM measurements, where the dipolar contrast is clearly observed in each structure. In this case, the topography of the sample also remains featureless and the smooth surface is preserved. Note that the topography observed in the AFM image is only due to the polishing process used for the sample preparation, which results in an average height of 10.1 nm and a root-mean-square (rms) roughness of 2.8 nm, with standard deviations of 1.6 and 0.5 nm, respectively. Interestingly, the ion-induced sputtering (i.e., erosion) results in virtually no changes in either the average height or the rms roughness (i.e., below the statistical deviation). Due to the Ga incorporation during the irradiation process, the patterned structures can be easily visualized by scanning electron microscopy, using secondary electrons, as shown in Figure 3.20 (c). Furthermore, it has been reported that the induced ferromagnetic state in FeAl alloys can be stabilized when Al is substituted by Ga [37]. The overall magnetic properties of the arrays have also been investigated with MOKE measurements. The laser spot of the MOKE system was either focused down to 3 μm diameter (only a few structures measured) or defocused to include the whole array. Analysis of different parts of the same array or defocused measurements rendered virtually identical hysteresis loops (e.g., all the H_C values were within 10 %), attesting a rather good homogeneity in the magnetic behavior of the generated structures. Moreover, as can be seen in Figure 3.20 (d), the magnetic measurements

revealed that the patterned rectangles exhibit in-plane shape anisotropy with the long side of the rectangle being the easy axis, as expected from their shape. Finally, MOKE measurements on neighboring non-irradiated areas show that they remain paramagnetic.

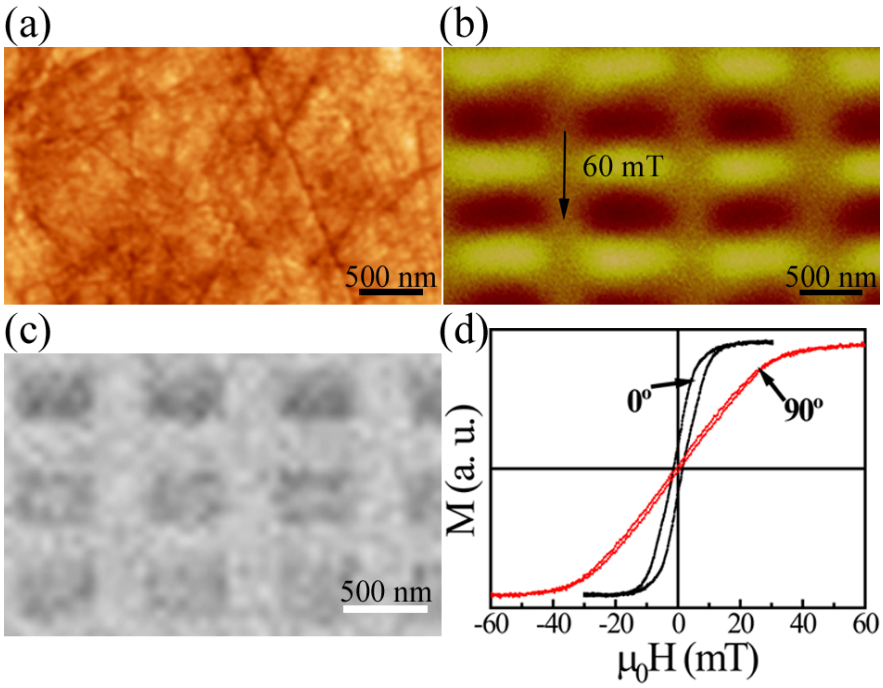

Figure 3.20. *(a) Local magnetic patterning using focused ion beam (FIB) exhibiting no topographic features. Atomic force microscopy image of an array of 350 × 500 nm^2 rectangles prepared by means of FIB with (b) the corresponding magnetic force microscopy image in an external magnetic field of 60 mT applied along the shortest dimension of the rectangles. (c) Scanning electron microscopy image of the patterned area measured with a secondary electron detector. (d) Magneto-optic Kerr effect hysteresis loops recorded with the magnetic field applied along the longest side of the rectangles (0º) and along the shortest side (90º).*

As can be seen in Figure 3.21 (a), the SEM imaging indicates that structures as small as 40 nm in diameter can be generated by FIB. As discussed in the experimental details section, the unusual shape of the dots stems from the defocusing of the FIB beam, required to reduce the fluence, in order to avoid induced surface roughness.

The magnetic imaging –Figures 3.21 (b) and (c)– clearly evidences that sub-100 nm magnetic features are achieved. However, it is worth mentioning that for the sub-100 nm dots, the MFM features appear rather larger than the physical size of the dots –compare Figures 3.21 (a) and (b)–. This is due to the convolution between the stray fields of the dots and the MFM tip (with a radius of curvature of < 50 nm). However,

even though the MFM features appear clearly larger than the physical size of the related structures, it is worth noting that the magnetic size, obtained from MFM characterization, has to be estimated from the distance between adjacent minimums (valleys) and maximums (peaks) in the phase line profile analysis [38]. For the circular dots, an average value of 90 with a standard deviation of 10 nm is obtained between the respective centers of the dark (valley) and bright (peak) areas of the MFM images (50 structures are measured), taken in an applied magnetic field of 30 mT –see Figure 3.21 (c)–. In addition, since MFM detects the stray fields at a certain distance from the surface of the specimen and due to the concomitant convolution of the stray fields of the tip and the dot, 90 nm have to be taken as an upper limit (i.e., the structures should certainly be smaller).

Importantly, concerning the overall properties of the arrays, when comparing the MOKE results in Figures 3.20 and 3.21, it can be clearly observed that the smallest dots exhibit much larger coercivities, in excess of $\mu_0 H_C$ = 50 mT –Figure 3.21 (d)–. Moreover, the loops are characterized by a high squareness, $M_R/M_S = 1$ (where M_R and M_S are the remnant and saturation magnetizations, respectively). It should be noted that both the pronounced coercivity enhancement and high squareness are typical features of single-domain states [22,27]. Indeed, even though present-day magnetic recording media have coercivities of around 300 mT [22] the obtained coercivity may allow recording information in patterned media without requiring exceedingly powerful and bulky writing heads [39]. In addition, the high squareness constitutes a crucial requirement in order to assure the proper storage of information [22,39].

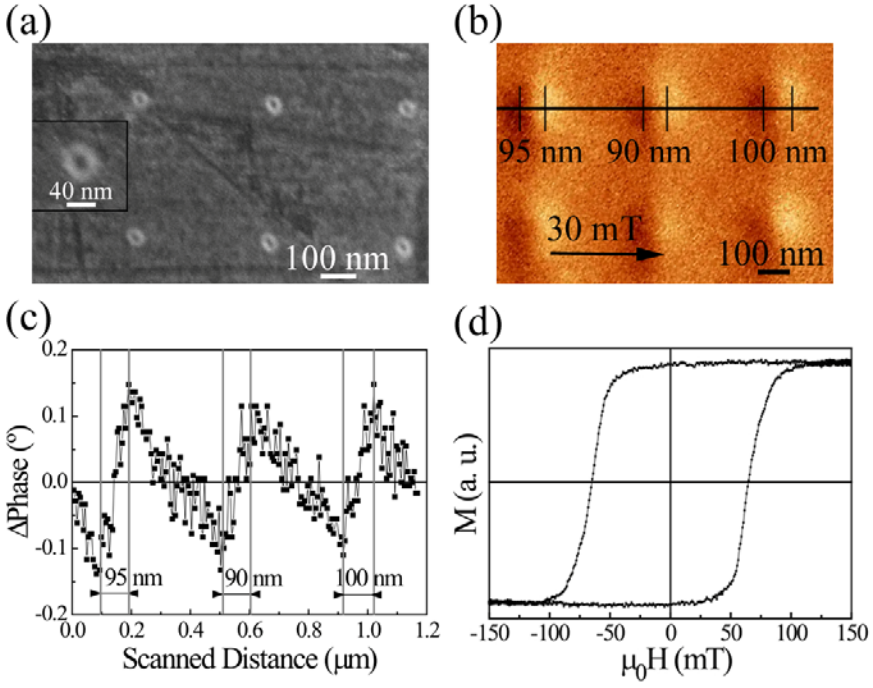

Figure 3.21. *Sub-100 nm magnetic patterning by focused ion beam (FIB). (a) Scanning electron microscopy image obtained using secondary electrons of an array of circular dots, 40 nm in diameter, patterned by FIB. The inset in (a) shows an enlarged image of one of these entities. (b) Magnetic force microscopy image of the circular dots taken in $\mu_0 H$ = 30 mT after saturation; (c) Phase line profile scan analysis at the position indicated in (b) and (d) magneto-optic Kerr effect hysteresis loop corresponding to these ferromagnetic features.*

It is important to point out that FIB is still a relatively slow sequential technique (in-series) where each nanostructure is irradiated individually. Hence, FIB is not adequate for mass production of nanostructures.

Concerning the above sections about lithography through shadow masks and FIB, it is worth mentioning that, ignoring technical issues, the size of the magnetic structures produced by these magnetic patterning methods is intrinsically limited by the ion-target interactions (i.e., by the irradiation process itself). Since the ion does not penetrate in the material following a straight path due to collisions with target atoms, a lateral distribution of damage is defined. For instance, note that, according to TRIM simulations [28], the lateral distribution of damage for the 40 keV Xe^+ and 30 keV Ga^+ irradiations are roughly 3 and 4.5 nm, respectively. In fact, twice these values would give the ultimate resolution of these cases.

3.2. Austenitic stainless steels

3.2.A. Ferromagnetism induced by mechanical deformation

3.2.A.1. Macroscopic approach: ball milling and compression tests

It is well known that due to strain-induced deformation, a phase transformation from the face-centered cubic –FCC– austenite (γ), which is paramagnetic at room temperature, to a body-centered cubic –BCC– martensite (α') phase –ferromagnetic– can occur in these ferrous alloys [40-42]. Even though the extent of $\gamma \rightarrow \alpha'$ transformation depends mainly on the chemical composition of the steel and the temperature at which the plastic deformation takes place, other important factors affecting this strain-induced phase transformation are the strain rate, grain size and deformation mode (i.e., stress state) [43]. Interestingly, the high rate deformation response of ASSs is known to be different from the quasi-static behavior [44].

The strain-induced austenite (γ) to martensite (α') transformation in AISI 316L austenitic stainless steel, either in powders or bulk specimens, has been investigated. The phase transformation is accomplished by means of either ball milling processes (in powders) –dynamic approach– or by uniaxial compression tests (in bulk specimens) –quasi-static approach–. Namely, the $\gamma \rightarrow \alpha'$ phase transformation and the development of magnetism (and enhanced hardness in bulk samples) have been correlated.

3.2.A.1.1. Experimental details

The as-received AISI 316L powders (Alfa Aesar, -325 mesh) consist of a mixture of γ and α' phases, where the presence of the metastable martensite phase could be ascribed to the gas atomization process used to synthesize the starting powders. The as-received powders have been subjected to an annealing process up to 800 ºC (temperature which is enough to allow the reverse, martensite-to-austenite, phase transformation in powder-form samples), under vacuum –air pressure < 10^{-5} mbar–, during 90 minutes to remove

any traces of the ferromagnetic α′ phase. Subsequently, the as-annealed powders have been ball-milled (BM) during 0.5, 1, 5, 10, 15, 20 and 30 h in a planetary ball mill, under Ar atmosphere, using hardened stainless steel vials and balls and a ball-to-powder mass ratio of 3:1. Disk angular frequencies of either 326 or 460 rpm (equal to the vial frequency in each case) have been used, which lead to different milling intensities –processes performed at 326 and 460 rpm will be denoted in the main text as I1 and I2, respectively–.

The morphology of the BM powdered specimens has been examined by means of SEM.

Regarding the bulk specimens, cubic-shaped samples (8 mm^3 volume) have been cut from commercial AISI 316L ASS polycrystalline bars and polished up to mirror-like appearance. The samples have been subsequently annealed for 30 min at 1100 ºC (temperature which is above the reverse, martensite-to-austenite, phase transformation temperature), under vacuum –air pressure < 10^{-5} mbar–, to eliminate the magnetic contributions which arise from the polishing-induced α′ phase. The compression processes have been performed uniaxially at room temperature. Two different loading rates (i.e., 0.1 and 1 kN/s) and a dwell time of 100 s have been used after achieving the target engineering stress (i.e., 1.2, 3.2, 4.7 and 6.2 GPa).

The overall microstructural parameters in both approaches, such as phase percentages, crystallite sizes and microstrains, have been evaluated by fitting the full XRD patterns by means of the Rietveld refinement program MAUD. This software also includes a formalism to quantitatively evaluate stacking fault (SF) probabilities, thus allowing an accurate assessment of these planar defects, which are particularly important in the case of ASSs, since they are low-energy stacking fault alloys.

The Vickers microhardness of the bulk samples has been determined using a load of 1 kg, H_{V1}, and a holding time of 5 s.

Finally, the magnetic characterization has been performed by means of VSM. The saturation magnetization has been calculated from a least square fitting of the initial

magnetization curves to the classical law of approach to saturation (Eq. 3.1) after subtracting the paramagnetic contribution [2].

3.2.A.1.2. Ball milling of AISI 316L powders (dynamic approach)

3.2.A.1.2.1. Structural and morphological characterization

The XRD patterns of the powders ball-milled during 0.5, 10 and 30 h, at either I1 (326 rpm) or I2 (460 rpm) angular frequencies, are presented in Figure 3.22.

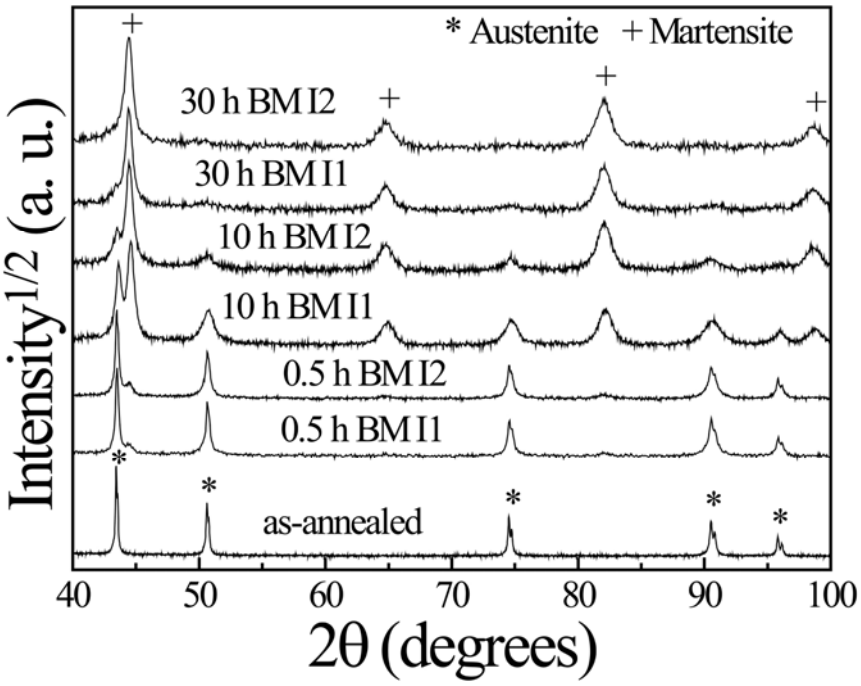

***Figure 3.22**. X-ray diffraction patterns of as-annealed ASS powders and specimens ball-milled during 0.5, 10 and 30 h at disk angular frequencies of 326 (I1) and 460 rpm (I2). Indicated in the figure are the main XRD peaks corresponding to austenite (*) and martensite (+) phases.*

The XRD pattern of the as-annealed sample is consistent with a FCC lattice structure (i.e., austenite phase, γ). Conversely, for the ball-milled samples, XRD peaks corresponding to the martensite phase appear (see Figure 3.22) even for the mildest conditions (i.e., 0.5 h at I1). The amount of the α′ phase increases with the milling time as it is evidenced by the increase of intensity of the α′ XRD peaks in detriment to the γ ones.

After 30 h of milling at I2, almost no traces of austenite XRD peaks are observed, thus resulting in a single phase material (i.e., martensitic steel). Remarkably, as it can be seen in Figure 3.23, the amount of the induced α′-martensite (estimated by XRD) is larger for milling procedures carried out at 460 rpm (I2) than for those performed at 326 rpm (I1). Actually, whereas milling processes performed at I1 show a steady-state like behavior only for long-term milling (i.e., 20 and 30 h), 5 h milling at I2 already leads to a martensite mass fraction in excess of 80 % (i.e., the steady-state in this case is attained for short-term milling).

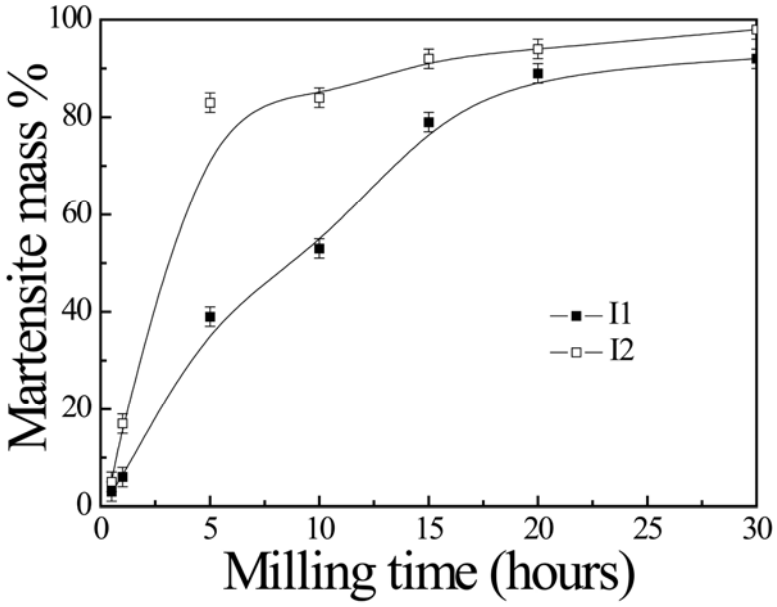

***Figure 3.23**. Milling time dependence of the strain-induced martensite mass % (estimated by x-ray diffraction) for the used milling intensities (I1=326 and I2=460 rpm). The lines are guides to the eye.*

Furthermore, a broadening of the XRD peaks corresponding to each phase is observed as the milling proceeds due to both crystallite size refinement and increase of microstrains (see Figure 3.22). Indeed, the milling processes result in smaller crystallites when increasing the milling intensity for either austenite or martensite phases (see Table 3.3). In addition, both the microstrains and the total amount of stacking faults corresponding to the austenite phase are larger for I2 procedures than those obtained from millings performed at I1. For milling times longer than 5 h, the austenite crystallite size remains rather constant with milling time either for I1 or I2 processes, even though a smaller crystallite size is obtained for I2 samples, confirming

that a more severe mechanical work occurs (see Table 3.3). Conversely, the crystallite size of the martensite phase tends to decrease even for long-term milling, while microstrain remains almost unaltered.

Concerning the morphological characterization, the thermal treatments to remove the ferromagnetic traces, ascribed to the powders production, lead to agglomerate-like particles. Nevertheless, as evidenced in Figures 3.24 (a) and (b), more intense welding processes take place at higher milling intensity for short-term milling (i.e., 1 h). Note that the particles corresponding to millings carried out at I2 are larger than those at I1. In fact, even for long-term milling (i.e., 20 h) at I1, particles are still agglomerate-shaped –see panel (e)–. Interestingly, for procedures at I2, the particle size decreases after 30 h of milling –compare panels (f) and (h)–.

Milling time (h)	I1 (326 rpm) I2 (460 rpm)	Austenite				Martensite	
		<D> (± 5 nm)	$\langle\varepsilon^2\rangle^{1/2}\cdot10^{-3}$ (± 0.5)	$\alpha\cdot10^{-3}$ (± 0.5)	$\beta\cdot10^{-3}$ (± 0.5)	<D> (± 5 nm)	$\langle\varepsilon^2\rangle^{1/2}\cdot10^{-3}$ (± 0.5)
0.5	I1	-	-	-	-	-	-
	I2	142	-	-	-	-	-
1	I1	141	-	-	-	-	-
	I2	117	-	2.7	2.9	83	3.1
5	I1	107	2.0	6.7	2.3	83	3.4
	I2	59	4.2	3.4	6.1	56	3.3
10	I1	117	2.8	4.0	5.5	85	3.7
	I2	61	4.5	3.3	6.2	46	3.2
15	I1	118	3.3	4.7	5.4	81	3.7
	I2	60	3.8	4.6	7.9	47	3.4
20	I1	117	3.5	3.7	13.6	76	3.7
	I2	57	7.4	4.3	15.7	45	3.3
30	I1	118	6.1	-	-	58	3.5
	I2	-	-	-	-	45	3.7

Table 3.3. *Crystallite sizes, <D>, and microstrains, $\langle\varepsilon^2\rangle^{1/2}$, of the austenite and martensite phases, deformation-type stacking fault probabilities, α, and twin-type stacking fault probabilities, β, of the austenite phase for ball-milled samples.*

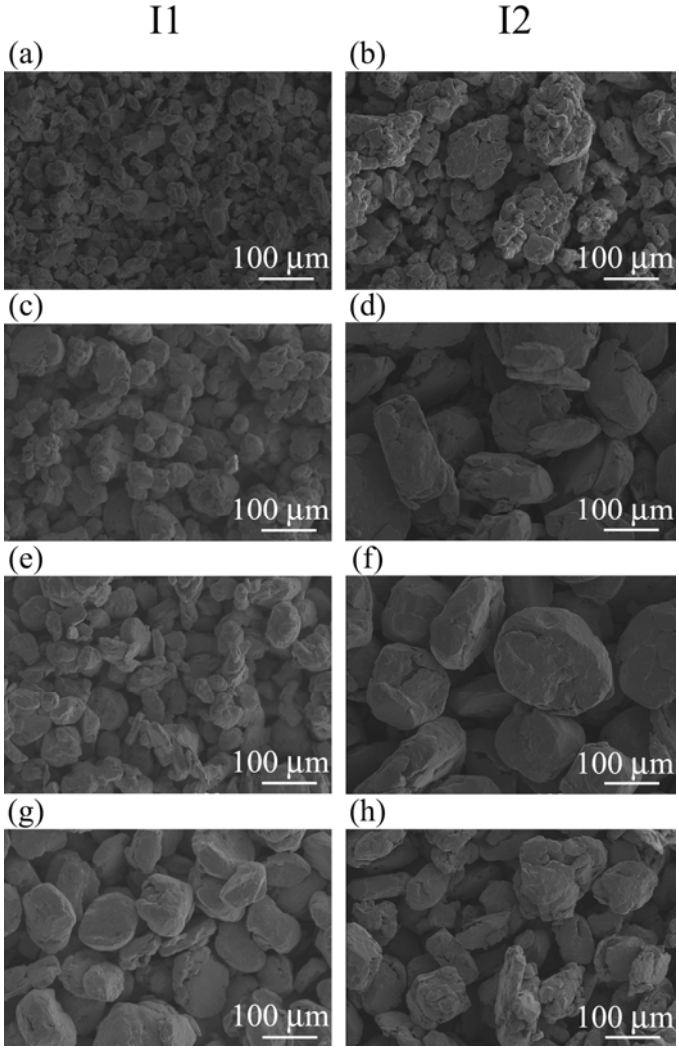

***Figure 3.24**. (a), (c), (e) and (g) are the scanning electron microscopy (SEM) images obtained using secondary electrons of the powders ball-milled using an angular frequency of 326 rpm (I1) during 1, 5, 20 and 30 h, respectively. Shown in (b), (d), (f) and (h) are the corresponding SEM images of the powdered specimens ball-milled using an angular frequency of 460 rpm (I2) during 1, 5, 20 and 30 h, respectively.*

3.2.A.1.2.2. Magnetic characterization

Shown in Figure 3.25 are the VSM loops recorded at room temperature for the samples ball-milled during 0.5 and 5 h –panel (a)– and 10 and 30 h –panel (b)– at either I1 or I2. Note that the as-annealed powders show paramagnetic behavior. The saturation magnetization, M_S, increases with the milling time. Moreover, larger M_S values are achieved when milling is carried out at I2 (i.e., when a higher strain rate is employed), corroborating the increase of the ferromagnetic counterpart. Since after 30 h of milling at I2, the $\gamma \rightarrow \alpha'$ transformation is almost completed (see Figure 3.22), this allows to

roughly estimate the saturation magnetization of the induced martensite, $M_S^{\alpha'} \approx 127$ emu/g.

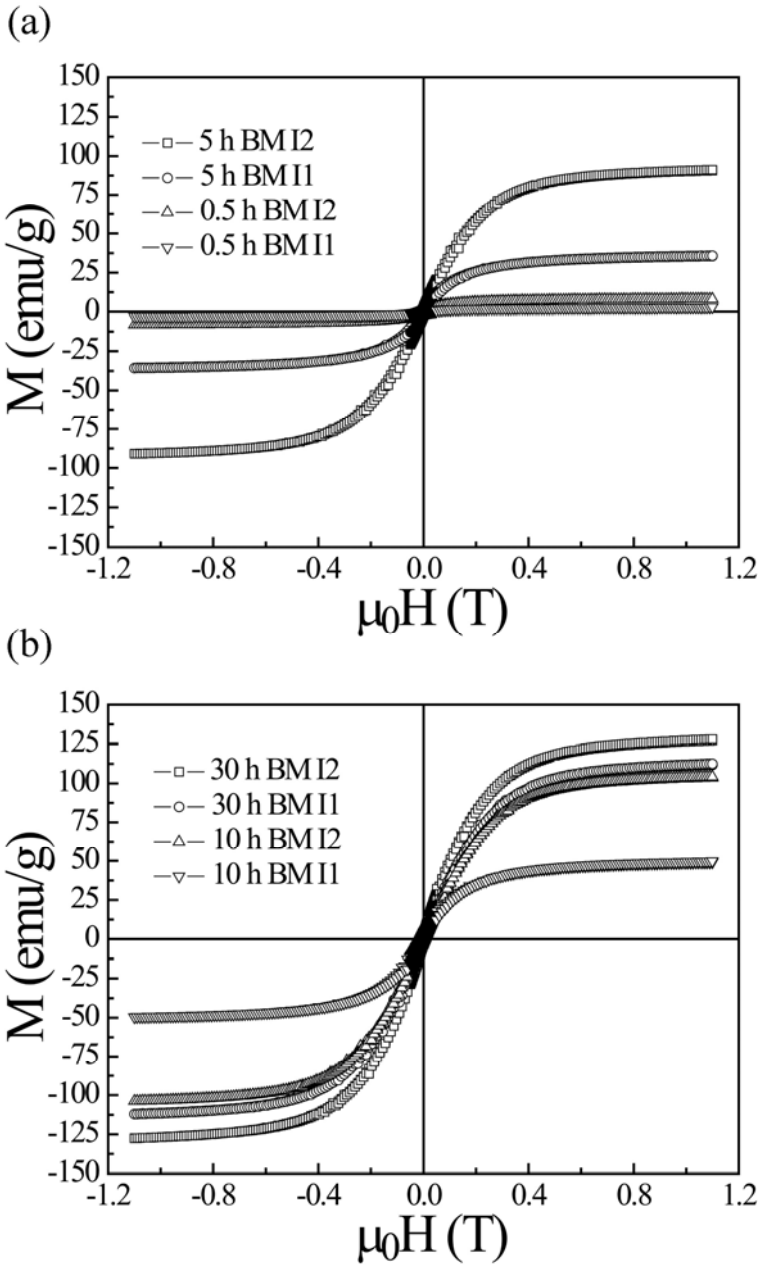

Figure 3.25. *Vibrating sample magnetometry measurements of the powders ball-milled at disk angular frequencies of 326 (I1) and 460 rpm (I2) during 0.5 and 5 h (a) and 10 and 30 h (b).*

3.2.A.1.3. Uniaxial compression of bulk AISI 316L specimens (quasi-static approach)

3.2.A.1.3.1. Structural characterization

Shown in Figures 3.26 (a) and (b) are the XRD patterns of the bulk AISI 316L samples compressed uniaxially up to 1.2, 3.2, 4.7 and 6.2 GPa using a loading rate of 0.1 kN/s and 1 kN/s, respectively, and a dwell time of 100 s.

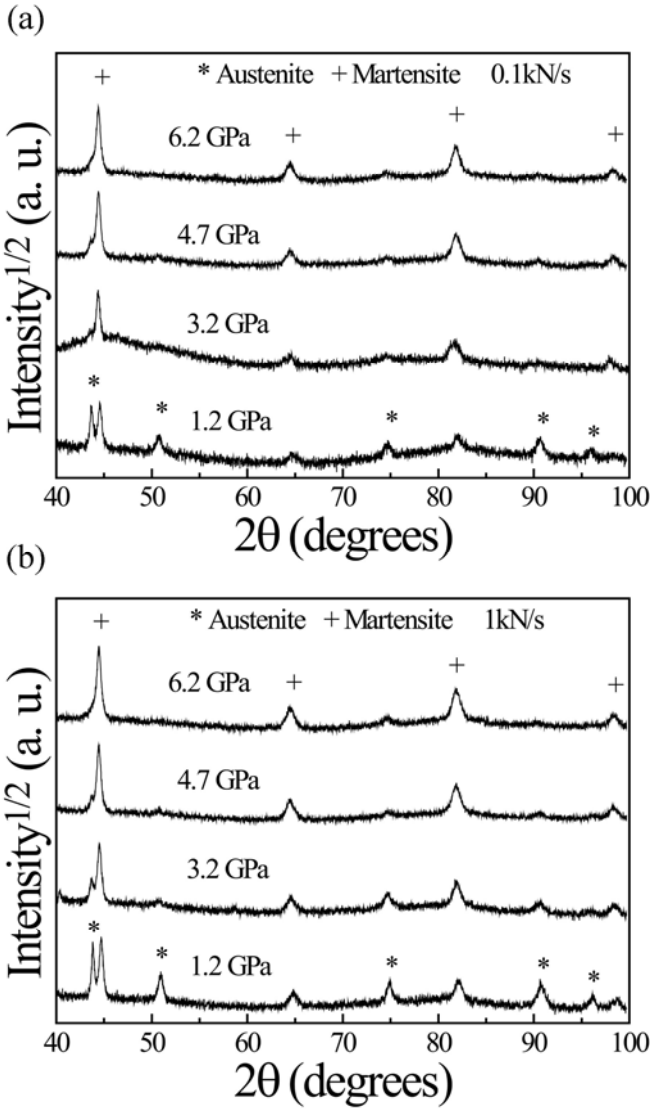

Figure 3.26. *(a) and (b) X-ray diffraction (XRD) patterns of the bulk AISI 316L samples compressed uniaxially up to 1.2, 3.2, 4.7 and 6.2 GPa using a loading rate of 0.1 kN/s and 1 kN/s, respectively, and a holding time of 100 s. Indicated in both panels are the main XRD peaks corresponding to austenite (*) and martensite (+) phases.*

In both cases, the amount of the α′ phase increases with the applied engineering stress, as it is evidenced by the increase of intensity of the α′ XRD peaks in detriment to the γ ones. Importantly, contrary to the BM powders, for a given engineering stress, the amount of martensite phase is larger for the lowest loading rate (see Figure 3.27).

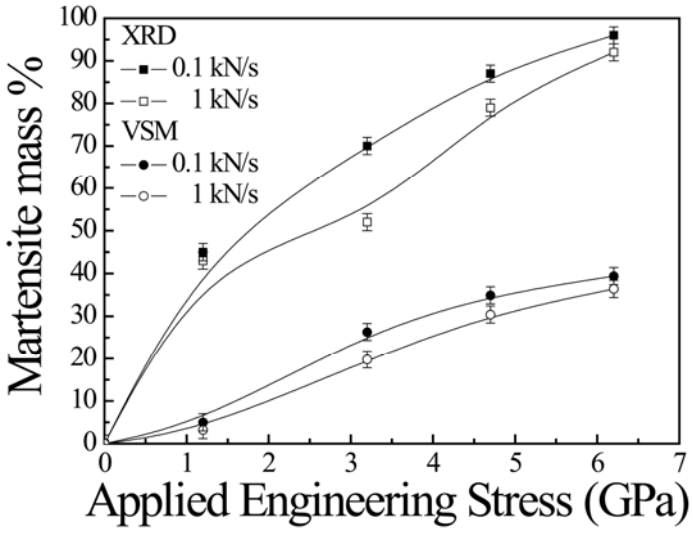

Figure 3.27. *Applied engineering stress dependence of the strain-induced martensite mass %, estimated from either X-ray diffraction analysis or vibrating sample magnetometry, for compressed specimens at both loading rates 0.1 and 1 kN/s. The lines are guides to the eye.*

As it happens in the dynamic approach, the crystallite size of the austenite phase remains rather constant as the engineering applied stress increases. Furthermore, no significant differences in crystallite sizes are obtained, for a given stress, when compression is performed either at 0.1 or 1 kN/s. Conversely, concerning the martensite phase, tests performed at 1 kN/s result in larger crystallite sizes than those carried out at 0.1 kN/s, although there are no considerable differences with the applied engineering stress. Nevertheless, the crystallite sizes of the martensite phase remain smaller than those corresponding to the austenite phase as occurs in ball milling. Concerning the microstrains, a steady value is attained for all the cases (see Table 3.4).

As expected, since compression tests result in a less severe straining process than ball milling, slightly larger crystallite sizes and smaller microstrains are obtained –compare Tables 3.3 and 3.4–.

Engineering Stress (GPa)	Loading Rate (kN/s)	Austenite				Martensite		H_{V1} [σ] (GPa)
		<D> (± 5 nm)	$<\varepsilon^2>^{1/2}\cdot10^{-3}$ (± 0.5)	$\alpha\cdot10^{-3}$ (± 0.5)	$\beta\cdot10^{-3}$ (± 0.5)	<D> (± 5 nm)	$<\varepsilon^2>^{1/2}\cdot10^{-3}$ (± 0.5)	
1.2	0.1	107	-	11.5	-	41	2.3	2.3 [0.2]
	1	106	-	8.7	2.9	76	2.8	1.9 [0.2]
3.2	0.1	109	-	11.6	2.5	55	3.0	2.9 [0.2]
	1	106	-	9.9	3.3	75	2.8	2.8 [0.1]
4.7	0.1	107	2.0	15.3	-	41	2.8	3.1 [0.3]
	1	106	2.7	13.4	1.7	80	2.8	3.0 [0.3]
6.2	0.1	-	-	-	-	40	2.8	3.5 [0.1]
	1	-	-	-	-	63	3.0	3.4 [0.1]

Table 3.4. *Crystallite sizes, <D>, and microstrains, $<\varepsilon^2>^{1/2}$, of the austenite and martensite phases, deformation-type stacking fault probabilities, α, and twin-type stacking fault probabilities, β, of the austenite phase and Vickers microhardness, H_{V1}, and its standard deviation for compressed samples.*

3.2.A.1.3.2. Magnetic characterization

As it can be seen in Figure 3.28, the M_S values increase significantly as the target engineering stress increases. The strain rate effect on the amount of transformed martensite can be clearly visualized in Figures 3.28 (a) and (b), where the VSM measurements of the bulk samples compressed uniaxially up to 1.2, 3.2, 4.7 and 6.2 GPa, using a holding time of 100 s and a loading rate of 0.1 kN/s –panel (a)– and 1 kN/s –panel (b)–, are shown. Note that, for a given applied engineering stress, the VSM loops corresponding to the samples tested at a higher loading rate (i.e., strain rate) have lower saturation magnetization. Since VSM is a bulk sensitive technique, this allows the total amount of transformed martensite to be inferred. Indeed, using the $M_S^{\alpha'}$ estimated from the virtually pure martensitic phase produced after long-term milling, quantitative information from the bulk of the sample can be readily obtained. As can be seen in Figure 3.27, although the overall trend of the percentage of α′ phase on the applied stress is the same for XRD and VSM characterization, there is a significant difference between the amount of α′ obtained from the two techniques. This stems from the limited penetration of the XRD into the material, probing only the top few μm (see section 2.3.1.6.2.).

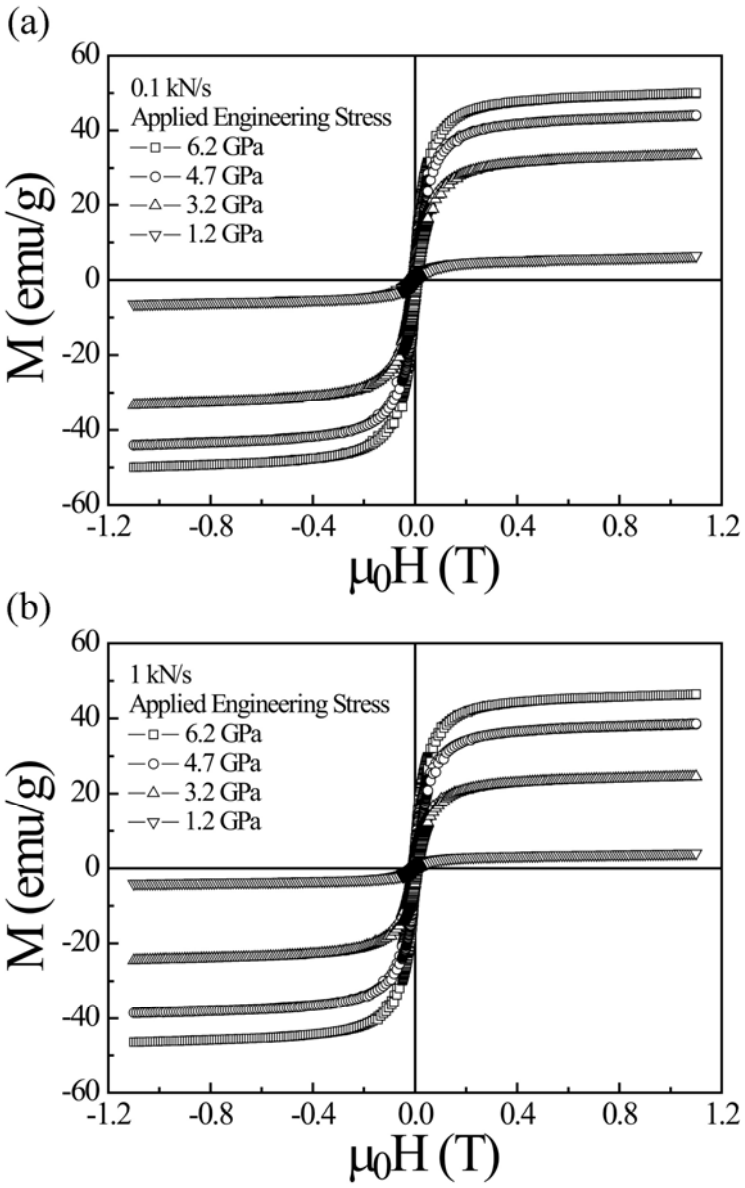

Figure 3.28. *Vibrating sample magnetometry measurements of the bulk AISI 316L samples compressed uniaxially up to 1.2, 3.2, 4.7 and 6.2 GPa using a holding time of 100 s and a loading rate of 0.1 kN/s (a) and 1 kN/s (b).*

3.2.A.1.3.3. Mechanical hardness characterization

The mechanical hardness, measured by means of Vickers microhardness with a load of 1 kg, shows a progressive increase with the applied engineering stress from H_{V1} = 2.3 to 3.5 GPa (for 0.1 kN/s) and H_{V1} = 1.9 GPa to 3.4 GPa (for 1 kN/s) –see Table 3.4–. Note that this increase of hardness correlates with the progressive formation of the martensite phase as deformation proceeds. For a given engineering stress, a slightly higher H_{V1} is

obtained for lower strain rate, as expected from the slightly higher martensite percentage.

3.2.A.1.4. Mechanisms of the strain-induced transformation: static vs. dynamic approaches

Since ASSs are low-energy stacking fault materials, the assessment of these planar defects (i.e., stacking faults) becomes a crucial aspect in order to investigate the structural transformations of these alloys. Namely, stacking faults play a relevant role in the strain-induced martensite formation [44,45] since, in FCC lattices, stacking faults are of hexagonal symmetry, like ε-martensite (HCP). Upon mechanical deformation, at early stages, this phase is formed by the overlapping of "n" neighboring stacking faults. It is known that shear bands consisting of stacking fault bundles and deformation twins are created as deformation proceeds and their intersections become potential sites for the nucleation of the ferromagnetic α' phase [45-48]. Thus, the transformation from austenite to α'-martensite is believed to follow $\gamma \rightarrow SF \rightarrow n \cdot SF \rightarrow \varepsilon \rightarrow \alpha'$ [49,50]. The volume fraction of ε-martensite is known to be dependent on the strain, reaching a maximum of around 10 % (volume percentage), at a strain of 0.05, and decreasing thereafter [51]. However, since this phase is formed at early stages of the deformation process and the ε-martensite percentage is rather small, this phase cannot be detected in our specimens.

Concerning the dynamic approach, larger angular frequencies result in more intense milling procedures (i.e., to more energetic and rapid collision processes). Hence the more severe milling, I2, leads to smaller crystallite sizes, larger microstrains and greater strain-induced plastic deformations, and larger amounts of stacking faults –see Table 3.3–. This is in agreement with previous reported results on milling processes of 304 stainless steel by means of a vibratory mill [52]. As the austenite phase accommodates strain, an augment of stacking fault density (which leads to a decrease in the distance between shear bands) occurs –see Table 3.3– resulting in the $\gamma \rightarrow \alpha'$ transformation. As it can be seen in Table 3, the total amount of stacking faults –i.e., $\alpha + \beta$– in the parent γ phase is larger for milling processes carried out at I2 for any milling time. This

evidences that the retained (i.e., non-transformed) austenite phase, when using I2, is more prone to form α' than that one corresponding to I1 routes, as it is confirmed by the greater amounts of transformed α' (see Figure 3.23). The presence of twin faults in the γ phase is favored by both the low stacking fault energy of ASSs and the high strain rates associated with ball milling. It is actually known that, under conditions of shock loading (such as ball milling), twin deformation prevails over deformation slip modes (note, as a general trend, that β values are larger than α ones, see Table 3.3). Importantly, an increase of the angular frequency in ball milling processes should lead to higher temperature rises, ΔT, during the milling due to the accommodation processes of plastic deformation. This ΔT (estimated to be in the $\Delta T \approx$ 40-400 K range from different ball milling processes [53-55]) could lead to the annihilation of stacking fault bundles and thus, to a certain extent, to the reverse transformation, $\alpha' \rightarrow \gamma$. In fact, the local heating effect is indirectly evidenced by the morphology of the particles (Figure 3.24), where the particle sizes of powders milled using I2 are larger and poliedric (evidencing increased welding) than those ones corresponding to I1 milling processes, which are agglomerate-like. However, one has to bear in mind that, in the dynamic deformation range, the local heating during ball milling takes place during very short time scales, Δt, (i.e., shock loading). Thus, probably, the total energy brought about by the local heating is insufficient to trigger the $\alpha' \rightarrow \gamma$ transformation [56]. Hence, overall, higher strain rates promote the $\gamma \rightarrow \alpha'$ transformation and, consequently, a concomitant work hardening phenomenon. Therefore, strain-hardening plays a more important role than thermal softening in this dynamic approach. In addition, long-term milling (i.e., 30 h) at I2 causes a particle size reduction –compare panels (f) and (h) of Figure 3.24–, evidencing that structural refinement is more significant than thermally-induced diffusive processes (e.g., welding) for long-term milling.

Remarkably, in contrast to the austenite phase, the crystallite size of the martensite phase tends to decrease for long-term milling, while microstrains remain almost unaltered. This fact can be ascribed to the more brittle nature of the induced martensite, since it is more prone to nucleate new grains than to modify its structure.

Regarding the compression tests, although the heating during compression, ΔT, is probably smaller than during ball milling, it occurs in a continuous manner (i.e., Δt is much longer). This temperature rise is known to cause annihilation processes of the shear-band intersections in the austenite phase, resulting in lower amounts of potential nucleation sites for martensite formation [44,45]. Thus, the aforementioned thermal softening (e.g., annihilation of stacking fault bundles) plays a more relevant role in the restriction of the amount of transformed martensite, particularly at higher rates (when the temperature rise is higher), since the time interval for release of heat decreases (i.e., short time to accommodate strain) [47,57,58]. Thus, the strain rate plays an opposite role in compression testing and ball milling procedures. As a consequence, in quasi-static approaches, lower amounts of generated martensite phase are encountered [49]. Moreover, the amount of deformation-type stacking faults is larger than twin-type ones (see Table 3.4), suggesting that slip becomes a major operative mechanism for plastic accommodation of the austenite phase during compression, since quasi-static tests lead to a rather continuous deformation route.

The magnetic measurements confirm the trends exhibited by the XRD results as can be seen by the linear dependence of the saturation magnetization on the % of martensite of the ball-milled samples (see Figure 3.29).

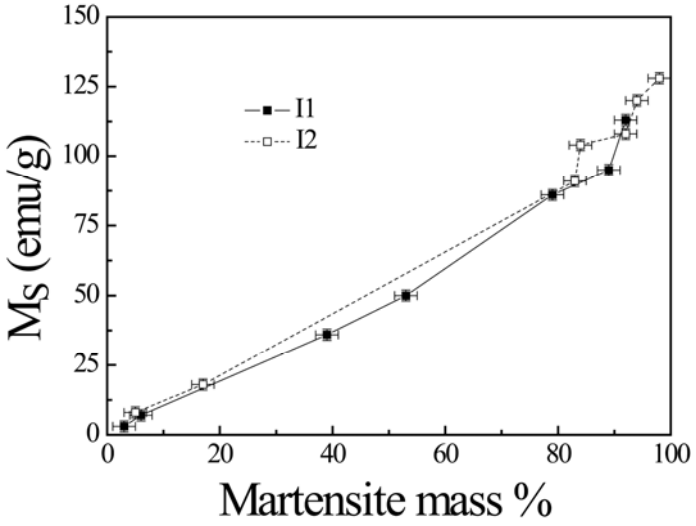

***Figure 3.29**. Martensite mass % dependence of the saturation magnetization of the ball-milled samples for the used milling intensities (I1=326 and I2=460 rpm). The lines are guides to the eye.*

Nevertheless, comparing the percentages of α′ phase obtained by XRD and magnetic measurements, both techniques give similar results in ball milling whereas, in compression tests, XRD gives much higher values of α′ phase. Since the penetration depth of the XRD is limited to a few micrometers, the results imply that in ball milling the whole particles transform, while in compression tests the transformation starts from the surface inwards. Thus, the maximum applied pressure is insufficient to transform the bulk of the specimen.

Finally, note that since the hardness of BCC materials is expected to be higher to that one corresponding to FCC materials due to the limited number of slip systems in BCC materials [9], the hardness increases with the amount of martensite, thus allowing to correlate mechanical and microstructural aspects (see Table 3.4) in bulk specimens.

3.2.A.2. Micro and nanoscaled approaches: nanoindentation

Periodic arrays of magnetic structures with micrometrer and submicrometer lateral sizes have been prepared in a controlled manner at the surface of an AISI 316 austenitic stainless steel by means of local deformation using a nanoindenter. This method takes advantage of the previously described mechanically-induced phase transformation (from non-magnetic FCC austenite to ferromagnetic BCC martensite) that occurs in austenitic steel upon plastic deformation.

3.2.A.2.1. Experimental details

The AISI 316 steel piece is first cut into fine sheets and subsequently polished to mirror-like appearance. To eliminate possible magnetic contributions created during the initial processing, the sheets are subsequently annealed for 30 min at 1100 ºC (which is above the reverse, martensite-to-austenite, phase transformation temperature [43]), under vacuum (air pressure < 10^{-5} mbar), and cooled down to room temperature. Arrays of 15 × 15 triangular indentations with lateral sizes in the micrometer and sub-micrometer range have been prepared by means of nanoindentation, operating in the load control mode, and using a Berkovich-type diamond tip (pyramidal-shaped). The

indentation function consists of a loading segment of 15 s, applying a maximum forces of 0.75, 2.5 and 9 mN, a load holding segment of 10 s and an unloading segment of 15 s. Arrays of lines (80 μm long) have been prepared by scratching, i.e., dragging the indenter tip at a constant force of 3.5 and 5 mN and at a rate of 10 μm/s. The morphology of the locally deformed regions is examined by SEM and AFM. Hysteresis loops of the deformed and non-deformed areas have been recorded using a MOKE setup. Hysteresis loops have been recorded along different in-plane angles to analyze possible effects from magnetic anisotropies. MFM imaging is used to check the local character of the induced ferromagnetism and to probe possible domain patterns within the indented regions.

3.2.A.2.2. Magnetic patterning

Shown in Figure 3.30 (a) is a scanning electron microscopy image (obtained using secondary electrons) of the array of indentations obtained on the steel sheet after applying a maximum loading force of 0.75 mN.

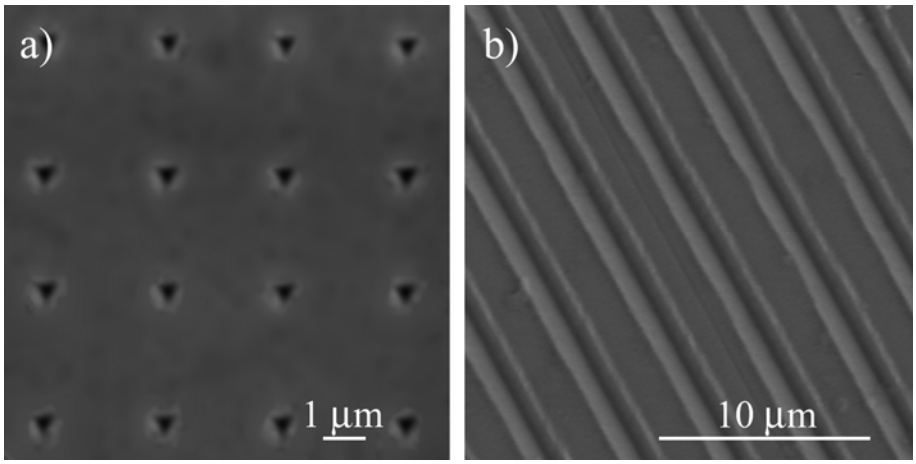

Figure 3.30. *Scanning electron microscopy (SEM) images corresponding to (a) the array of indentations obtained applying a maximum loading force of 0.75 mN and (b) the array of lines obtained by dragging the nanoindenter tip at 10 μm/s applying a constant load of 3.5 mN.*

The indentations are roughly triangular due to the pyramidal shape of the indenter (as it is also evident from the AFM image shown in the upper panel of Figure 3.31 (a), corresponding to an applied force of 9 mN).

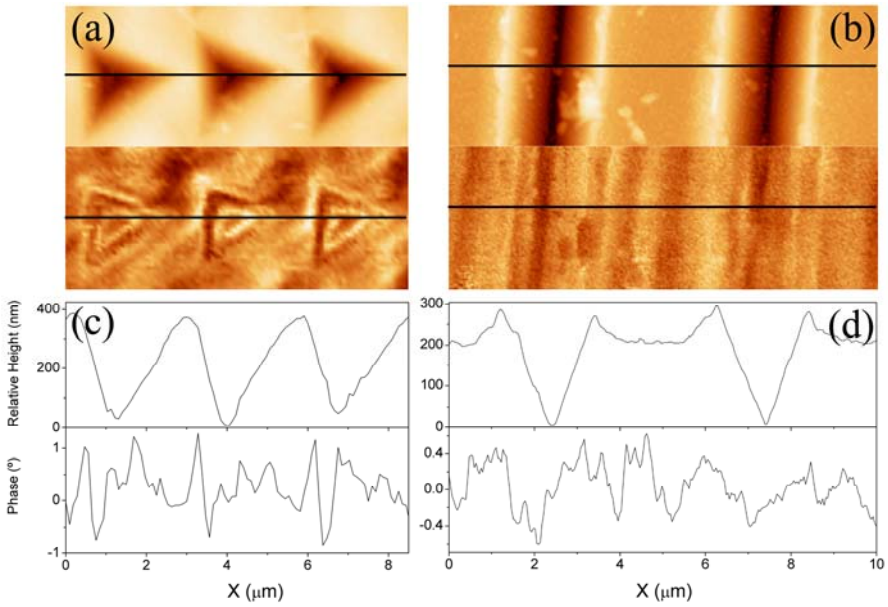

Figure 3.31. *(a) Atomic force microscopy (AFM) image –upper panel– and magnetic force microscopy image (MFM) –bottom panel– corresponding to the array of indentations obtained applying a maximum load of 9 mN; (b) AFM –upper panel– and MFM –bottom panel– images of a portion of the array of lines obtained by scratching with an applied load of 5 mN; (c,d) line profiles of the AFM (i.e., relative height) and MFM (magnetic contrast, i.e., phase) pictures, corresponding to the positions indicated in Figures 3.31 (a) and 3.31 (b).*

For loads of 0.75, 2.5 and 9 mN, the lateral dimensions of the indentations are of approximately 400 nm, 1 μm and 2.8 μm, respectively. Other structures, e.g. lines, can be also produced by simply dragging the indenter tip onto the surface of the austenitic stainless steel. Two arrays of lines, with widths of 1.8 and 2.3 μm, are shown in Figure 3.30 (b) (SEM) and the upper panel of Figure 3.31 (b) (AFM), corresponding to applied forces of 3.5 and 5 mN, respectively. A slight deformation just around each line is observed (i.e., pile-up). This can be clearly visualized in the line scan of Figure 3.31 (d), where there is a clear maximum at the edges of the created lines.

From the dependence of the displacement into the sample on the applied force, an average hardness of 2.7 GPa and a reduced elastic modulus of 220 GPa are obtained, which are values typical for austenitic stainless steel [59].

Figure 3.32 (a) reveals that when the MOKE measurement is carried out after cutting and polishing the steel pieces, a clear ferromagnetic hysteresis loop with a coercivity

$\mu_0 H_C$ = 3.5 mT is measured, which indicates that the initial processing (i.e., cutting and polishing) already induces a partial transformation from austenite to martensite.

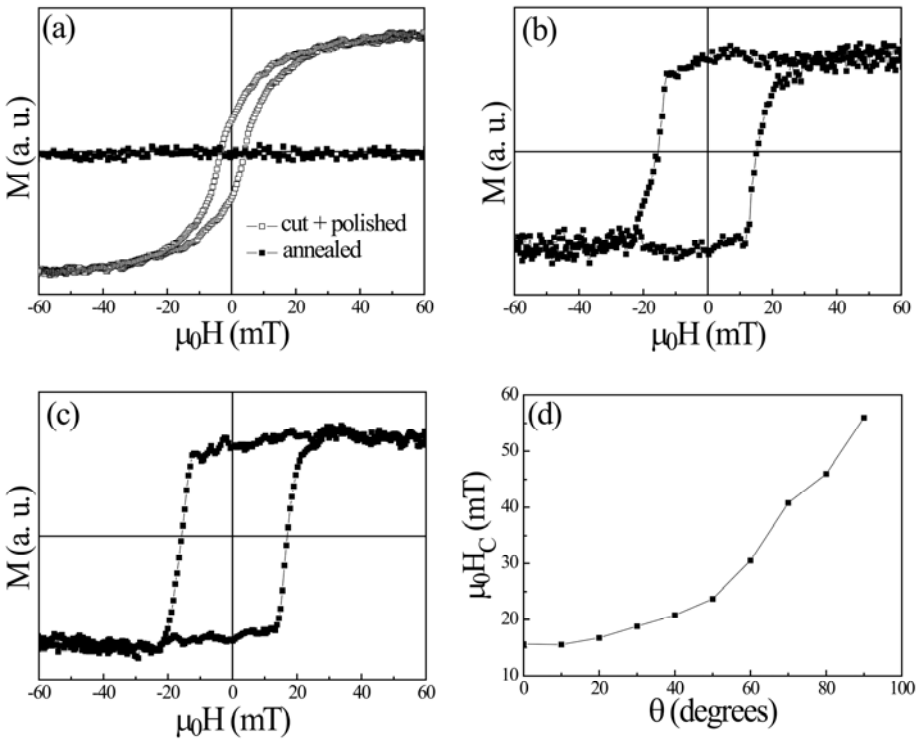

***Figure 3.32**. (a) Magneto-optic Kerr effect (MOKE) hysteresis loop (opened symbol) obtained after cutting and polishing (before annealing) the austenitic stainless steel, together with the linear relationship (filled symbol) observed between the magnetization and the applied field after annealing the steel at 1100 ºC for 30 min; (b) MOKE hysteresis loop corresponding to the array of indentations with lateral size of 1 μm; (c) MOKE hysteresis loop obtained from the array of lines (1.8 μm wide) measured along the direction of the lines; (d) dependence of the coercivity, H_C, on the angle of measurement for the array of 1.8 μm wide lines. The lines are guides to the eye.*

The subsequent annealing of the steel at 1100 ºC for 30 minutes completely transforms the martensite back to austenite (as confirmed by XRD in the macroscopic approach). Moreover, after annealing, when MOKE measurements are performed away from the arrays of indentations (i.e., undeformed material), a straight line is obtained –see Figure 3.32 (a)–, which corresponds to the austenite at room temperature.

When MOKE measurements are carried out in the indented regions, hysteresis loops typical of ferromagnetic behavior are recovered, indicating that nanoindentation is indeed a versatile tool to controllably induce ferromagnetism at small length scales in

these ferrous alloys. From the hysteresis loop corresponding to the array of 400 nm –see Figure 3.32 (b)–, a coercivity value of $\mu_0 H_C$ = 15 mT is obtained, which represents about a four-fold increase with respect to H_C measured after cutting and polishing the austenitic steel piece (i.e., before annealing). This large H_C may be due to the physical constraints that the reduced sizes of the indented regions impose on the propagation of magnetic domains [22,27]. No variations in H_C are observed when varying the in-plane angle of measurement. Similar coercivity values, again without angular dependence, are obtained for the other arrays of triangular indentations. Conversely, for the arrays of lines, the coercivity is found to be dependent on the direction of the measurement. For example, for the array of 1.8 μm wide lines, the coercivity evaluated from the loop recorded along the direction of the lines –Figure 3.32 (c)– is $\mu_0 H_C$ = 16 mT and it increases progressively as the angle of measurement, θ, approaches 90º from the direction of the lines –see Figure 3.32 (d)–, reaching a maximum value of 56 mT. These results may be interpreted as being due to the competition between magneto-static energy (which, for the relatively large thickness of the lines, favors magnetization reversal via curling mechanisms or formation of multidomain states) and anisotropy energy [22-24].

To further assess the local character of the generated ferromagnetism, the indented samples have been imaged by MFM. The MFM images, with the corresponding AFM images, of the array of triangular indentations with 2.8 μm lateral size and a portion of lines (2.3 μm wide) are shown in Figures 32 (a) and (b), respectively. Dark and bright areas are observed by MFM inside the triangular indentations while no contrast is observed outside the indentations (except for the deformed material just around each indentation). As can be seen in Figure 3.31 (b), some fringes can be observed both inside and between the lines (also because the scratch experiments deform, to some extent, the material surrounding the lines). The fact that the MFM images indeed correspond to magnetic (and not simply topographic) contrast can be confirmed by plotting line scans across the AFM and MFM images. As shown in Figures 3.31 (c) and (d), the topographic (from AFM) and magnetic (from MFM) profiles do not coincide, thus the MFM images are indeed representative of the multidomain structure inside the indentations. Nevertheless, these images are not straightforward to interpret because the

surfaces are not flat and, therefore, both in-plane and out-of-plane magnetization components probably coexist. However, MFM clearly confirms that ferromagnetism is locally induced by the nanoindentation experiments.

Finally, the indented austenitic steel sheet has been annealed again at 1100 ºC for 30 minutes. This process resulted in a MOKE signal without hysteresis, resembling the straight line shown in Figure 3.32 (a). Actually, the magnetic information has been removed, even though the physical marks caused by the nanoindentation still remain.

3.2.B. Ferromagnetism induced by ion irradiation

The influence of the irradiation temperature and time on the magnetic and structural properties of AISI 304L ASSs after ion beam nitriding is reported. Moreover, periodic arrays of ferromagnetic structures in the micrometer and sub-micrometer scale have been prepared at the surface of these steels by direct magnetic patterning using shadow masks. This method takes advantage of the formation of the ferromagnetic supersaturated nitrogen solid solution γ_N phase (i.e., expanded austenite) upon nitriding at moderate temperatures [60-62].

Regrettably, it should be mentioned that noble gas ion irradiation, at the same fluence range used to generate ferromagnetism in $Fe_{60}Al_{40}$ alloys, is not able to induce the martensitic transformation in ASSs, thus these alloys remain paramagnetic.

3.2.B.1. Macroscopic approach: broad beam ion beam nitriding

3.2.B.1.1. Experimental details

Disk-shaped samples (10 mm diameter and 2 mm thickness) have been cut from commercial AISI 304L ASS polycrystalline bars and then polished to mirror-like appearance using diamond paste and, as a final step, SiO_2 particles. It is worth mentioning that no traces of stress-induced martensite have been found after this pre-treatment step, therefore, resulting in a non-ferromagnetic surface.

Ion beam nitriding processes (i.e., ion irradiation using nitrogen ions) have been carried out with a Kaufman type ion source in the temperature range of 300-400ºC. The ion energy and the ion current density are ≈ 1 keV and 0.5 mA/cm^2, respectively. The ratio of the charge species in the ion beam has been estimated to be 55% N_2^+ and 45% N^+ [63], corresponding to the flux of ≈ $3 \cdot 10^{15}$ ions·cm^{-2}·s^{-1}. The processing times are 5 or 30 minutes.

Quantitative nitrogen depth profiles have been determined by nuclear reaction analysis (NRA) using the $^{14}N(d^+,\alpha)^{12}C$ nuclear reaction at an incident deuterium energy of 1.4 MeV. The structure of the modified surface layer has been also investigated by XRD with a fixed incident angle of 1º (i.e., glancing incidence mode). The magnetic properties of the homogeneously nitrided areas have been determined by MOKE magnetometry.

3.2.B.1.2. Structural and magnetic characterization

The structure of the virgin ASS sample is consistent with the FCC lattice structure (i.e., austenite phase, γ). Conversely, as can be seen in Figure 3.33, for the nitrided samples, each austenite peak exhibits a satellite peak, located at lower diffraction angles (i.e., lattice expansion), which are related to the formation of the "expanded austenite".

The amount of the γ_N phase increases with the processing temperature, as it is evidenced by the increase of intensity of the γ_N XRD peaks at the expense of the γ ones. It is noteworthy that after nitriding at 300ºC for 5 min the austenite peaks are already slightly asymmetric (see Figure 3.33) due to the existence of tiny tails located on the left hand side of the austenite XRD peaks. This indicates the incipient formation of the "expanded austenite" phase even for rather mild conditions. Interestingly, peaks located ≈ 38.8º might be attributed to hexagonal iron nitrides (ε-Fe_3N_{1+x}-type) –see Figure 3.33–.

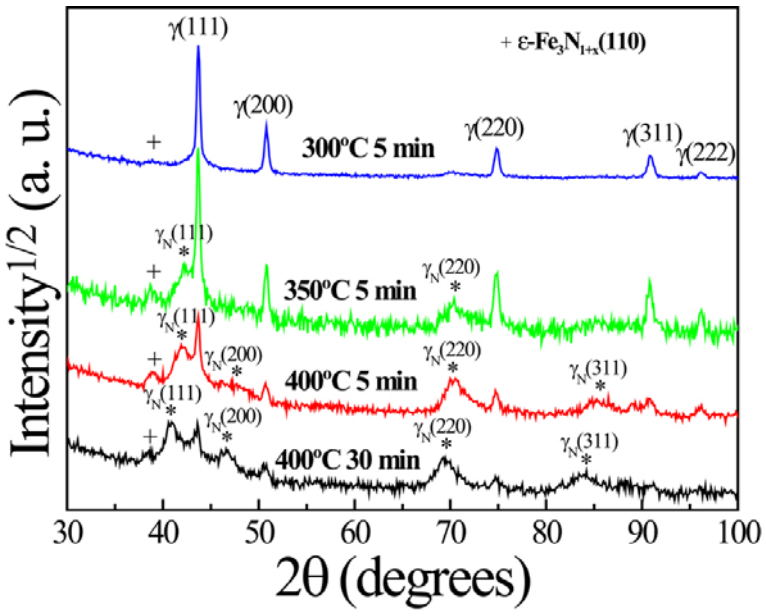

Figure 3.33. *X-ray diffraction patterns of nitrided ASS samples (nitriding duration 5 min for 300 and 350°C and 5 and 30 min for 400ºC). The stars correspond to the γ_N phase and the plus symbols to the ε-Fe_3N_{1+x}-type phase.*

The above structural results are consistent with NRA observations –see Figure 3.34–.

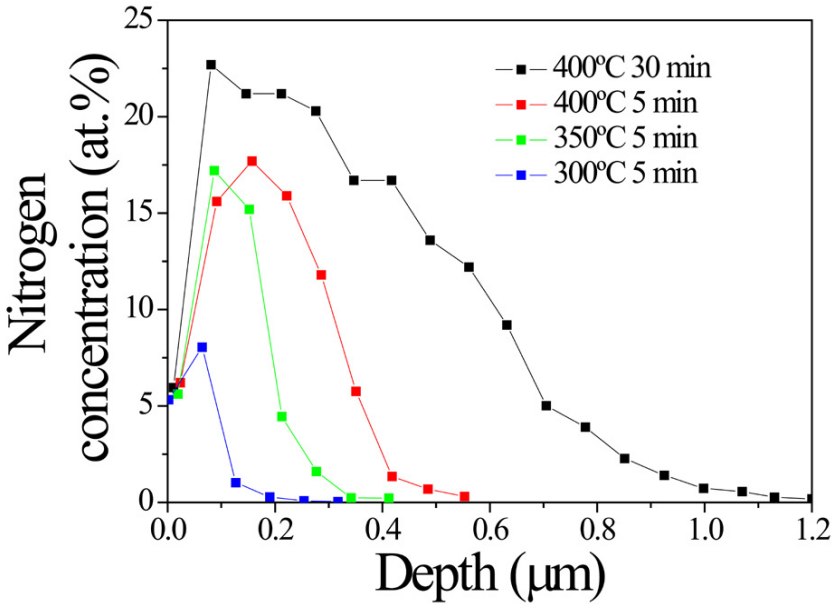

Figure 3.34. *Nuclear reaction analysis nitrogen distribution profiles of the nitrided AISI 304L ASS specimens. The lines are guides to the eye.*

Actually, for higher processing temperatures and/or longer treatments, the retained fluence and maximal nitrogen concentration are larger and the nitrogen penetration is deeper. For instance, the depth of the nitrogen-rich layers corresponding to the

400ºC/5min and 400ºC/30min nitrided samples is around 0.6 and 1.2 μm, respectively (see Table 3.5) [64].

As expected, the implanted fluences, obtained by multiplying the ion flux and the processing time (i.e., 5 or 30 minutes), are larger than the retained ones, obtained from the integration of the curves in Figure 3.34, since both backscattering and sputtering processes take place during nitriding. Moreover, whereas the maximal nitrogen concentration corresponding to the samples 350ºC/5min and 400ºC/5min is rather similar, the retained fluence of the 400ºC/5min sample is almost twice the value of the 350ºC/5min specimen, evidencing the role of temperature in promoting nitrogen interstitial diffusion and, therefore, in achieving larger nitrogen penetration depths.

Sample	300°C/5min	350°C/5min	400°C/5min	400°C/30min
Implanted nitrogen fluence (atoms/cm^2)·10^{17}	9	9	9	54
Retained nitrogen fluence (atoms/cm^2)·10^{17}	0.66	2.4	4.3	11
Maximal nitrogen concentration (at.%)	8.1	17.2	17.7	22.7
Sputtered depth (nm)	85	82	152	240
Standard deviation (nm)	10	12	20	23

***Table 3.5**. Implanted fluences, retained fluences, maximal nitrogen concentrations and sputtered depth of the patterned areas together with its standard deviation corresponding to the specimens 300ºC/5min, 350ºC/5min, 400ºC/5min and 400ºC/30min.*

Remarkably, as can be seen in Figures 3.35 (a), (b) and (c), MOKE measurements of the nitrided samples exhibit a clear ferromagnetic behavior.

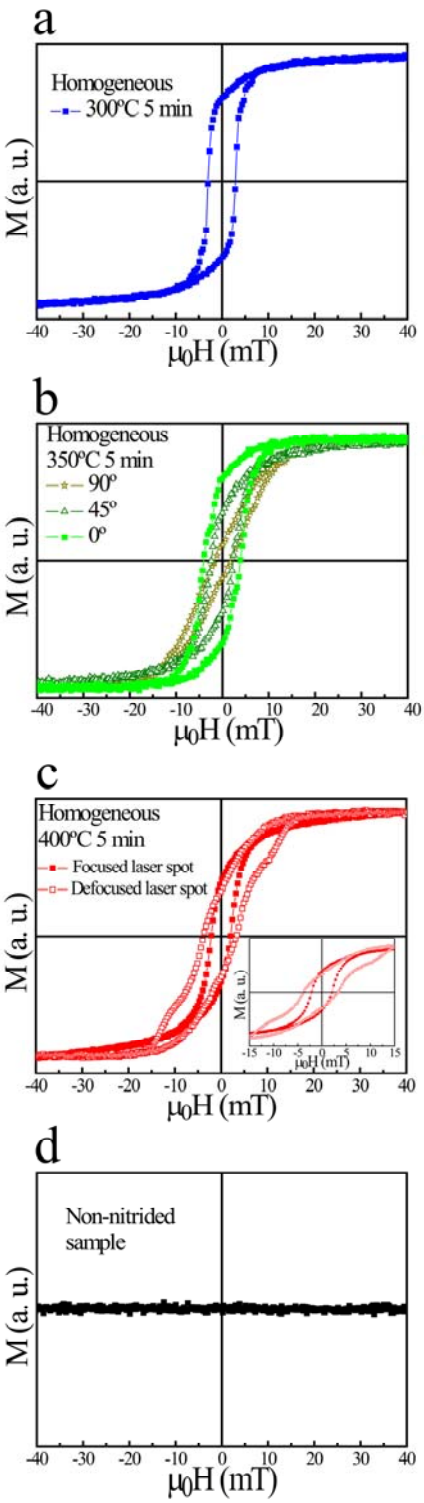

Figure 3.35. *(a) Focused magneto-optic Kerr effect (MOKE) loop of the sample 300ºC/5min nitrided. (b) Focused MOKE measurements of sample 350ºC/5min along the hard axes (90º), 45° and the easy axes (0º). (c) Focused and defocused MOKE loops of sample 400ºC/5min. The inset in (c) shows an enlarged image of the MOKE loops. (d) MOKE measurements of the non-nitrided specimen. Measurements in panels (a), (b) and (c) correspond to homogeneously nitrided samples.*

Moreover, since the average grain size of the ASS samples is about 30 μm and the employed laser spot of the MOKE apparatus is focused down up to 3 μm in diameter, changes in the remnant magnetization, M_R, and coercivity, H_C, are observed when varying the in-plane angle of measurement –Figure 3.35 (b)– due to the crystallographic orientation of the measured grain with respect to the applied field (i.e., magneto-crystalline anisotropy). Note that both the remnant magnetization and the coercivity, H_C, decrease when increasing the in-plane angle of measurement (i.e., from 0º –easy axes– to 90º –hard axes–). Measurements carried out in other regions (i.e., other grains), often lead to different magnetization reversal curves due to the different orientations of the various grains with respect to the applied field direction. In addition, measurements using a completely defocused laser spot ≈ 100 μm diameter have been also performed, resulting mainly in hysteresis loops comprising all in-plane contributions due to the random grain orientation –see Figure 3.35 (c)–. Comparing the hysteresis loops of the different samples –Figures 3.35 (a)-(c)–, it can be seen that the induced coercivity is comparable for all samples since the nature of the generated phase is similar in all cases. Interestingly, taking into account that MOKE is a surface sensitive technique, this implies that all the nitriding treatments induce sufficient nitrogen content at the surface of the sample to induce a ferromagnetic phase. Note that the virgin ASS samples exhibits no MOKE signal (i.e. non-hysteretic behavior) –see Figure 3.35 (d)–. However, as it can be seen in Figure 3.35 (a), short-term irradiation at 300 ºC already yields an easily measurable ferromagnetic response. This is consistent with glancing incidence XRD, which shows that, even for the mildest conditions, expanded austenite is formed. However, this may appear to be in contrast with NRA, although one has to bear in mind that the depth resolution of NRA is around 150 nm near the surface [61]. Thus this technique would not be able to determine the nitrogen concentration of the sample nitrided at 300ºC during 5 minutes, since its nitrogen penetration depth (see Figure 3.34) is almost the depth resolution of NRA at the surface. Nevertheless, the presence of ferromagnetic hexagonal iron nitrides (ε-Fe_3N_{1+x}-type [65,66]) within the nitrided layer may, to some extent, also explain the ferromagnetic character of the sample nitrided at 300 ºC during 5 min.

3.2.B.2. Micro and nanoscaled approaches: lithography through shadow masks

3.2.B.2.1. Broad beam ion beam nitriding through TEM grids

3.2.B.2.1.1. Experimental details

For the micrometer-sized patterning process, a 2000 mesh Cu TEM grid (with a mesh size of 7.5 x 7.5 μm^2, 12.5 μm pitch, 20 μm thickness and 3.05 mm diameter), placed on the surface of the ASS samples, has been employed as a shadow mask in the nitriding processes (same conditions as in the homogeneous approach) to fabricate arrays of ordered ferromagnetic entities in the micrometer scale.

The local character of the induced ferromagnetism has been confirmed by MOKE measurements together with MFM imaging. Finally, AFM imaging has been used to examine the surface topography of the produced patterns.

3.2.B.2.1.2. Magnetic patterning

As can be seen from the MFM image of sample nitrided at 400 ºC for 5 min through a TEM grid –Figure 3.36 (a)–, magnetic patterns of a few microns in size are indeed formed at the surface of the sample.

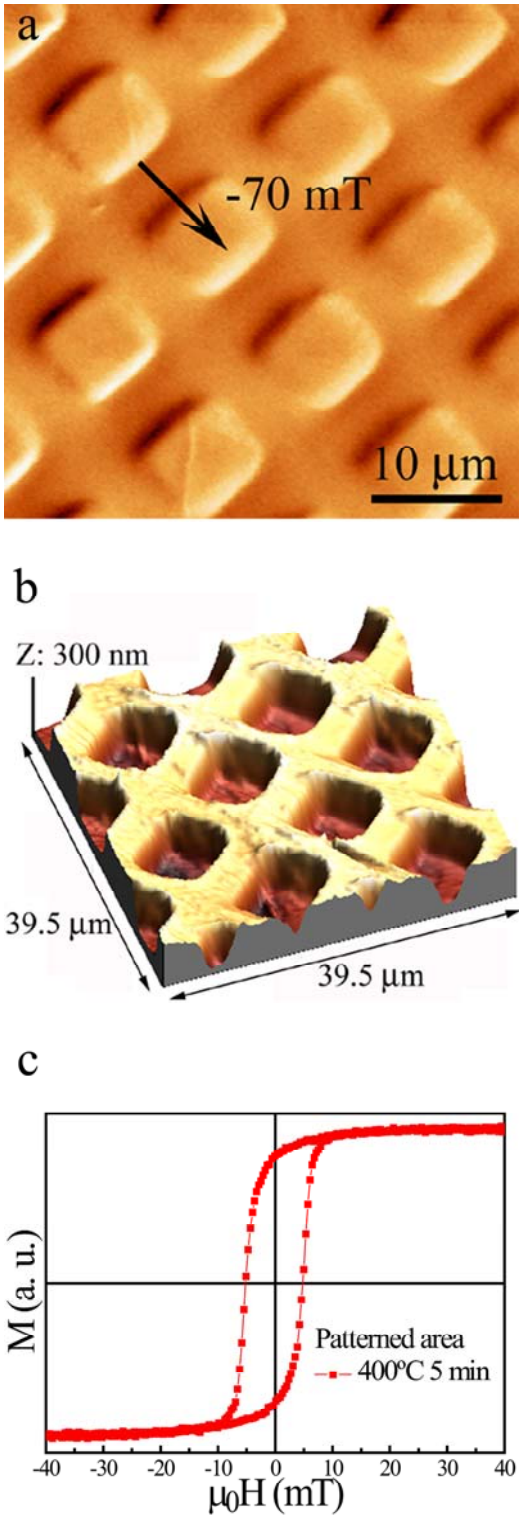

Figure 3.36. *(a) Magnetic force microscopy image of a patterned area of the sample nitrided at 400ºC/5min taken in an applied magnetic field of -70 mT, together with the corresponding 3D atomic force microscopy image image (b). (c) Magneto-optical Kerr effect loop –obtained after focusing the laser spot– of the patterned region of the sample nitrided at 400ºC/5min.*

Figure 3.36 (a) is the corresponding MFM image of Figure 3.36 (b) –topographic image– taken in an applied magnetic field of -70 mT, where a magnetic dipolar contrast can be clearly seen in each entity, confirming the feasibility of the production of periodic arrays of isolated ferromagnetic structures (i.e., dark and bright areas due to magnetic stray fields are only observed inside the patterns while no contrast is visualized outside the structures).

The AFM image of the patterned area –Figure 3.36 (b)– shows that a sputtering process of the surface took place during nitriding (see also Table 3.5), resulting in the formation of a periodic array of squared pits. Since the sputtering depends on crystalline orientation and the samples are polycrystalline, an average value of the sputtered depth is given in Table 3.5. Note that the aforementioned corrugation process of the diverse surfaces is more pronounced for longer irradiation times and/or higher temperatures. The hysteresis loop of the patterned area obtained by MOKE is shown in Figure 3.36 (c). The hysteresis behavior of the patterned areas and the homogeneously nitrided ones are quite similar due to the fact that the induced ferromagnetic structures are relatively large (micrometer range), leading to entities with magnetic multidomain configurations [22]. MFM and MOKE measurements confirm that the ferromagnetic entities are surrounded by a paramagnetic matrix, as expected, since the distance between the structures is in the micrometer range and nitrogen lateral diffusion is far less than one micrometer (in fact, penetration depth for the most nitrided sample is about 1.2 μm).

As in the continuous (i.e., homogeneous) approach, changes in H_C are also observed when varying the in-plane angle of measurement due to magneto-crystalline anisotropy, since the corresponding MOKE measurements were performed using a focused laser spot. As expected, after defocusing the laser spot (i.e., several grains measured), hysteresis loops composed by both easy and hard axis contributions are again obtained.

3.2.B.2.2. Broad beam ion beam nitriding through alumina masks

3.2.B.2.2.1. Experimental details

For the submicrometer-sized patterning, alumina membranes (5 μm thickness with pseudo-ordered 300-350 nm diameter pores, self-organized in hexagonal arrays), prepared by means of anodization procedures [67], have been used in order to obtain magnetic patterns in the submicrometer range. Actually, this type of membranes has already been used as irradiation masks to produce magnetic nanopatterning on Co/Pt multilayer films [68] and in TiO_2 single crystals [69].

The ion beam nitriding process is carried out using the same conditions as in those employed in the homogeneous approach, but a processing time of 7 minutes is utilized.

The local character of the induced ferromagnetism is also confirmed by magneto-optic Kerr effect measurements together with MFM imaging. Finally, AFM imaging is used to examine the surface topography of the produced patterns.

3.2.B.2.2.2. Magnetic patterning

As a proof of principle, periodic arrays of ferromagnetic structures in the sub-micrometer range have also been directly prepared at the surface of the paramagnetic ASS by nitriding through alumina templates (see Figures 3.37 (a) –AFM– and (b) –MFM in an applied magnetic field of -70 mT–).

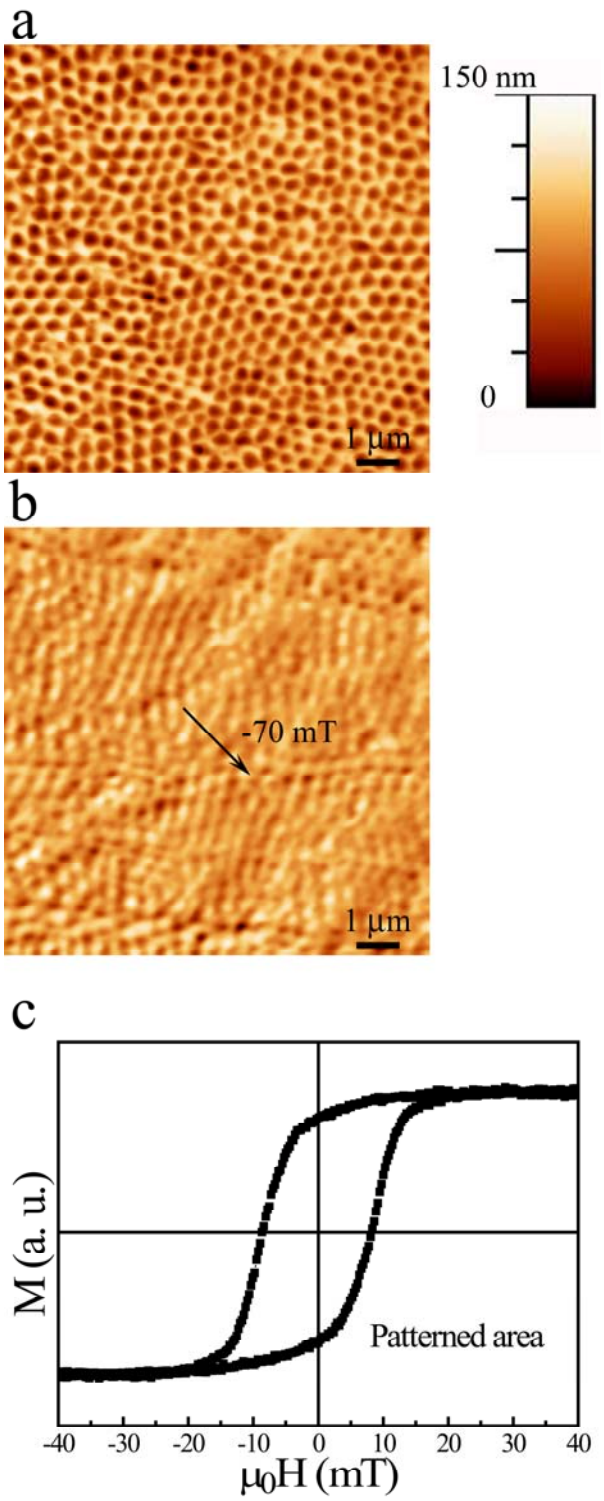

Figure 3.37. *Atomic force microscopy image of a nanopatterned area obtained from nitriding at 400ºC/7min through a pseudo-ordered alumina mask (a) with its corresponding magnetic force microscopy image taken in an applied magnetic field of -70 mT (b). (c) Magneto-optical Kerr effect measurement of a patterned area of the specimen nitrided at 400ºC/7 min –obtained after focusing the laser spot–.*

From the MFM images it can be seen that even though some areas show clear isolated magnetic entities, other areas appear to be magnetically interconnected. This arises from the pseudo-ordered nature of the alumina templates where, in some areas, the separation walls between pores may not be thick enough –see Figure 3.37 (a)– to avoid lateral nitrogen diffusion through these isolation regions. In spite of the existing non-homogeneity in this magnetically patterned sample, coercivities, H_C, around 9 mT are typically obtained –see Figure 3.37 (c)–, whereas $H_C \approx$ 2-4 mT are measured in the microscaled patterned material (see Figure 3.36). Since the laser spot of the MOKE system was focused down to 3 μm diameter (i.e., several structures measured), interconnected structures and isolated ones are susceptible to be measured simultaneously. Note, however, that if the laser spot of the MOKE system is varied between 3-20 μm within one grain, the resulting hysteresis loops are virtually identical. The enhanced H_C may be ascribed to both the physical constraints that the reduced sizes of the nanoscaled structures impose on the propagation of magnetic domains and the existence of single domain entities [27]. Furthermore, as it occurs for the homogeneously irradiated samples, changes in H_C are also observed when varying the in-plane angle of measurement due to the specific crystallographic orientation of the measured grain.

References

[1] T. B. Massalski *Binary Alloy Phase Diagrams*, edited by J. L. Murray, L. H. Bennett and H. Baker (American Society for Metals, Ohio, 1987)

[2] S. Chikazumi *Physics of Magnetism* (John Wiley & Sons Inc., New York, 1964)

[3] B. D. Cullity *Elements of X-Ray Diffraction* (Addison-Wesley Publishing Company, Inc., Boston, 1978)

[4] Y. Yang, I. Baker and P. Martin *Philos. Mag. B* **79** 449 (1999)

[5] X. Amils, J. Nogués, S. Suriñach, M. D. Baró and J. S. Muñoz *IEEE Trans. Magn.* **34** 1129 (1998)

[6] A. Hernando, X. Amils, J. Nogués, S. Suriñach, M. D. Baró and M. R. Ibarra *Phys. Rev. B* **58** R11864 (1998)

[7] E. Apiñaniz, F. Plazaola and J. S. Garitaonandia *J. Magn. Magn. Mater.* **272-276** 794 (2004)

[8] J. Nogués, E. Apiñaniz, J. Sort, M. Amboage, M. d'Astuto, O. Mathon, R. Puzniak, I. Fita, J. S. Garitaonandia, S. Suriñach, J. S. Muñoz, M. D. Baró, F. Plazaola and F. Baudelet *Phys. Rev. B* **74** 024407 (2006)

[9] E. Dieter *Mechanical Metallurgy* (McGraw-Hill, London, 1988)

[10] X. Amils, J. Nogués, S. Suriñach, J. S. Muñoz, L. Lutterotti and M. D. Baró *Nanostruct. Mater.* **8** 801 (1999)

[11] M. A. Meyers, A. Mishra and D. J. Benson *Prog. Mater. Sci.* **51**, 427 (2006)

[12] Y. Yang and I. Baker *Intermetallics* **6** 167 (1998)

[13] X. Amils, J. Nogués, S. Suriñach, M. D. Baró, M. A. Morris-Muñoz and D. G. Morris *Intermetallics* **8** 805 (2000)

[14] D. G. Morris and S. C. Deevi *Mater. Sci. Eng. A* **329-331**, 573 (2002)

[15] S.C. Deevi *Intermetallics* **8** 679 (2000)

[16] X. Amils, J. S. Garitaonandia, J. Nogués, S. Suriñach, F. Plazaola, J. S. Muñoz and M. D. Baró *J. Non-Cryst. Solids* **287** 272 (2001)

[17] X. Amils, J. Nogués, S. Suriñach, J. S. Muñoz, M. D. Baró, A. Hernando and J. P. Morniroli *Phys. Rev. B* **63** 052402 (2001)

[18] S. C. Deevi and R.W. Swindeman *Mater. Sci. Eng. A* **258** 203 (2002)

[19] Y. Yang, I. Baker and P. Martin *Philos. Mag. B* **79** 449 (1999)

[20] D. Wu and I. Baker *Mater. Sci. Eng. A* **329-331** 334 (2002)

[21] X. Amils, J. Nogués, J. S. Muñoz, S. Suriñach and M. D. Baró *Mat. Sci. Forum* **312-314** 531 (1999)

[22] R. Skomski *J. Phys.: Condens. Mater.* **15** R841 (2003)

[23] W. Wernsdorfer, B. Doudin, D. Mailly, K. Hasselbach, A. Benoit, J. Meier, J. -Ph. Ansermet and B. Barbara *Phys. Rev. Lett.* **77** 1873 (1996)

[24] J. Qin, J. Nogués, M. Mikhaylova, A. Roig, J. S. Muñoz and M. Muhammed *Chem. Mater.* **17** 1829 (2005)

[25] A. Concustell, J. Sort, G. Alcalá, S. Mato, A. Gebert, J. Eckert, M. D. Baró *J. Mater. Res.* **20** 2719 (2005)

[26] X. Amils, J. Nogués, S. Suriñach, J. S. Muñoz, L. Lutterotti, S. Gialanella and M. D. Baró *Nanostruct. Mater.* **11** 689 (1999)

[27] J. I. Martín, J. Nogués, K. Liu, J. L. Vicent and I. K. Schuller *J. Magn. Magn. Mater.* **256** 449 (2003)

[28] The calculations have been performed using the TRIM program which is included in the SRIM (*the Stopping Range of Ions in Matter*) package, see http://www.srim.org, J. F. Ziegler, M. D. Ziegler and J. P. Biersack. J. F. Ziegler, J. P. Biersack and U. Littmark *The Stopping and Range of Ions in Solids* (Pergamon, New York, 1985)

[29] This is reflected by the concept of the so-called "cascade efficiency", which varies between ≈ 0.3 and 1 for heavy and light ions, respectively –see R. S. Averback, R. Benedek and K. L. Merkle *J. Nucl. Mat.* **69&70** 786 (1978)–. Although the energies covered in the cited reference are significantly larger, this is expected to be valid as long as the maximum energy transfer in primary collisions is large compared to the damage threshold energy.

[30] M. -J. Caturla, T. Diaz de la Rubia, L. A. Marques and G. H. Gilmer *Phys. Rev. B* **54** 16683 (1996)

[31] J. Nord, K. Nordlund and J. Keinonen *Phys. Rev. B* **65** 165329 (2002)

[32] P. Ziemann, W. Miehle and A. Plewnia *Nucl. Instr. Meth. B* **80&81** 370 (1993)

[33] S. Y. Chou, P. R. Krauss and P. J. Renstrom *Appl. Phys. Lett.* **67** 3114 (1995)

[34] L. J. Heyderman, H. Schift, C. David, J. Gobrecht and T. Schweizer *Microelectron. Eng.* **54** 229 (2000)

[35] L. E. Ocola and A. Stein *J. Vac. Sci. Tech. B* **24** 3061 (2006)

[36] Z. Gu, Ph.D. Thesis, Kungliga Tekniska Höskolan, Stockholm, Sweden (2005)

[37] D. A. Papaconstantopoulos, I. I. Mazin and K. B. Hathaway *J. Appl. Phys.* **89** 6889 (2001)

[38] R. Engel-Herbert and T. Hesjedal *J. Appl. Phys.* **97** 074504 (2005)

[39] C. A. Ross *Annu. Rev. Mater. Res.* **31** 203 (2001)

[40] S. S. Hecker, M. G. Stout, K. P. Staudhammer and J. L. Smith *Metall. Trans. A* **13** 619 (1982)

[41] E. Nagy, V. Mertinger, F. Tranta and J. Sólyom *Mater. Sci. Eng. A* **378** 308 (2004)

[42] H. Ishigaki, Y. Konishi, K. Kondo and K. Koterazawa *J. Magn. Magn. Mater.* **193** 466 (1999)

[43] K. Mumtaz, S. Takahashi, J. Echigoya, Y. Kamada, L.F. Zhang, H. Kikuchi, K. Ara and M. Sato *J. Mater. Sci.* **39** 85 (2004)

[44] W. -S. Lee and C. -F. Lin *Scr. Mater.* **43** 777 (2000)

[45] P. L. Mangonon and G. Thomas *Metall. Trans.* **1** 1577 (1970)

[46] M. W. Bowkett, S. R. Keown and D. R. Harries *Met. Sci.* **16** 499 (1982)

[47] L. E. Murr, K. P. Staudhammer and S. S. Hecker *Metall. Trans. A* **13** 627 (1982)

[48] G. B. Olson and M. Cohen *Metall. Trans. A* **13** 1907 (1982)

[49] J. Talonen, P. Nenonen, G. Pape and H. Hänninen *Metall. Mater. Transac. A* **36** 421 (2005)

[50] R. E. Schramm and R. P. Reed *Metall. Trans. A* **6** 1345 (1975)

[51] P. L. Mangonon and G. Thomas *Metall. Trans.* **1** 1587 (1970)

[52] H. Huang, J. Ding and P. G. McCormick *Mater. Sci. Eng. A* **216** 178 (1996)

[53] P. J. Miller, C. S. Coffey and V. F. Devost *J. Appl. Phys.* **59** 913 (1986)

[54] B. S. Murty and S. Ranganathan *Int. Mater. Rev.* **43** 101 (1998)

[55] J. Sort, S. Suriñach, J. S. Muñoz, M. D. Baró, J. Nogués, G. Chouteau, V. Skumryev and G. C. Hadjipanayis *Phys. Rev. B* **65** 174420 (2002)

[56] W. -S. Lee and C. -F. Lin *Mater. Sci. Eng. A* **308** 124 (2001)

[57] H. N. Han, C. G. Lee, D. -W. Suh and S.-J. Kim *Mater. Sci. Eng. A* **485** 224 (2008)

[58] H. N. Han, C. G. Lee, C. -S. Oh, T. -H Lee and S. -J. Kim *Acta Mater.* **52** 5203 (2004)

[59] A. Rodrigo and H. Ichimura *Surf. Coat. Technol.* **148** 8 (2001)

[60] M. P. Fewell, D. R. G. Mitchell, J. M. Priest, K. T. Short and G. A. Collins *Surf. Coat. Technol.* **131** 300 (2000)

[61] G. Abrasonis, J. P. Riviere, C. Templier, A. Declemy, L. Pranevicius and X. Milhet *J. Appl. Phys.* **97** 083531 (2005)

[62] O. Öztürk and D. L. Williamson *J. Appl. Phys.* **77** 3839 (1995)

[63] M. Zeuner, J. Meichsner, H. Neumann, F. Scholze and F. Bigl *J. Appl. Phys.* **80** 611 (1996)

[64] G. Abrasonis, Doctoral Dissertation, Université de Poitiers, France (2003)

[65] A. Leineweber, H. Jacobs, F. Hüning, H. Lueken, H. Schilder and W. Kockelmann *J. Alloys Compd.* **288** 79 (1999)

[66] A. Leineweber, H. Jacobs, F. Hüning, H. Lueken and W. Kockelmann *J. Alloys Compd.* **316** 21 (2001)

[67] A. P. Li, F. Muller, A. Birner, K. Nielsch and U. Gosele *J. Appl. Phys.* **84** 6023 (1998)

[68] S. W. Shin, S. G. Lee, J. Lee, C. N. Whang, J. H. Lee, I. H. Choi, T. G. Kim and J. H. Song *Nanotechnology* **16** 1392 (2005)

[69] R. Sanz, A. Johansson, M. Skupinski, J. Jensen, G. Possnert, M. Boman, M. Vázquez and K. Hjort *Nano Lett.* **6** 1065 (2006)

4. Conclusions

As a final chapter, the main conclusions of this Thesis are presented. Moreover, some potential applications of the generated patterned magnetic materials will be pointed out.

From a broad point of view, this Thesis shows mainly the viability to produce ordered arrays of ferromagnetic structures, embedded in a paramagnetic matrix, at the surface of either $Fe_{60}Al_{40}$ or austenitic stainless steels by means of diverse routes. These take advantage of the magnetic transitions (from a paramagnetic state to a ferromagnetic one) which occur in the studied materials upon mechanical deformation or ion local irradiation.

Note that below there are more specific conclusions for the main approaches studied in this Thesis.

4.1. $Fe_{60}Al_{40}$ (at. %) alloys

4.1.A. Ferromagnetism induced by mechanical deformation

4.1.A.1. Macroscopic approach: compression tests

The macro-scale deformation-induced ferromagnetism achieved by means of uniaxial compression tests performed at quasi-static conditions has been investigated. The correlation among structural (i.e., lattice cell parameter and atomic intermixing) and magnetic properties indicates that the induced ferromagnetism is mainly controlled by both lattice cell expansion and atomic intermixing at low-stress range processing. Conversely, lattice expansion seems to become the most important cause of the ferromagnetic response at high-stress regime. Moreover, this induced ferromagnetism is virtually independent of the loading rate. Interestingly, the mechanical hardness characterization allows indirect assessment of this phase transition.

4.1.A.2. Micro and nanoscaled approaches: nanoindentation

Here, it is demonstrated that nanoindentation can be used as a serial method to fabricate, in a controlled manner, arrays of micron and submicron magnetic structures at the surface of paramagnetic sheets of $Fe_{60}Al_{40}$. Even though an unavoidable physical patterning is at the same time obtained due to plastic deformation, the locally induced ferromagnetism can be simply removed by heating taking advantage of the annealing-induced atomic reordering processes.

Possibly, applications, such as magnetic separators (i.e., localized zones to trap magnetic particles), could be envisaged for these structures since they have topographic configuration and are embedded in a smooth paramagnetic matrix.

4.1.B. Ferromagnetism induced by ion irradiation

4.1.B.1. Macroscopic approach: broad beam irradiation

The effect of different ion masses on the disordering efficiency of atomically ordered $Fe_{60}Al_{40}$ alloys has been elucidated. For heavy ions, a pure ballistic mixing occurs which is reflected by a universal curve for the damage dependence of the induced magnetism. However, for light ions, a dynamic recovery of the B2-phase, which reduces the disordering efficiency, has to be taken into account. Moreover, the structural effects induced by the irradiation (i.e., atomic intermixing) are also fully reversible. That is, by annealing the disordered-magnetic $Fe_{60}Al_{40}$ alloy (A2-phase) at 900 K for 30 minutes, the non-magnetic ordered B2-phase is completely recovered.

4.1.B.2. Micro and nanoscaled approaches: lithography through shadow masks and focused ion beam

It has been demonstrated that ion irradiation can be used to fabricate, in a controlled manner, arrays of sub-100 nm ferromagnetic structures at the surface of paramagnetic

$Fe_{60}Al_{40}$ sheets, while preserving smooth surfaces. The described methods are based on the selective generation of disorder-induced ferromagnetism via ion irradiation, either by broad beam ion irradiation through shadow masks (TEM grids, patterned polymer resist masks or alumina membranes) or focused ion beam. Remarkably, since irradiation-induced erosion is minimized due to the low fluences used, $Fe_{60}Al_{40}$ sheets can be re-patterned indefinitely, taking advantage of the atomic reordering processes upon annealing, without causing topographic etching. Conversely, methods which bring about a significant physical patterning, such as nanoindentation, can only be processed once.

The utilization of templates which are simply clipped at the surface, such as TEM grids or alumina membranes, allows obtaining large patterned magnetic areas (several square centimeters depending on the size of the template) at once (i.e., parallel process) in a few minutes.

Furthermore, it is worth mentioning that these methods are intrinsically limited by the irradiation process itself. That is, the limit in size of the generated structures is ultimately restricted to the mean free path of the ions through the alloy (i.e., to the lateral distribution of damage).

Interestingly, this arrangement of magnetic structures embedded in a paramagnetic matrix virtually without any physical boundaries could be considered as a potential configuration for magnetic patterned recording media. In particular, the smallest dots produced by FIB, which exhibit much larger coercivities, in excess of $\mu_0 H_C$ = 50 mT and high square-shaped loops. Indeed, even though present-day magnetic recording media have coercivities of around 300 mT, the obtained coercivity may allow recording information in patterned media without requiring exceedingly powerful and bulky writing heads. In addition, the high squareness constitutes a crucial requirement in order to assure the proper storage of information. Hence, this method may lead to a novel type of patterned recording media practically free from tribological (due to the preservation of flat surfaces) and exchange coupling effects (due to the paramagnetic non-irradiated matrix).

4.2. Austenitic stainless steels

4.2.A. Ferromagnetism induced by mechanical deformation

4.2.A.1. Macroscopic approach: ball milling and compression tests

The structural and magnetic properties of either ball-milled AISI 316L powders or uniaxially compressed AISI 316L bulk specimens have been tailored, yielding different responses of the γ (paramagnetic) → α′ (ferromagnetic) strain-induced transformation depending on the loading conditions of the processing technique as the strain rate increases. Namely, whereas larger amounts of the α′ phase are obtained in ball milling procedures as the strain rate increases, compression tests result in opposite trend. These opposite behaviors may stem from both the effects of local temperature rise during deformation and the type (and quantity) of the generated structural defects. Furthermore, it is demonstrated that this solid state transformation can be tailored and correlated in a controlled manner by means of structural, magnetic and mechanical analysis. Hence, this detailed characterization could improve its applications, including developments in non-destructive methods to assess the degradation or enhancements in surface properties (i.e., mechanical hardness and/or wear resistance).

4.2.A.2. Micro and nanoscaled approaches: nanoindentation

By means of nanoindentation experiments, it is possible to fabricate, in a controlled manner, periodic arrays of micrometric and submicrometric magnetic structures at the surface of non-magnetic stainless steel. This method is based on the mechanically-induced martensitic phase transformation that occurs in austenitic steel. The induced ferromagnetism can be removed by subsequently subjecting the locally deformed sheets to annealing processes at temperatures high enough to transform the martensite back to austenite.

As a potential application, this type of material could be also useful for magnetic separation.

4.2.B. Ferromagnetism induced by ion irradiation

4.2.B.1. Macroscopic approach: broad beam ion beam nitriding

Nitriding of austenitic stainless steels at moderate temperatures (around 400 ºC) leads to the formation of the supersaturated nitrogen solid solution "expanded austenite" or γ_N phase. Since this phase shows ferromagnetic behavior, this method paves a new approach of producing ferromagnetic structures using the existing routes.

4.2.B.2. Micro and nanoscaled approaches: lithography through shadow masks

In this approach, it has been demonstrated that it is possible to fabricate, in a controlled manner and in parallel processes, periodic arrays of micron and sub-micron magnetic structures at the surface of non-magnetic austenitic stainless steels by means of ion beam nitriding through shadow masks. This method is based on the expansion of the austenite lattice due to the incorporation of nitrogen atoms that occurs during irradiation of austenitic stainless steel. In principle, this process of selectively and locally inducing ferromagnetism could be also performed by means of other nitriding processes such as gas or plasma nitriding. Once again, the obtained topography opens a potential application of these materials as magnetic separators.

Appendix

Austenitic stainless steels (ASSs) are ferrous alloys, which consist in a FCC crystal lattice, that create a passive state on their surface to keep hard to be stained. ASSs must contain chromium as an alloy component in order to create the protective film (i.e. passivation film) on the surface that causes corrosion resistance.

Elements of the base of ASSs are:

- Chromium, whose quantity has to be higher than 16 mass % in order to assure the stainless character.

- Nickel, whose quantity has to be higher than 8 mass % in order to obtain the austenitic structure at all temperatures.

Besides that, steels contain:

- Carbon, whose quantity can be graded into three categories: $C \leq 0.03$ mass %: low carbon ASSs (type L); $0.03 < C \leq 0.08$ mass %: average carbon ASSs; $C > 0.08$ mass %: elevated carbon steels

- Manganese, whose quantity does not exceed 2 mass % except particular cases.

- Silicon, whose quantity does not exceed 1 mass % except particular cases.

- Sulfur and phosphor as contamination, whose quantity does not exceed 0.04 mass % except particular cases.

The carbon content has to be low in order to hinder the formation of Cr carbides in the grain boundaries. If it exceeds 0.03 mass %, additional elements such as Ti or Nb and Ta have to be added in order to trap carbon atoms in form of carbides and to avoid the formation of Cr carbides, which causes a decrease in intergranular corrosion resistance.

Certain elements, such as Mo or Cu, are added to improve the corrosion resistance in the presence of certain fluids [1].

The compositional ranges (in mass %) of the utilized ASSs are:

	C max	Mn max	Si max	P max	S max	Ni	Cr	Mo
AISI 304L	0.03	2	1	0.045	0.03	8.0 -10.5	18-20	-
AISI 316	0.08	2	1	0.045	0.03	10-14	16-18	2-3
AISI 316L	0.03	2	1	0.045	0.03	10-14	16-18	2-3

Reference

[1] S. L. Chawla and R. K. Gupta *Materials Selection for Corrosion Control* (ASM International, Materials Park, Ohio, 1997)